Department of Physics

Physics PhD program   Cycle XXXIII

Studies on a PET module prototype for the recovery of Compton events

Surname   Polesel

Name   Andrea

Registration number   762543

Tutor: Prof. Marco Paganoni

Supervisor: Dr. Etiennette Auffray

Coordinator: Prof. Marta Calvi

ACADEMIC YEAR 2019/2020

Abstract

Andrea POLESEL

Studies on a PET module prototype for the recovery of
Compton events

In this thesis we will present different studies carried out on a prototype of PET module detector with pixelated crystals, light sharing and single side readout.

A dedicated experimental setup was initially developed and characterised, in order to satisfy all the requirements in terms of spatial, energy and time resolution. This setup allows multiple channels readout with parallel chains for energy and time measurement and various possibilities for automation given by several possible mechanics arrangement. The flexibility of this setup allowed to perform all the successive studies using the same Data Acquisition electronics and software. Moreover, it opens up the possibilities for further tests on multi-channels detectors and on image reconstruction.

The first application of this setup was the improvement of the Coincidence Time Resolution of the PET module exploiting Depth Of Interaction information. The contribution to the time resolution due to different speed of gamma and optical photons inside the detector was mitigated with an algorithm that only requires a calibration measurement compared to the DOI capable prototype used. To achieve the best possible time resolution in this configuration, multiple time stamps were combined to obtain a better time of interaction estimator. This work is particularly interesting for possible application in high resolution PET scanners, because it relies on single side readout and requires production costs only slightly higher compared to a similar existing module without DOI capability.

Moreover, an algorithm was developed to correctly identify the crystal of first interaction in case of Inter-Crystal Scatter events. These are events in

which the primary gamma photon interacts with multiple channels of the PET detector. Different approaches to the subject are found in literature; one of these is to use an algorithm to sort the energy depositions. This is the approach used in this study: a new algorithm was developed, preliminary tested by means of Geant4 simulations and later applied on the PET module previously developed using the experimental setup originally described. The possibility to include ICS event with good accuracy would allow to increase sensitivity or image quality depending on the method to whom this approach is compared to. The long term possibilities of this algorithm will be discussed further at the end of this thesis.

Acknowledgements

First of all, I would like to thank my Cern supervisor, Dr. Etiennette Auffray, my University supervisor, Professor Marco Paganoni, and Dr. Marco Pizzichemi for the their support and availability from the first day to the (very) last hour of this PhD project. Their knowledge, advise and feedback were fundamental in these three years and in particular in the last one, twice as challenging.

My gratitude goes also to my friends and colleagues of Cern and Milano for the work conversations, for the fun conversations and for the funny work conversations.

My friends and family in Italy were always present as well. I've never felt alone during the isolation of 2020 and to all of them goes my sincere gratitude too (Matteo is included here but he's too important not to be explicitly mentioned).

And *finally*, to Joelle.

Contents

viii

List of Figures

List of Tables

List of Abbreviations

ADC	Analog to Digital Converter
APD	Avalanche Photon Diode
CFD	Constant Fraction Discriminator
CT	Computed Tomography
CTR	Coincidence Time Resolution
DOI	Depth Of Interaction
DAQ	Data AcQuisition
ESR	Enhanced Specular Reflector
ICS	Inter Crystal Scatter
FBP	Filtered Back Projection
FDG	FluDeoxyGlucose
FEB	Front End Board
FOV	Field Of View
FWHM	Full Width at Half Maximum
G-APD	Geiger-mode Avalanche Photon Diode
LO	Light Output
LOF	Line Of Flight
LOR	Line Of Response

LSO	Lutetium OrtoSilicate
LTE	Light Transfer Efficiency
LY	Light Yield
LYSO	Lutetium Yttrium OrtoSilicate
MLEM	Maximum Likelihood Expectation Maximization
MRI	Magnetic Resonance Imaging
NEC	Noise Equivalent Counts
MPPC	Multi Pixels Photon Counter
PCB	Printed Circuit Board
PDE	Photon Detection Efficiency
PDF	Probability Densiry Function
PEM	Positron Emission Mammography
PET	Positron Emission Tomography
PMT	Photon Multiplier Tube
PSD	Pulse Shape Discrimination
PSF	Point Spread Function
PTS	Photon Time Spread
PVT	PolyVinylToluene
QE	Quantum Efficiency
ROI	Region Of Interest
SPAD	Single Photon Avalanche Photodiode
SiPM	Silicon Photon Multiplier

SNR   **S**ignale to **N**oise **R**atio

SPTR   **S**ingle **P**hoton **T**ime **R**esolution

TDC   **T**ime to **D**igital **C**onverter

TOF   **T**ime **O**f **F**light

TOT   **T**ime **O**ver **T**hreshold

VOR   **V**olume **O**f **R**esponse

WLS   **W**ave**L**enght-**S**hifter

Anche questa volta,
per le mie nonne

Chapter 1

Introduction to Positron Emission Tomography

PET (*Positron Emission Tomography*) is a clinical imaging technique able to provide metabolic images of the patient. Among its field of application we find oncology, cardiology, neurology, psychiatry and *in-vivo* studies of small animals. Thanks to the ability to detect concentrations down to the pico-molar level, it is the most sensitive molecular imaging technique.

In this chapter the principle of PET is going to be presented, as well as the key components of a PET scanner and its physical parameters.

1.1   How PET works

PET is based on the use of a radiotracer, a radioactive isotope embedded in a drug, which is chosen depending on the specific application and target. Through a β^+ decay, it emits a positron which annihilates with an electron of the body: the idea of a PET scanner is to detect the two γ photons generated following this annihilation. The knowledge of the positions of interaction of these two γ with the detector allows to define a *Line Of Response* (LOR), the line connecting the two positions. Considering the kinematics of the phenomenon, we know that the position of annihilation lays on this line. By tracing multiple LORs, it is possible to reconstruct the area where the radio-tracer was accumulated.

A scheme for the general principle of work of a PET scanner can be seen in figure 1.1.
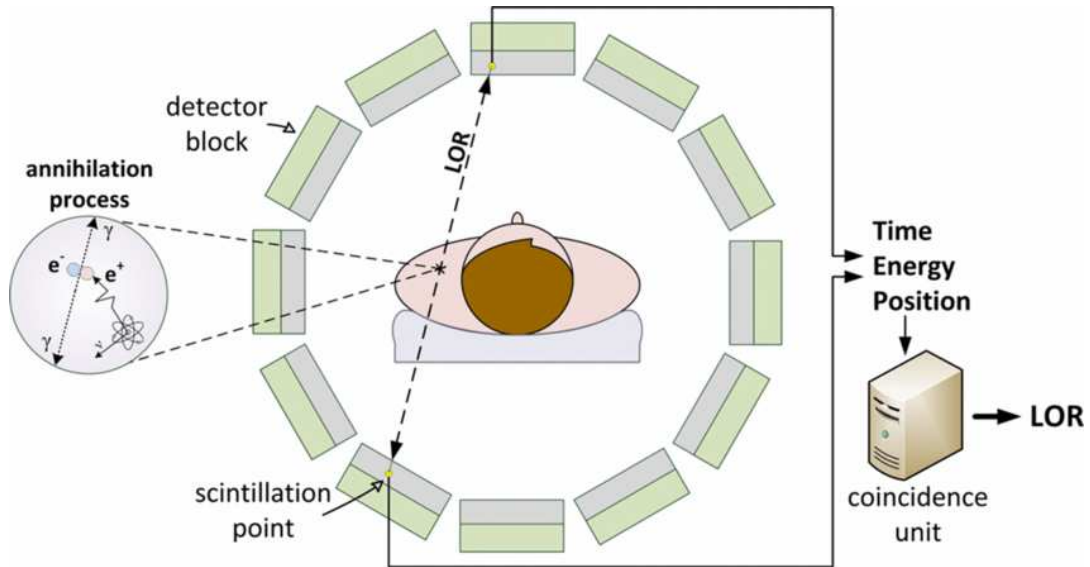
FIGURE 1.1: General scheme of a PET scanner

1.2   Physics

1.2.1   The radioactive tracer

The possibility to use radioactive tracers in PET and other fields of nuclear medicine is based on the Tracer Principle, discovered by George de Hevesy in 1923, which states that the biological behaviour of molecules is not affected by the presence of radioactive isotopes of the elements of such molecule.

Fluorodeoxyglucose (FDG) is the most common tracer in Positron Emission Tomography for oncology applications. It is a glucose molecule in which fluorine, which replaces an OH group, is present in its unstable isotope, fluorine-18 (^{18}F) (see figure 1.2). Given the high metabolism of cancer cells, glucose will accumulate in those regions of the body and the presence of fluorine-18 will allow to draw a map of the radioactive density of the body of the patient.
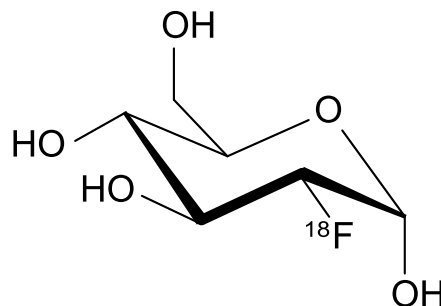
FIGURE 1.2: Stereo skeletal formula of fluorodeoxyglucose (By Anypodetos - Own work, Public Domain, wikimedia)

Isotope	Half-Life (min)	Average kinetic energy (MeV)	Kinetic energy endpoint (MeV)	Average range (water) (mm)	Maximum range (tissue) (mm)
^{11}C	20.4	0.385	0.960	1.2	4.2
^{13}N	10.0	0.491	1.198	1.6	5.4
^{15}O	2.0	0.735	1.732	2.8	8.4
^{18}F	109.8	0.242	0.633	0.6	2.6

TABLE 1.1: Physical properties of physiological radioisotopes
(Del Guerra, Belcari, and Bisogni, 2016)

Thanks to the Tracer Principle, any other pharmaceutical can be labeled with a β^+ radioactive isotope (Schmitz et al., 2005). The most common are carbon-11 (^{11}C), nitrogen-13 (^{13}N), oxygen-15 (^{15}O), fluorine-18 (^{18}F), gallium-68(^{68}Ga) and rubidium-82 (^{82}Rb). Their applications are not limited to oncology, but are also used in Cardiology, Neurology and other fields of medicine. Their physical properties are shown in table 1.1.

The half-life is the parameter that poses the strictest constraints in the logistic of the usage of each isotope in hospitals: when it is too short for convenient storage, it must be produced *in loco* or very close by and rapidly delivered. This is one of the reasons why Nuclear Medicine hospitals are often equipped with facilities such as cyclotrons. Fluorine-18 for example is obtained with these machines: the stable mother target (^{18}O) is bombarded with protons to obtain (^{18}F) ($^{18}O + p \rightarrow ^{18}F + n$).

1.2.2 Positron annihilation

The fundamental physical phenomenon on which PET is based is the annihilation of a positron with an electron (Bailey, Karp, and Surti, 2005). This happens after the emission of a positron from a radioactive nucleus, which decays β^+:

$$p \rightarrow n\, e^+\, \nu \tag{1.1}$$

The positron subsequently loses its energy in a similar way to an electron in matter, through radiative loss or ionization. When it encounters an electron,

it forms a bonded state (*positronium*), which in the end results in the annihilation of the two particles. The cross-section of this process (electron-positron annihilation) is highest for systems with low velocity of the center of mass. For this reason the annihilation is most likely to happen when the positron is thermalized with the environment.

The fact that the annihilation of the positron happens at a different position from the decay of the nucleus, sets a lower limit to the possible spatial resolution of PET. The range of the positron is a function of its energy, and therefore is different for each isotope (see table 1.1).

A second effect that deteriorates spatial resolution is the non collinearity of the two γ photons emitted: if the annihilation of electron and positron happens before they completely lose their kinetic energy, the residual momentum is transferred to the gamma photons, which receive a boost along a specific direction.

1.2.3   Photon interaction with matter

Among the various way in which a γ photon can interact with matter, two of them are relevant in Positron Emission Tomography: photoelectric absorption and Compton scattering. Pair production, the other way for a γ photon to interact with matter, is a process with an energy threshold, 1022 KeV; for this reason it does not play a role in PET. All these phenomena result in a partial or complete energy transfer from photon to an electron. Differently from what happens for the energy loss of a charged particle, which is a gradual process, photons lose their energy in one or a few scatters, which profoundly vary their trajectory and energy.

Photoelectric absorption

In a photoelectric absorption, a photons interacts with an atom, and an electron is emitted as a consequence; in the case of gamma rays with sufficient energy, the most probable shell of emission is the K one. The energy of the resulting photoelectron is

$$E_{e^-} = h\nu - E_b \tag{1.2}$$

where E_b is the bonding energy of the electron on his original shell. This E_b effectively acts as a threshold level for low energy photon, causing the characteristic bumps in the cross-section for this process seen in figure 1.4. For γ
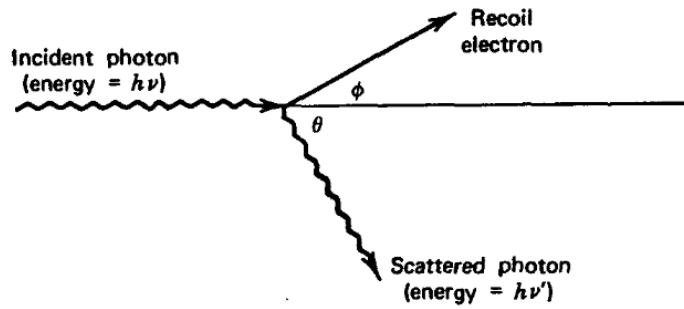
FIGURE 1.3: Compton scattering (from Knoll, 2010)

rays of a few hundred keV of energy or more, the electron carries away almost all of the photon energy. Photoelectric effect is the dominant process for photons of a few hundred keV or less. This process is enhanced in absorbing materials with high Z. Even though a general expression for a given γ energy and Z for photoelectric absorption does not exist, a good approximation is

$$\tau \propto Z^n E_\gamma^{3.5} \tag{1.3}$$

where the exponent n varies from 4 to 5 as a function of E_γ.

Compton scattering

Compton Scattering is a process that happens between a γ photon and an electron of the absorbing material. The photon is scattered with an angle θ from its original direction and part of its energy is transferred to the electron. This energy can vary from 0 up to a large fraction of the original E_γ. The expression that correlates the energy transferred and the scattering angle can be obtained by simultaneously imposing the conservation of energy and momentum. Using the same symbols as in figure 1.3, we obtain:

$$h\nu' = \frac{h\nu}{1 + \frac{h\nu}{m_0 c^2}(1 - \cos(\theta))} \tag{1.4}$$

where $m_0 c^2$ is the rest energy of the electron. The greatest energy transfer happens for $\theta = \pi$. The Compton scatter probability for every absorbing atom depends on the number of electrons on which the scatter can happens; consequently, it scales linearly with Z. The angular distribution of the scattered γ photon is given by the Klein-Nishina formula (Klein and Nishina, 1929) for the differential cross-section $\frac{d\sigma}{d\Omega}$.
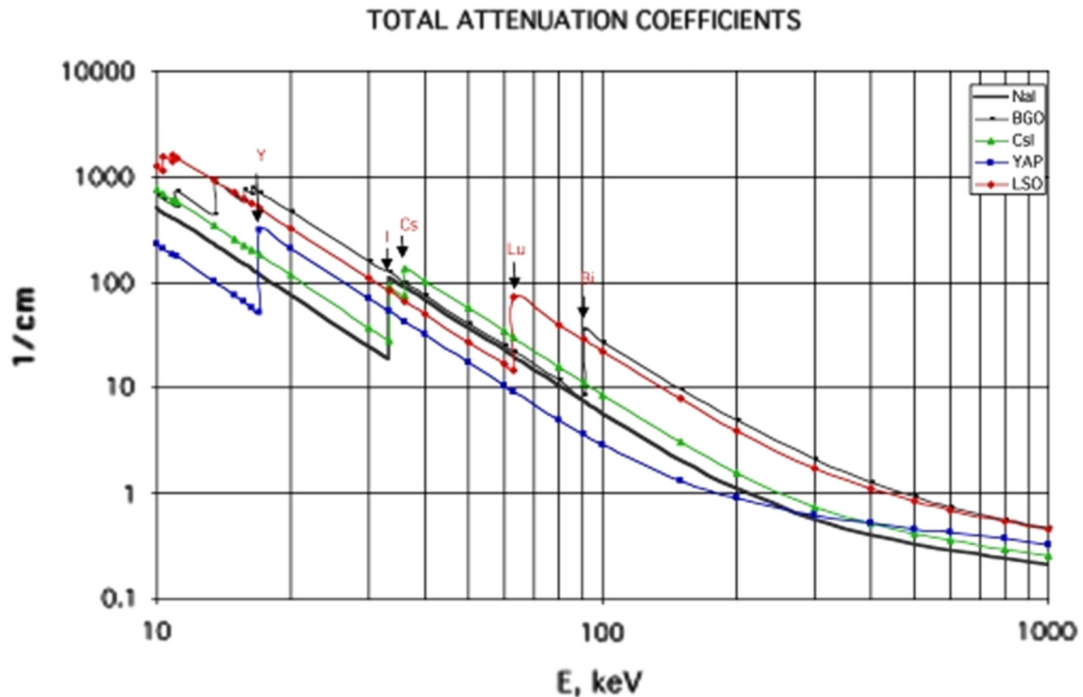
FIGURE 1.4: Total Attenuation Coefficients for various crystal
for PET application (from Lecoq, 2016)

1.2.4 Scintillating crystals

A scintillating crystal is a material that emits, upon the passage of charged
particles inside it, scintillating light. It is typically made of a material where
the energy gap between valence and conduction band is of few eV. The pas-
sage of a charged particle through the crystal excites electrons up to the con-
duction band, and the number of these electrons is proportional to the energy
lost by the incoming particle. The radiative de-excitation at a wavelength at
which the crystal is transparent is encouraged by doping the material with
elements that modify the band structure of the lattice (see figure 2.3). By so
doing, in the proximity of these centers, the energy gap between ground and
excited states is lower, and therefore also the energy of the photon emitted
is smaller. These optical photons are collected by a photodetector, and their
number is proportional to the energy lost by the charged particle inside the
bulk of the crystal.

The intrinsic characteristics of a crystal are fundamental for its energy and
time performances and therefore also for the PET detector. The parame-
ters usually quoted are Light Yield, defined as the number of optical pho-
tons emitted per MeV of incident γ photon, Decay Time, defined as the time
constant of the emitted light profile, and the attenuation coefficient μ for a
gamma photon of 511 keV, which is the inverse of the attenuation length (the
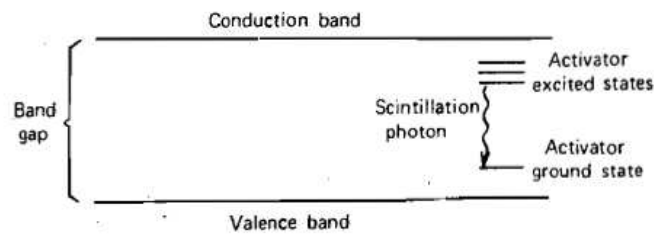
FIGURE 1.5: Diagram of scintillation mechanism in a crystal
(from Knoll, 2010)

thickness of a material at which the probability that a photon has not been absorbed has dropped to $\frac{1}{e}$).

The properties and characteristics of scintillating crystals are going to be discussed in further lengths in the next chapter.

1.2.5 Scintillators suitable for PET

In order for a scintillator to be used in PET application, it must have low attenuation length, high light yield and short decay time. The motivations for these requirements will be more clear is section 1.5. In table 1.2 the properties of various crystals are summarised. I_0, in particular, is worth of discussion: defined as the ratio between the relative light output and the scintillation decay time normalized to LSO, it combines two of the three parameters mentioned before. As seen from the table, $LaBr_3$ is the only candidate with a better score than LSO (Schaart et al., 2010). However, this crystal, on top of being hygroscopic, is characterized by a higher attenuation length, that would require longer crystals which in turn would cause higher parallax error and lower time resolution. LuAP instead is affected by an emission wavelength that does not match the range of higher detection efficiency of the most commonly available photodetectors. For these reasons, LSO (and its variation LYSO) are still the most common crystals for PET applications.

1.3 Description of a total body PET scanner

A whole-body PET machine consists of a cylindrical detector within which a table is placed to support the patient. The internal diameter is around 65-85 cm wide. The detector itself is made up of various modules, and each one of them contains a number of scintillating crystals (typically L(Y)SO) coupled to photodetectors; the single pixel size is usually in the 3 to 5 mm in section

Name	BGO	NaI	LSO	LaBr$_3$	LuAP
Composition	Bi$_4$$Ge_3O_{12}$	NaI	Lu$_2$$SiO_5$	LaBr3	LuAlO$_3$
Dopant		Tl	Ce	Ce	Ce
Density (g/cm^3)	7.1	3.67	7.4	5.3	8.34
Z_{eff}	75	51	66	46	65
Refractive Index	2.15	1.85	1.82	1.9	1.94
Attenuation Length (mm)	10.4	29.1	11.4	22.3	11
Prob. of PE effect (%)	40	17	32	14	32
LO (relative to LSO) (%)	30	137	100	200	40
I_0 (relative to LSO) (%/ns)	4	24	100	500	90
Decay time (ns)	300	230	40	16	18
Scint. emission wavelength (nm)	480	510	420	360	365
Hygroscopic	no	yes	no	yes	no

TABLE 1.2: Properties of various scintillating crystal for PET application (adapted from Eijk, 2002), Lecoq, 2016 and Lecomte, 2009

and 15 to 25 mm long. The modules are arranged in each ring in a radial geometry, usually 15 to 25 cm long, in order to reach the highest possible sensitivity (Vandenberghe, Moskal, and Karp, 2020).

The electronics present inside the scanner allows to acquire data: whenever a pulse from a crystal has an amplitude compatible with a signal from a 511 keV γ photon, the coincidence chain waits for a second signal of equal amplitude for a certain time; if such an event occurs, the signal coming from the two modules are acquired, otherwise the event is discarded.

The detector, which contains a certain number of rings of modules, is able to translate along the axis of the cylinder so as to perform a complete uniform scan of the body of the patient. A complete scan, head to thigh, requires usually 5 bed positions. Thanks to the improvement of the performances of the detectors and the computational capabilities of modern computers, the acquisition nowadays is no longer limited to 2D, but each ring of detectors is instead in coincidence with all the other rings, allowing to obtain 3D images.

In modern PET machine, alongside this cylinder, a CT machine is present (Beyer et al., 2000) in order to provide a high-resolution image of the structure of the body of the patient, complementary to the one obtained through a PET scan (Alessio et al., 2004); in figure 1.6 are shown pictures taken from a PET and a CT scan, and the combination of the two.

For a total body scan, around 1 minute is dedicated to the CT and 10-20 minutes for the PET scan itself.

Other types of PET scanner exists, such as those dedicated to specific organs (Surti and Karp, 2008) or parts of the body (Vilardi et al., 2006), which have lower dimensions and therefore higher performances (see table 2.1 in section 1.8)

1.4 Reconstruction

As explained in the section 1.1, from the intersection of multiple LOR lines it is possible to obtain the distribution of the radiotracer inside the body. An algorithm is necessary in order to compute the spatial distribution $\rho(x, y, z)$ of the activity from a set of LOR. The principle on which reconstruction is based is that the number of LOR between a set of two points is proportional to the line integral of the ρ distribution along the LOR:
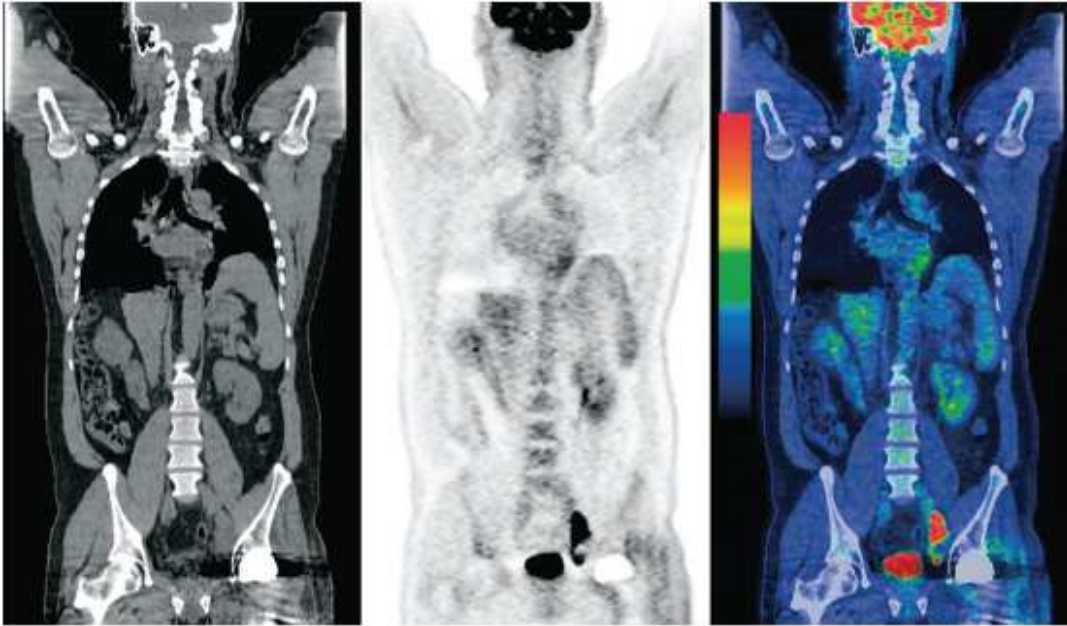
FIGURE 1.6: Left: CT image; middle: PET image; right: super-
position of the two (from Gong et al., 2014).

$$N_{i,j} = k \int_{LOR_{i,j}} \rho(x,y,z) dl \qquad (1.5)$$

Given the finite size of the detector crystals, this formula can be generalized
for any given couple of crystals *i* and *j* defining a Volume Of Response (VOR):

$$N_{i,j} = k' \int_{VOR_{i,j}} \rho(x,y,z) dv \qquad (1.6)$$

which is the fraction of Field Of View (FOV) seen by the two crystals.

The purpose of reconstruction is to obtain the activity distribution function
ρ from a set of LOR_{ij}. The Field of View is usually discretized in a number
of small volumes called voxels, and each of these voxels is characterized by
a certain value of activity.

1.4.1   The different approaches to reconstruction

There are two different types of algorithms available to reconstruct a PET
image: analytic algorithm and iterative ones.
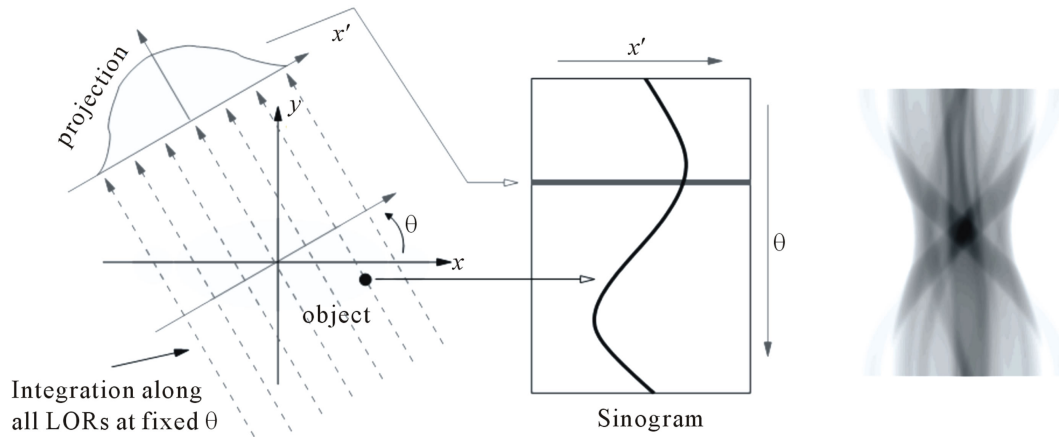
FIGURE 1.7: How to obtain a sinogram (from Asl and Sadremomtaz, 2013)

Analytic algorithm

Analytic algorithms take as input the data organized in sinograms: these are plots of the projection on an axis x' of all the line of response at fixed angle θ. This projection is done for all angles around the center of the Field Of View (see figure 1.7).

This mathematical process is called Radon Transform (see Radon, 1986).

The function ρ is then obtained through a *Filtered Back Projection* (FBP): the value of the projections explained above is added to all voxels crossed by the LORs defined by (x', θ), with a weighting factor to account for the path length of the line through the voxel.

Iterative algorithm

An iterative algorithm uses instead statistical considerations in order to improve the image quality. One of the most used algorithms of this kind is the *Maximum Likelihood Expectation Maximization* (ML-EM), which aims to find the activity values λ_j, defined by:

$$\lambda_j = \int_{voxel_j} \rho(x, y, z,) d\tau \tag{1.7}$$

that maximize the number of counts in each LOR, now indicated by n_i; this method works with data directly stored in LORs, without the need to use

sinograms. These methods are characterized by a lower noise and have therefore replaced analytic ones, once the computation power of computers has been sufficiently high.

1.5 Parameters

In order to evaluate and compare the performances of a PET scanner, some fundamental parameters are usually reported: spatial, energy and time resolution and sensitivity.

1.5.1 Spatial resolution

The spatial resolution of a PET scanner is given by the width of the Point Spread Function (PSF) measured using a point source; it can be written as (Moses, 2011):

$$FWHM = 1.25\sqrt{(d/2)^2 + b^2 + (0.0022D)^2 + r^2 + p^2} \qquad (1.8)$$

where:

- d is the detector size;

- b is the coding error (usually more than one crystals are associated to a single photodetector; the position of interaction is obtained using an Anger logic scheme). This term also include the possibility of inter-crystal scatters);

- D is the scanner diameter;

- r is the positron range;

- p is the parallax effect;

This width is measured both in the axial and transaxial direction, because the geometry of the system causes different performances in different directions. Typical values of spatial resolution for commercial whole-body PET scanners are of the order of 4 to 6 mm; small animal PET scanners and pre-clinical prototypes can achieve better values, but the range of the positron put a lower bound to the best possible spatial resolution.

1.5.2 Time resolution

The ability of a pair of detectors to determine the difference in the time of arrival of γ photons is called Coincidence Time Resolution (CTR); this parameter depends on the scintillator light yield and decay time ($\tau_d = 1/\lambda$), as well as on the coincidence chain. The dependence on the crystal parameters can be written as:

$$CTR \propto \sqrt{\frac{\tau_r \cdot \tau_r}{N_{ph}}} \tag{1.9}$$

where τ_r is the rise time of the pulse. From this relation it is clear that in order to obtain a good timing resolution, it is necessary to have a fast scintillator with a high light yield; crystals of choices of commercial scanners are BGO and L(Y)SO, with a tendency towards L(Y)SO in the recent years.

Commercial whole-body PET scanners with PMTs have a time resolution of the order of ~ 500 ps, but the most performing models, based on SiPMs, reach up to ~ 215 ps (Siemens Biograph Vision PET/CT (see Reddin et al., 2018)).

Improving time resolution is a key factor in achieving a better Signal to Noise Ratio (Lecoq et al., 2010). Similarly to spatial resolution, also in the case of CTR the lower bound is set by the positron free range, which translates to around 10ps of minimum achievable time resolution. In this case, however, the margin of improvement is much greater and bigger than an order of magnitude (Lecoq et al., 2020).

1.5.3 Energy resolution

The ability of a detector to discriminate particles of similar energies is called energy resolution. It is usually quoted as the ratio between the FWHM and the peak position of the distribution of signals produced by a monoenergetic source (usually the 511 keV peak of ^{22}Na or 622 keV of ^{60}Co). It is a fundamental property of the crystal used, and is proportional to the square root of the intrinsic Light Yield: the higher the light yield, the higher the resolution.

In case of a PET scanner, this parameter is fundamental in order to be able to discriminate from a 511 keV event and scatter and background ones (see section 1.6).

1.5.4 Sensitivity

The sensitivity of a PET scanner is the ratio between the rate of coincidences detected by the device and the unit of activity of the radiotracer. It is a function of geometric efficiency, detection efficiency, the width of the energy window and dead time of the scanner; the sensitivity of a single ring can be written as:

$$S = A \cdot \epsilon^2 \cdot \exp^{-\mu t} \cdot 3.7 \cdot 10^4 4\pi r^2 (cps/\mu Ci) \qquad (1.10)$$

where A is the detector area seen by a point source, ϵ is the detector efficiency, μ is the linear attenuation coefficient, t is the thickness of the detector and r is the radius of the ring. The unit of measure is counts per second per micro Curie.

The optimization of this parameter is fundamental in order to reduce the dose injected inside the patient and to shorten the time length of an exam: the higher the coincidences are detected in a fixed time, the lower can be the intensity of the source or the duration of the scan.

As will be explained in Chapter 5, one possible strategy to improve sensitivity in pixelated PET scanners is to include a portion of Inter-crystal Compton Scatter events: for the same amount of activity, the number of events used for reconstruction would increase with this technique.

1.6 Random Coincidences and Scatter Events

Of all the coincidences measured by a PET scanner, real coincidences corresponding to a couple of γ photons produced by an annihilation event are only a fraction (Bailey, 2005). Their rate can be expressed as:

$$R_{true} = R_0 \cdot \eta_{detector}^2 \cdot \eta_\Omega^2 \cdot \exp -\frac{D}{\lambda_{tissue}} \qquad (1.11)$$

where R_0 is the tracer activity in Bq, $\eta_{detector}$ is the gamma detector efficiency, η_Ω is the solid angle coverage of the detector, D is the thickness of the patient and λ_{tissue} the attenuation length in the tissue.

However, of all the events detected, a certain number of them is given by the so-called random coincidences: two gamma photons from different β^+decay arrive at the detector within the set time window, and are therefore regarded

as real. This can happen when only one gamma photon from each pair is detected. The random coincidence rate is given by the formula

$$R_{random} \propto \Delta t \cdot S^2 \tag{1.12}$$

where Δt is the coincidence time window and S is the single count rate. These events can be reduced by improving time resolution and therefore reducing the time window: the chance to use a shorter coincidence time window allow to deal with a proportionally shorter random coincidence rate.

Even among real coincidences, it may happen that one or both photons are scattered inside the body of the patient (where the attenuation length in tissues is about 10cm), the scanner frame or the detector itself (Inter-Crystal Scatter events); these events can be discarded within the limits of energy resolution. However, it is not possible to discriminate scatter events inside a single crystal; this causes an intrinsic degradation in spatial resolution.

All these possible cases are graphically shown in figure 1.8.

In conclusion, only true coincidence events correspond to LOR that truthfully represent the physics of the positron annihilation. Random and scattered coincidence events contribute instead to the degradation of the Signal to Noise Ratio (SNR), one of the parameters used to estimate the purity of the signal:

$$SNR \propto \sqrt{\frac{R_{true}^2}{R_{true} + R_{random} + R_{scattered}}} \tag{1.13}$$

1.7 Parallax Error

When a decay event takes place at the center of the Field Of View (FOV), the Volume of Response (VOR) size is solely determined by the cross-section of the crystals and the scanner diameter. On the other end, when two gamma photons are emitted from the peripheral regions of the FOV, the size of the VOR is influenced by the crystal length as well. For this reason longer crystals, despite being useful to increase sensitivity, cause an increase in parallax error as well.

A possible solution to overcome this difficulty is to include Depth Of Interaction (DOI) information in the calculation of the VOR. DOI, defined as the position of the interaction of the gamma photon in the crystal along its main
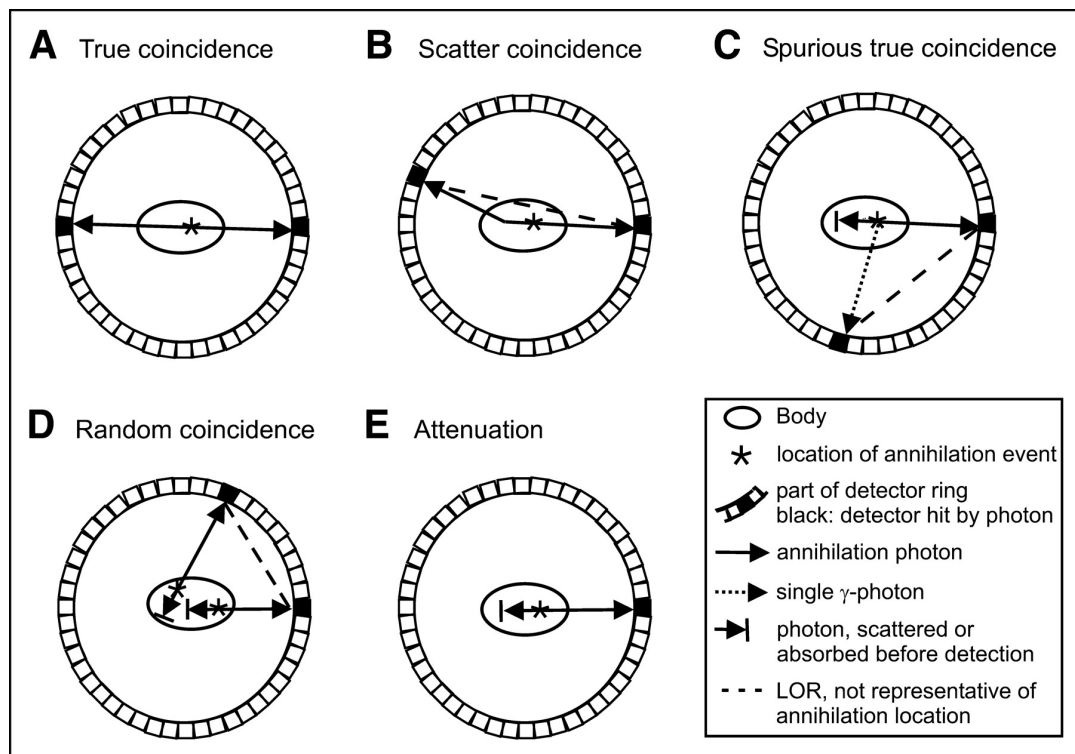
FIGURE 1.8: Various kinds of events that can happen in a PET scanner (from Verel, Visser, and Dongen, 2005)

axis, helps to reduce the parallax error as it narrows the dimension of the projection of the crystal.

There are many methods that have been developed to obtain DOI information; they will be further discussed in Chapter 5 and 6.

A b

1.8   Brief history of PET

The first preliminary idea of PET was presented in 1951 by W. Sweet (Sweet, 1951); the following year W. Sweet and G. Brownell build the first prototype of a brain PET scanner using two NaI(Tl) crystals, each of them coupled to a PMT (Brownell and Sweet, 1953). In 1974 the Lawrence Berkeley Laboratory group proposed for the first time the use of BGO as scintillating crystal; the Bismuth Germanate was used as crystal of election for the following 20 years (Cho and Farukhi, 1977). The 1:1 coupling between crystal and photodetector was soon replaced by a *block detector* design suggested by M.Casey and R.Nutt in 1986 (Casey and Nutt, 1986), and was used up until a few years ago. Finally, the last breakthrough was the switch from BGO to LSO(Ce) and
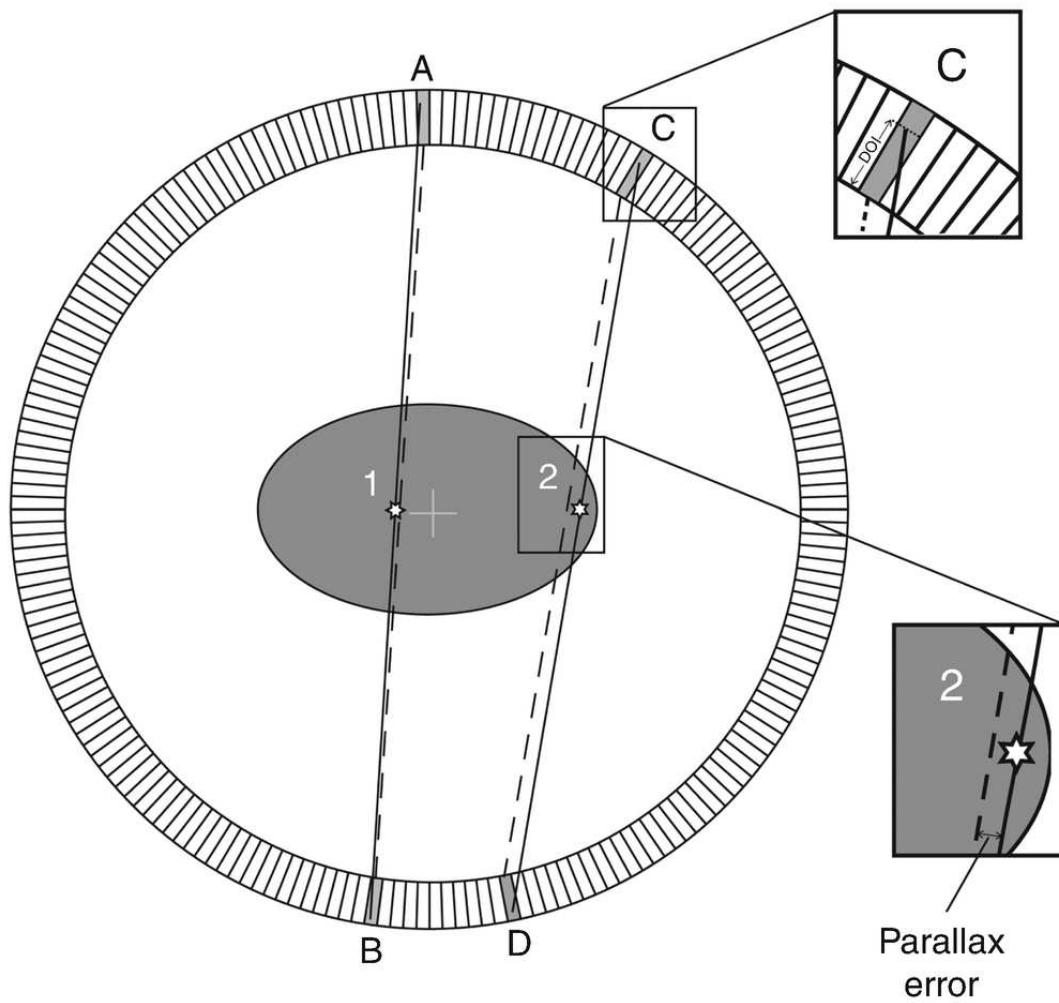
FIGURE 1.9: Effect of DOI in reducing parallax error (from
Verel, Visser, and Dongen, 2005)

LYSO(Ce), chosen for their excellent properties of high light yield and fast decay time; the performance improvement allowed the passage from a 2D to a 3D reconstruction.

1.9   State of the art and future developments

Research is ongoing in order to optimize all aspects described in section 1.5 (see Pizzichemi, 2016). First of all there is a need for a scintillator with high light yield, high stopping power and fast scintillation; however, it is demonstrated that the scintillation mechanism causes an intrinsic limitation, of $\sim$ 100 ps, to the CTR that can be achieved. For sub-100 ps timing resolution, other phenomena that produce prompt photons need to be considered, such as Cerenkov photons (Gundacker et al., 2020), hot intraband luminescence ((Lecoq, 2016) and heterostructures of scintillators and nanocrystals (Turtos et al., 2019).

Another aspect of the chain that has the chance to improve the overall performance of a PET scanner is the photodetector. As already mentioned, the current trend in commercial scanners is to move from PMTs to solid-state detectors. In this sense, research is now focused on digital SiPMs instead of standard analog ones, and on new SiPMs that allow separating the sensitive area of the detectors from the electronics, increasing the fill factor and therefore the efficiency of light collection .

Regarding the timing and image quality, research is active in the topics of *Time of Flight* (TOF) PET (see next section) and *Depth of Interaction* (DOI) (see Chapter 4).

1.10   TOF-PET

In order to improve the *Signal to Noise* (S/N) ratio (Conti, 2011), it is useful to exploit the TOF information, as can be seen from the formula:

$$SNR_{TOF} = \sqrt{\frac{D}{c \cdot \Delta t}} \cdot SNR_{no-TOF} \qquad (1.14)$$

where D is the diameter of the ring, c the speed of light and Δt the TOF resolution. As is shown in figure 1.10, the position of annihilation along the

PET/CT Model	Ingenuity TF	Discovery 710	Biograph mCT Flow TrueV)	Discovery IQ (5 rings)	Vereos
Manufacturer	Philips	GE	Siemens	GE	Philips
Crystal size (mm^3)	4×4×22	4,2×6,3×25	4×4×20	6,3×6,3×30	4×4×22
N. of crystals	28336	13824	32448	19200	23040
N. of PMTs	420	256	768	720	SiPM
Physical axial FOV (cm)	18	15,7	21,8	26	16,3
Detector material	LYSO	LYSO	LSO	BGO	LYSO
Sesitivity (%)	0,74	0,75	0,95	2,2	2,2
Transaxial res. @1cm (mm)	4,7	4,9	4,4	4,9	4,0
Transaxial res. @10cm (mm)	5,2	5,5	4,9	5,5	4,5
Axial res. @1cm (mm)	4,7	5,6	4,5	5,1	4,0
Axial res. @10cm (mm)	5,2	6,3	5,9	5,5	4,5
TOF res. (ps)	550	544	540	n.a.	345
TOF localization (cm)	8,9	8,2	8,1	n.a	5,2

TABLE 1.3: Performance comparison for various commercial full-body PET scanners by Philips, GE and Siemens (from Vandenberghe, Moskal, and Karp, 2020, Kaalep et al., 2018 and Alessio et al., 2004)

Manufacturer	Model	Transax. FOV (mm)	Axial FOV mm	Spatial res. (mm)	Sensitivity (%)	Energy window (keV)
Bioscan/ Mediso	NanoPET	45-123	94	1.2	8.3	250-750
Carastream	Albira	80	40-148	<1.3	3-9	NA
Gamma Medica / GE	LabPET	110	38-113	1.3	1.1-5.4	250-650
Philips	Mosaic HP	128	120	2.7	1.1	410-665
Raytest Isotopen.	ClearPET	94	110	1.5	1.9	250-750
Sedecal	nPET-1	68	47	1.5	0.5	250-650
Siemens	microPET Focus 120	100	76	1.3	7.1	250-750
Siemens	microPET Focus 220	190	76	1.3	3.4	250-750
Siemens	microPET Inveon DPET	100	127	1.4	9.3	250-625

TABLE 1.4: Performance comparison for various commercial small animal PET scanners (from Yao, Lecomte, and Crawford, 2012 and Mannheim et al., 2019)
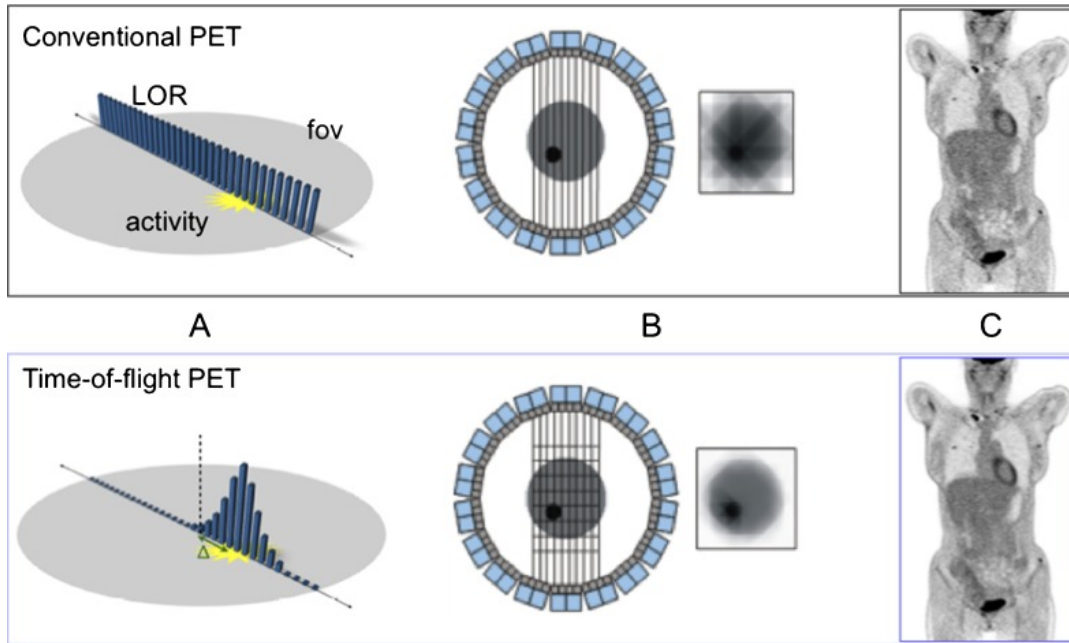
FIGURE 1.10: Schematic effect of TOF use in a PET measure
(from Beyer et al., 2011)

LOR is correlated to the time difference between the two signals inside the detector. Knowing this time difference Δt, using

$$s = \frac{\Delta t}{2} c \tag{1.15}$$

it is possible to obtain the coordinate s of the annihilation point along the LOR. In a typical whole-body PET machine, with a *Coincidence Time Resolution* (CTR) of 500ps, it is possible to reach around 7.5 cm of spatial resolution on s (Lecoq, 2017).

It is then clear from equation 1.15 that an improvement in time resolution is directly correlated to an improvement in spatial resolution along the LOR. The physics of the annihilation sets a lower limit to the best performance obtainable in the positioning of the decay point along the LOR: taking into account the range of the positron (about 1.5 mm for FDG), the best possible CTR is then about 10 ps. This would profoundly change the approach to the reconstruction process and could mean a paradigm shift in the PET field (Lecoq et al., 2020 and Schaart, Ziegler, and Zaidi, 2020).

References

Alessio, Adam M et al. (2004). "PET/CT scanner instrumentation, challenges, and solutions". In: *Radiologic Clinics* 42.6, pp. 1017–1032.

Asl, M. and A. Sadremomtaz (2013). "Analytical image reconstruction methods in emission tomography". In: *Journal of Biomedical Science and Engineering* 6.1, pp. 100–107. DOI: 10.4236/jbise.2013.61013.

Bailey, Dale L (2005). "Data acquisition and performance characterization in PET". In: *Positron emission tomography*. Springer, pp. 41–62.

Bailey, Dale L, Joel S Karp, and Suleman Surti (2005). "Physics and instrumentation in PET". In: *Positron emission tomography*. Springer, pp. 13–39.

Beyer, Thomas et al. (2000). "A Combined PET/CT Scanner for Clinical Oncology". In: *Journal of Nuclear Medicine* 41.8, pp. 1369–1379. eprint: http://jnm.snmjournals.org/content/41/8/1369.full.pdf+html. URL: http://jnm.snmjournals.org/content/41/8/1369.short.

Beyer, Thomas et al. (June 2011). "The future of hybrid imaging—part 2: PET/CT". In: 2, pp. 225–34.

Brownell, G.T. and W. H. Sweet (1953). "Localization of brain tumors with positron emitters". In: *Nucleonics* 11, pp. 40–45.

Casey, M.E. and R. Nutt (1986). "A Multicrystal Two Dimension BGO Detector System for Positron emission Tomography". In: *IEEE Transaction on Nuclear Science* 33.1, pp. 460–463. URL: http://ieeexplore.ieee.org/stamp/stamp.jsp?arnumber=4337143.

Cho, Z. H. and M. R. Farukhi (1977). "Bismuth Germanate as a Potential Scintillation Detector in Positron Cameras". In: *Journal of Nuclear Medicine* 18.8, pp. 840–844. URL: http://jnm.snmjournals.org/content/18/8/840.short.

Conti, Maurizio (2011). "Focus on time-of-flight PET: the benefits of improved time resolution". In: *European Journal of Nuclear Medicine and Molecular Imaging* 38.6, pp. 1147–1157. ISSN: 1619-7089. DOI: 10.1007/s00259-010-1711-y.

Del Guerra, A., N. Belcari, and M. Bisogni (2016). "Positron Emission Tomography: Its 65 years". In: *Rivista del Nuovo Cimento* 39.4, pp. 155–223. URL: http://dx.doi.org/10.1393/ncr/i2016-10122-6.

Eijk, C. W. E. van (2002). "Inorganic scintillators in medical imaging". In: *Physics in Medicine and Biology* 47.8, pp. 85–106. URL: https://www.ncbi.nlm.nih.gov/pubmed/12030568.

Gong, Jiaying et al. (Nov. 2014). "Diagnostic efficacy of whole-body diffusion-weighted imaging in the detection of tumour recurrence and metastasis by comparison with 18F-2-fluoro-2-deoxy-D-glucose positron emission tomography or computed tomography in patients with gastrointestinal cancer". In: *Gastroenterology report* 3. DOI: 10.1093/gastro/gou078.

Gundacker, Stefan et al. (2020). "Experimental time resolution limits of modern SiPMs and TOF-PET detectors exploring different scintillators and Cherenkov emission". In: *Physics in Medicine & Biology* 65.2, p. 025001.

Kaalep, Andres et al. (2018). "Feasibility of state of the art PET/CT systems performance harmonisation". In: *European journal of nuclear medicine and molecular imaging* 45.8, pp. 1344–1361.

Klein, Oskar and Yoshio Nishina (1929). "Über die Streuung von Strahlung durch freie Elektronen nach der neuen relativistischen Quantendynamik von Dirac". In: *Zeitschrift für Physik* 52.11-12, pp. 853–868.

Knoll, G.F. (2010). *Radiation Detection and Measurement*. John Wiley & Sons. ISBN: 9780470131480.

Lecomte, Roger (2009). "Novel detector technology for clinical PET". In: *European Journal of Nuclear Medicine and Molecular Imaging* 36.1, pp. 69–85. ISSN: 1619-7089. DOI: 10.1007/s00259-008-1054-0.

Lecoq, P (2017). "Pushing the limits in time-of-flight PET imaging". In: *IEEE Transactions on Radiation and Plasma Medical Sciences* 1.6, pp. 473–485.

Lecoq, P et al. (2010). "Factors influencing time resolution of scintillators and ways to improve them". In: *IEEE Transactions on Nuclear Science* 57.5, pp. 2411–2416.

Lecoq, Paul (2016). "Development of new scintillators for medical applications". In: *Nuclear Instruments and Methods in Physics Research Section A: Accelerators, Spectrometers, Detectors and Associated Equipment* 809.Supplement C. Advances in detectors and applications for medicine, pp. 130 –139. ISSN: 0168-9002. URL: http://www.sciencedirect.com/science/article/pii/S0168900215009754.

Lecoq, Paul et al. (2020). "Roadmap toward the 10 ps time-of-flight PET challenge". In: *Physics in Medicine & Biology* 65.21, 21RM01.

Mannheim, Julia G et al. (2019). "Reproducibility and comparability of preclinical PET imaging data: a multicenter small-animal PET study". In: *Journal of Nuclear Medicine* 60.10, pp. 1483–1491.

Moses, William W. (2011). "Fundamental limits of spatial resolution in PET". In: *Nuclear Instruments and Methods in Physics Research Section A: Accelerators, Spectrometers, Detectors and Associated Equipment* 648.Supplement

1, S236–S240. ISSN: 0168-9002. URL: http://www.sciencedirect.com/
science/article/pii/S0168900210026276.

Pizzichemi, M. (2016). "Positron Emission Tomography: state of the art and
future developments". In: *Journal of Instrumentation* 11.08, p. C08004. URL:
http://stacks.iop.org/1748-0221/11/i=08/a=C08004.

Radon, J. (1986). "On the determination of functions from their integral val-
ues along certain manifolds". In: *IEEE Transactions on Medical Imaging* 5.4,
pp. 170–176. ISSN: 0278-0062. DOI: 10.1109/TMI.1986.4307775.

Reddin, J. S. et al. (2018). "Performance Evaluation of the SiPM-based Siemens
Biograph Vision PET/CT System". In: *2018 IEEE Nuclear Science Sympo-
sium and Medical Imaging Conference Proceedings (NSS/MIC)*, pp. 1–5. DOI:
10.1109/NSSMIC.2018.8824710.

Schaart, Dennis R, Sibylle Ziegler, and Habib Zaidi (2020). "Achieving 10
ps coincidence time resolution in TOF-PET is an impossible dream". In:
Medical Physics.

Schaart, Dennis R et al. (2010). "LaBr3: Ce and SiPMs for time-of-flight PET:
achieving 100 ps coincidence resolving time". In: *Physics in Medicine & Bi-
ology* 55.7, N179.

Schmitz, Ruth E et al. (2005). "The physics of PET/Ct scanners". In: *PET and
PET/CT: a clinical guide* 3.

Surti, Suleman and Joel S Karp (2008). "Design considerations for a limited
angle, dedicated breast, TOF PET scanner". In: *Physics in Medicine & Biology*
53.11, p. 2911.

Sweet, William H. (1951). "The Uses of Nuclear Disintegration in the Diag-
nosis and Treatment of Brain Tumor". In: *New England Journal of Medicine*
245.23. PMID: 14882442, pp. 875–878. DOI: 10.1056/NEJM195112062452301.

Turtos, R Martinez et al. (2019). "Towards a metamaterial approach for fast
timing in PET: experimental proof-of-concept". In: *Physics in Medicine &
Biology* 64.18, p. 185018.

Vandenberghe, Stefaan, Pawel Moskal, and Joel S Karp (2020). "State of the
art in total body PET". In: *EJNMMI Physics* 7, pp. 1–33.

Verel, Iris, Gerard W.M. Visser, and Guus A. van Dongen (2005). "The Promise
of Immuno-PET in Radioimmunotherapy". In: *Journal of Nuclear Medicine*
46.1 suppl, 164S–171S. URL: http://jnm.snmjournals.org/content/46/
1_suppl/164S.abstract.

Vilardi, I et al. (2006). "Optimization of the effective light attenuation length
of YAP: Ce and LYSO: Ce crystals for a novel geometrical PET concept". In:

Nuclear Instruments and Methods in Physics Research Section A: Accelerators, Spectrometers, Detectors and Associated Equipment 564.1, pp. 506–514.

Yao, Rutao, Roger Lecomte, and Elpida S Crawford (2012). "Small-animal PET: what is it, and why do we need it?" In: *Journal of nuclear medicine technology* 40.3, pp. 157–165.

Chapter 2

Introduction to Radiation Detectors for Positron Emission Tomography

2.1 Introduction

The fundamental components of a radiation detector for PET application are three:

- a scintillator

- a photodetector

- readout electronics

A schematic picture of this chain is shown in figure 2.1.

The purpose of the first element, the scintillator, is to stop high-energy gamma photons and convert them into low-energy optical photons. In the case of medical applications, and in particular PET, typical energies of gamma photons are in the order of hundreds of keV, up to 511 keV (the energy of the gamma photons produced in the annihilation of an electron-positron couple). Each of these high-energy gamma photons produces in the scintillator bulk thousands of low energy optical photons (in the case of LYSO, around
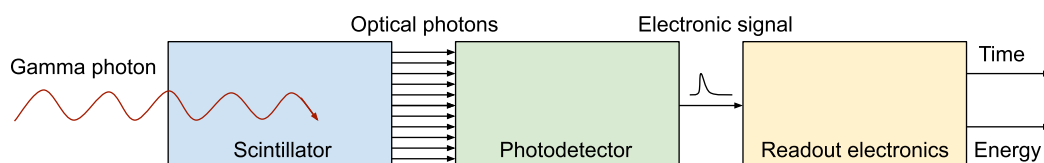
FIGURE 2.1: Schematic representation of the building blocks of a radiation detector (from Gundacker et al., 2019)

40000 photons with a wavelength of 420nm are emitted for every MeV of energy deposited in the crystal).

These optical photons travel inside the scintillator and reach the second block of the detector chain, the photodetector. This can be a Photomultiplier Tube (PMT), an Avalanche Photodiode (APD) or, more recently, a Silicon Photomultiplier (SiPM). The result of the interaction of the optical photons in the photodetector is an electronic signal which contains information regarding the light detected.

The electronic signal is then processed in the last part of the detector, the readout electronics. This last step is fundamental to obtain quantitative information relative to the original gamma photon, in particular time and energy. These quantities are later used in the reconstruction process in order to produce an image of the radiotracer inside the body of the patient.

In this chapter these three building blocks of the detector will be further discussed.

2.2 Scintillators

One of the many techniques used to detect ionizing radiation involves the use of scintillating materials. These can be made of organic or inorganic compounds and have many different applications depending on their properties (security, high-energy physics, medical physics...). In general, organic scintillators can be cheaper and faster than inorganic ones; the latter however have usually a higher density (and therefore a better stopping power) and are brighter.

In this section these two types of materials are going to be further explored.

2.3 Organic Scintillators

In organic scintillators different processes cause different types of light emission:

- *fluorescence* is the prompt emission of visible radiation

- *phosphorescence* is the emission of longer wavelength light than fluorescence, with a slower characteristic time

- *delayed fluorescence*, which has a similar profile to prompt fluorescence but characterized by a longer emission time

In the following sections these processes are going to be discussed in more detail, as well as the light output and the time response.

2.3.1 Scintillation mechanism

In organic scintillators fluorescence arise from transitions in the energy levels of a single molecule (Brooks, 1979). These levels are characteristic of a given molecular species and do not depend on its physical state. Organic scintillators can be therefore manufactured in solid, liquid or gaseous form, in contrast with inorganic scintillators which require a crystalline lattice and therefore a solid state.

Prompt fluorescence is emitted in transitions between the first excited singlet state and one of the vibrational states of the ground electronic state (Birks and Dyson, 1963). The Intensity of light emitted at time t following excitation is

$$I(t) = I_0 e^{-t/\tau} \tag{2.1}$$

where τ is the fluorescence decay time for the first excited singlet state.

If an excited singlet state is converted to a triplet state (through a process called *inter-system crossing*), the delayed light emitted in the de-excitation is called *phosphorescence*. In the case of thermal excitation back to the excited singlet state and subsequent de-excitation, the process is called *delayed fluorescence*.

2.3.2 Light Output

In organic scintillators the light yield varies greatly depending on the type of ionizing radiation. For this reason, it is useful to introduce the *MeV electron equivalent*, which is the particle energy necessary to generate the same light yield as an electron of 1 MeV. The classic way to describe the light produced as a function of the energy deposited by ionizing radiation is through Birk's formula:

$$\frac{dL}{dx} = \frac{S\frac{dE}{dx}}{1 + kB\frac{dE}{dx}} \tag{2.2}$$
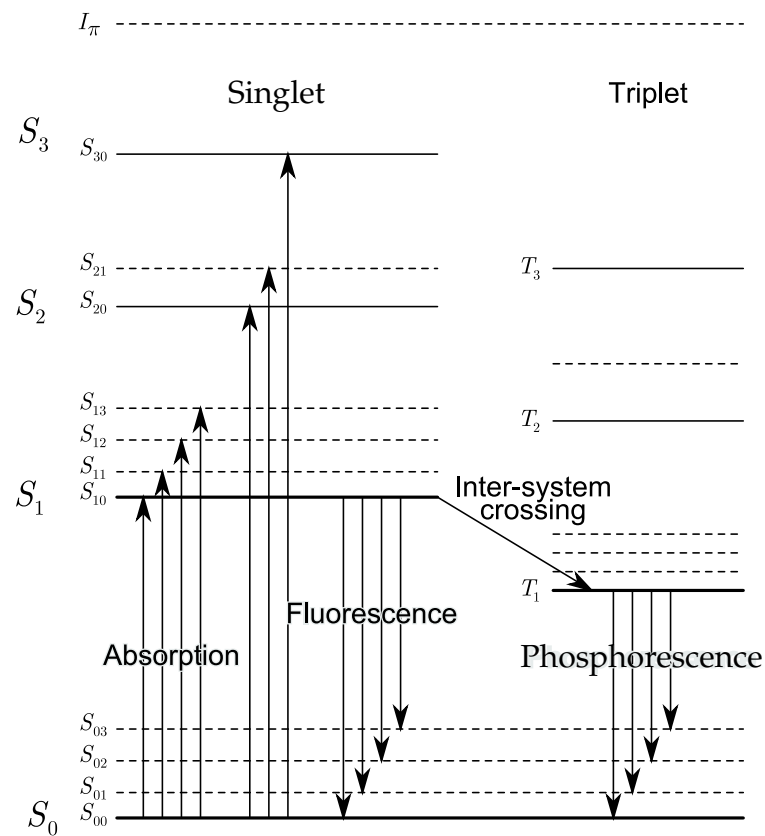
FIGURE 2.2: Energy levels of an organic molecule (from Paff, 2017)

Name	LO (% Anthracene)	Wavelenght of max emission (nm)	Decay constant (ns)	Att. length (mm)	Refractive index	Density (g/cm^3)
Anthracene	100	447	30		1.62	1.25
Stilbene	50	410	4.5		1.626	1.16
BC-422	55	370	1.4	8	1.58	1.032
EJ-204	68	408	1.8	160	1.58	1.032
NE-115	41	428	285	180	1.58	1.032

TABLE 2.1: Performance comparison for various commercially available organic scintillators (BC = St. Gobain, EJ = Eljen)

which correlates the light emitted per unit length to the energy loss (Birks, 1951); the denominator takes into account the probability of quenching: the higher the specific energy loss, the higher the quenching probability and therefore the lower the scintillation efficiency.

2.3.3 Time Response

In a first approximation, the time profile of the light pulse produced by an organic scintillator is an exponential decay that follows a sharp rise, as expressed in equation 2.1. However, it takes a finite amount of time (usually around half a nanosecond) to populate luminescent states, and delayed fluorescence and phosphorescence usually cause slower components in the decay profile. For these reasons, the overall shape of the light output can be expressed as

$$I = I_0 (e^{-t/\tau_{decay}} - e^{-t/\tau_{rise}}) \tag{2.3}$$

where τ_{rise} and τ_{decay} are respectively the time constant characteristic of the population and decay of optical levels.

2.3.4 Plastic scintillators

In a plastic scintillator an organic scintillator is dissolved in a solvent base which can be polymerized (Swank and Buck, 1953). The result is a solid solution. Common examples of solvents are *styrene monomer*, *polyvinyltoluene (PVT)* or *polymethylmethacrylate*. This production process allows for great flexibility in the shape, size and light properties of the final product. Price, in particular, favors them when large-volume detectors are needed; in these cases however, self-absorption of scintillation light must be accounted for.

BC-422

BICRON BC-422 is the commercial name of a plastic scintillator manufactured by Saint-Gobain (Crystals, 2014). It is based on polyvinyltoluene and has a light yield of 55% of Anthracene (which in turn is 40-50% of NaI(Tl)). Its decay constant (1.6ns) is one of the lowest of other materials with similar characteristics, making it particularly suitable for fast timing applications.
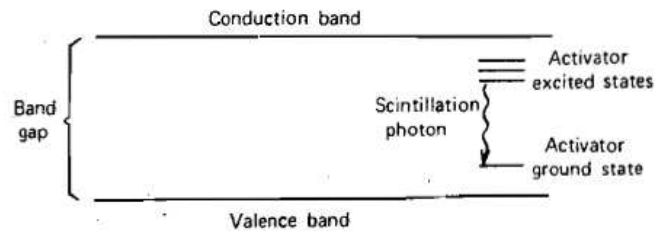
FIGURE 2.3: Energy band structure in a doped scintillating crystal (from Knoll, 2010)

2.4   Inorganic Scintillators

Scintillation mechanism

In inorganic scintillators, the crystal lattice of the material determines the energy states and therefore the scintillation mechanism (Weber, 2002). In the simplest possible model electrons can move, if excited, between two discrete energy levels: the valence band and the conduction band. In the former the electrons are bound at the site, in the latter instead they can freely move around the crystal. Once excited to the conduction band, the electron leaves behind a hole. The recombination of such electron/hole pair results in the emission of light. To ensure that the light emitted during this recombination process is not subsequently absorbed by the lattice the crystal can be doped with impurities, called activators, which cause the presence of energy levels between the valence and conduction band in the so-called forbidden gap. This way, the electron can de-excite through intermediate energy levels emitting light at a wavelength that the crystal is transparent to. The properties of the most common inorganic scintillators for medical application are shown in table 2.2.

Bismuth Germanate (BGO)

BGO is an intrinsic scintillator made of bismuth, germanium and oxygen ($Bi_4Ge_3O_12$). The high density (7,13 g/cm^3) and large atomic number (83), despite the low light yield, makes it widely used in high-energy gamma spectroscopy. Moreover, the light collection is made difficult by the high refractive index (2,15). Its time resolution is approximately 2 times worse than NaI(Tl), due to slow decay time and low light emission (Moszyński et al., 1981). BGO is an intrinsic inorganic scintillator, because it does not require an activator element to create luminescence centers. This crystal has been

Name	BGO	NaI	LSO	LaBr$_3$	LuAP
Composition	Bi$_4$Ge$_3$O$_{12}$	NaI	Lu$_2$SiO$_5$	LaBr3	LuAlO$_3$
Dopant		Tl	Ce	Ce	Ce
Density (g/cm^3)	7.1	3.67	7.4	5.3	8.34
Z_{eff}	75	51	66	46	65
Refractive Index	2.15	1.85	1.82	1.9	1.94
Attenuation Length (mm)	10.4	29.1	11.4	22.3	11
Prob. of PE effect (%)	40	17	32	14	32
LO (relative to LSO) (%)	30	137	100	200	40
I_0 (relative to LSO) (%/ns)	4	24	100	500	90
Decay time (ns)	300	230	40	16	18
Scint. emission wavelength (nm)	480	510	420	360	365
Hygroscopic	no	yes	no	yes	no

TABLE 2.2: Properties of various scintillating crystals for PET application (adapted from Eijk, 2002), Lecoq, 2016 and Lecomte, 2009

used for many years in the medical imaging industry thanks to the high sensitivity associated with BGO based systems and the research is now focused on the possibility to exploit the fast component (60 ns, 10% LY fraction) of its light emission. There is currently a renovated interest in this material because of the presence of prompt Cerenkov photons in the emission spectrum. The number of photons is still low (few dozens of photons per MeV) but could be exploited to achieve better Coincidence Time Resolution.

Fast Inorganics

Since the late 1960s Cerium started to be used as an activator in new categories of scintillators, fast and bright (Holloway and Kestigian, 1969). The transition from $5d$ to $4f$ state in a cerium activator site, in particular, is characterized by a luminescence decay time of 20 to 80 ns (depending on the host crystal); this set these scintillators closer to organics compared to more classical inorganic detectors. Popular choices for host crystals are rare earth halides and oxides, such as yttrium, lanthanum, gadolinium and lutetium. Those 3 last elements constitute the group of lanthanoid scintillators, characterized by a high density and effective Z and therefore suitable for gamma spectroscopy.

LYSO

Rare earth oxyorthosilicates (Ln_2SiO_5 or $Ln(SiO_4)O$, where Ln is either Y, Gd or Lu) is a family of scintillators that include LYSO, a commercially available scintillating crystal of mixed composition widely used in medical imaging (Positron Emission Tomography in particular). LSO was described for the first time in 1991 (Bescher et al., 2000). It is characterized by a light yield of around 40000 photons per MeV, by a fast decay time (between 40 and 50 ns), and has an emission spectrum peaking at 420 nm. The ^{126}Lu isotope, which represents 2,59% of the natural element, is radioactive (250 Bq/cm^3) and contributes to the other radioactive contaminants of LSO. This fact discourages any low background application but is fortunately of low importance in PET applications since the spectrum of intrinsic radioactivity does not superimpose to the 511 keV photopeak (the decay chain for lutetium-176 is shown in figure 2.4) (Moses and Derenzo, 1999 and Moszynski et al., 2006).

The mixed composite LYSO was developed to combine the best properties of LSO (high yield and high stopping power) and YSO (favorable growth
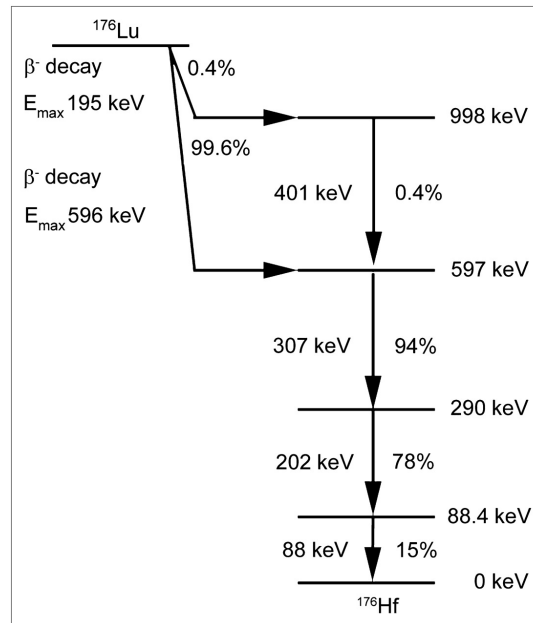
FIGURE 2.4: Schematic of lutetium-176 decay (from Green et al., 2016)

and cost). The different yttrium fractions in the final blend accounts for the difference in density of the available products.

2.5 Scintillator Properties

2.5.1 Light Output

Once scintillation light is produced, the next critical step is to collect as much of it as possible. In this sense, it is necessary to distinguish between intrinsic light yield and light output:

- intrinsic light yield is the total amount of photons produced inside the scintillating material;

- light output is the amount of light that exits the scintillator and collected by the photodetector.

For any type of material, the theoretical limit for light output can be calculated as:

$$LO_{th}^{lim} = LTE \times \frac{S \cdot Q}{b \cdot E_G} \tag{2.4}$$

(Moszynski et al., 1997), where

- *LTE* is the Light Transfer Efficiency of the crystal and is a function of the transparency of the material to its own emission light, index of refraction and attenuation length;

- *S* is a factor that accounts for the energy transfer efficiency from the deposition center to the luminescent centers;

- *Q* is the quantum efficiency of the latter;

- *b* is the correcting factor for phonon losses for

- E_G, which is the band gap energy.

The product of the two terms at the denominator is the energy to produce an electron-hole pair. For a typical crystal used in medical applications, the value of LO is around few tens of thousands of photons per MeV

2.5.2   Energy resolution

Energy resolution is usually quoted as the ratio between the FWHM of a peak (ΔE) and the full energy of the peak itself (*E*). Its value is given by the sum of several terms (Dorenbos, Haas, and Van Eijk, 1995):

- statistical contribution δ_{st}: it is proportional to the inverse of the square root of the number of detected photons:

$$\delta_{st} = 1/\sqrt{N_{ph}} \qquad (2.5)$$

  It represents the Poisson nature of the error associated with photon counting and represents the theoretical limit;

- intrinsic energy resolution δ_{intr}: it is caused by the non linearity in the response of the detector to low energy photons and electrons;

- scintillator light transfer and photodetector conversion resolution δ_{phot};

- photodetector dark noise contribution δ_{dn}.

These last two terms are determined by the crystal and photodetector characteristics (size, shape, coupling and their performances).

In figure 2.5 is shown an overview of different scintillating materials compared to the theoretical Poisson limit (the photostatistics contribution).
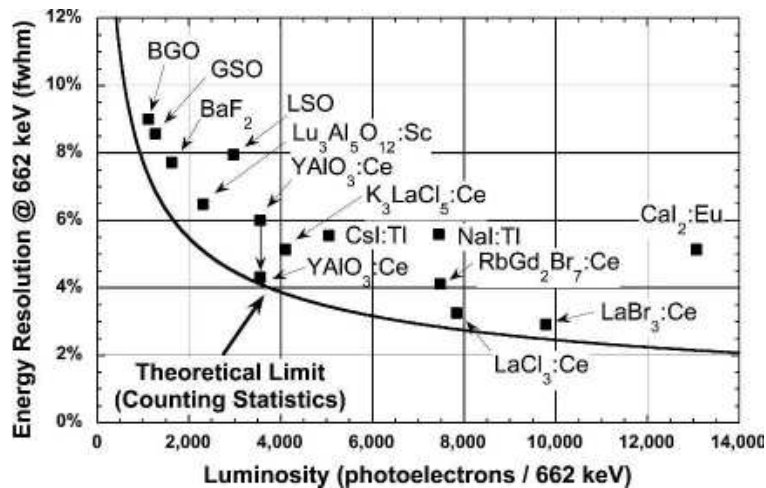
FIGURE 2.5: Energy resolution for different materials used as scintillators REF (from Milbrath et al., 2008)

2.5.3 Time resolution

The timing properties of a scintillating crystal are critically dependent on the time profile of the emitted light pulse (Melcher, 2000). The process of light emission can be divided into three steps:

- creation of electronic excitations (10^{-16} to 10^{-10} seconds);

- transfer to luminescent scenters (10^{-10} to 10^{-8} seconds);

- e-h recombination, which leads to light emission.

More in detail, in the case of a 511 keV gamma photon, the interaction with the material can happen through the photoelectric effect or Compton scatter. In both cases, the result is the production of "hot" electrons that start the multiplication process via inelastic electron-electron scattering and the Auger effect (0.1-10 fs). After this phase, the thermalization of carriers continues through phonon interaction (10 fs - 1 ps), until each electron is in the minimum energetic level of the conduction band. At this point electrons and holes start the recombination phase, which results in luminescent centers emitting photons.

In the case of a simple bi-exponential light emission pulse, the first photon gives the best time resolution. However, photon transport inside the crystal and photodetector SPTR result in the situation where the best time information is obtained waiting for the first n photons to arrive at the photodetector.
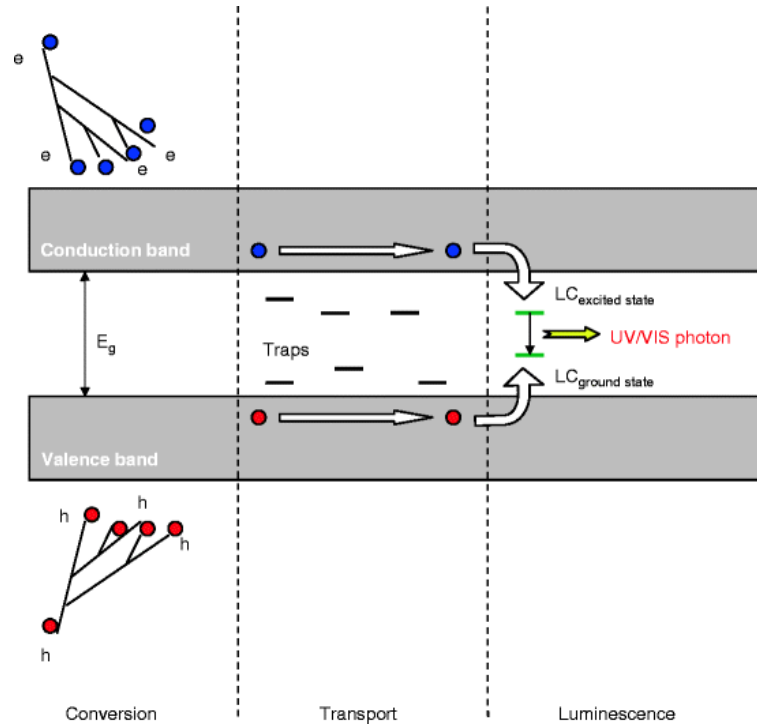
FIGURE 2.6: Conversion, transport and luminescence phases in inorganic scintillators (from Nikl, 2006)

2.6 Photodetectors

One of the most common ways to read the light emitted by a scintillating crystal is using a PhotoMultiplier Tube (PMT). For Positron Emission Tomography applications, PMTs have been used in commercial PET scanners up to recent years, when Silicon-based photodetectors (SiPM or APD) gained popularity (Henseler et al., 2009).

2.6.1 Photomultiplier Tubes

A Photomultiplier Tubes (PMT) is a photodetector made of two main components: a transparent window coupled to the crystal, and an electron multiplier structure (Lubsandorzhiev, 2006). The transparent window, called *photocathode*, is made of a material that converts scintillating light in photoelectrons. These electrons are then accelerated inside the tube by an electric field, multiplied by various dynodes and finally reach an anode where the current, proportional to the charge gathered, is read. The overall signal gain can be expressed as

$$gain = \alpha \delta^N \tag{2.6}$$
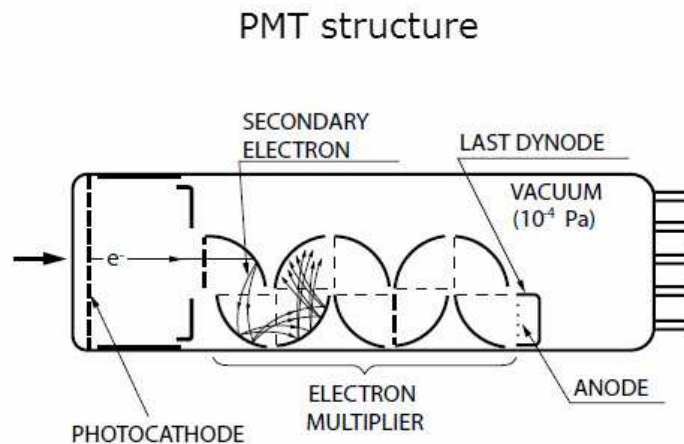
PMT structure

FIGURE 2.7: PMT structure (image from Hamamatsu)

where α is the fraction of photoelectron collected, δ the multiplication factor for the single dynode (typical values of 5, up to more than 50) and N is the number of stages.

Typical values for the electrons produced at the end of the multiplication stage are between 10^7 to 10^{10}; the pulse itself lasts usually a few nanoseconds and is produced with a delay of few tens of nanoseconds.

These photodetectors have a low efficiency of light collection (around 20 to 30%), they are sensitive to the electric and magnetic fields and they need high voltages in order to operate. A scheme of a standard PMT is shown in figure 2.7.

2.6.2 Silicon Photomultipliers

An Avalanche Photodiode (APD) is a photodiode that is able to convert optical photons in a current pulse using a reverse-biased p-n junction (Stillman and Wolfe, 1977). This is possible thanks to the voltage applied across the depletion region: when scintillation photons produce electron-hole pairs in this volume, these free electrons are accelerated and acquire sufficient kinetic energy to produce new electron-hole pairs. In this process, the number of free carriers is amplified and avalanches are formed, causing a microscopic variation of the electric field inside the junction. The structure of a single APD is shown in figure 2.8.

A Silicon Photomultiplier (SiPM) is based on multiple Single Photon Avalanche Diodes (SPADs), which are APD operating in Geiger mode (Piemonte and
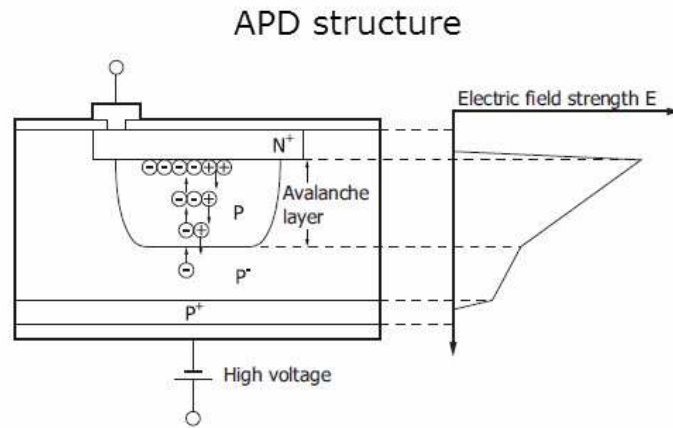
FIGURE 2.8: APD structure (image from Hamamatsu)

Gola, 2019): a single photon triggers an avalanche that discharges the APD; the total electric signal is given by the sum of all the currents by all APDs. SiPMs are also known as Multi Pixel Photon Counter (MPPC) and their SPADs as G-APD (Geiger-mode APD).

These Silicon photomultipliers are insensitive to magnetic fields, require low voltage to operate compared to a PMT and are much smaller. A schematic representation of a SiPM with its circuit components is shown in figure 2.9.

Gain

The signal produced by the SiPM is the sum of the signal produced by each G-APD. In turn, the output signal of each cell is always the same, regardless of the number of photons that started the avalanche. The gain G can therefore be expressed as:

$$G = \frac{C \times V_{ov}}{q} \tag{2.7}$$

where C is the cell capacitance, V_{ov} is the bias overvoltage (operating reverse bias voltage minus the breakdown voltage) and q is the electron charge. Typical values for G are in the order of 10^5 to 10^7 and are enough to produce a single photon signal above the electronic noise.

Because the breakdown voltage is strongly dependent on the operating temperature, in order to keep the value of the bias overvoltage (and therefore the Gain) the same, it is necessary to carefully keep the temperature stable; in alternative, the bias voltage can be modified to compensate for the temperature change.
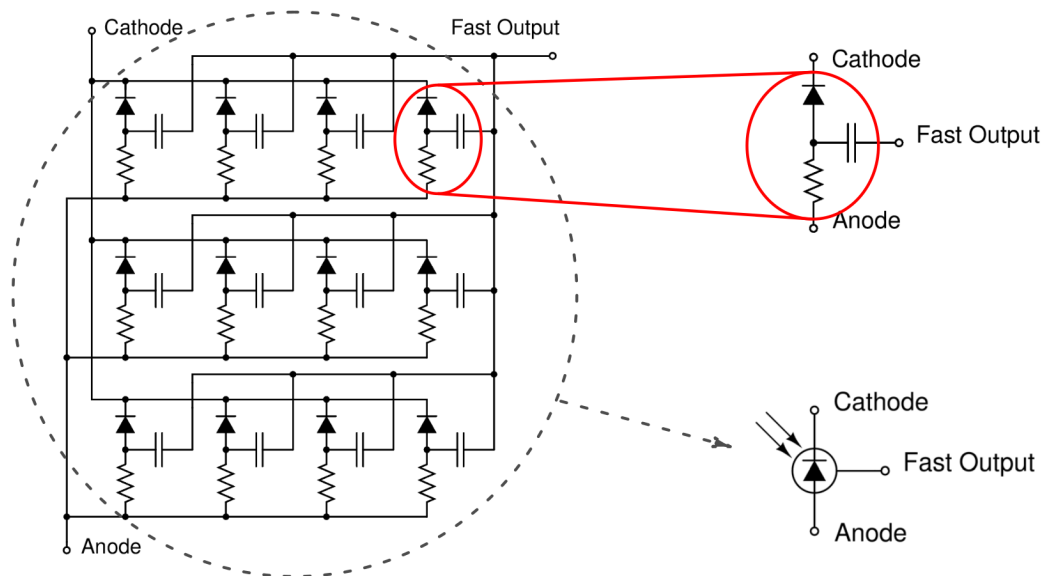
FIGURE 2.9: Simplified circuit schematic of a SiPM (Left) show-
ing each microcell which is composed of the SPAD, quench re-
sistor and fast output capacitor (top right) (image from SensL)

Quenching

In order to stop the current flow during the breakdown phase of photode-
tection, a so-called quenching resistor is placed in series with the photodi-
ode (a scheme of the circuit is shown in figure 2.9). By so doing, during an
avalanche, the current that starts flowing in the circuit causes a voltage drop
across the resistor R_q, which increases until the operational voltage of the cell
is below the breakdown voltage. At this point the avalanche stop and the cell
can start the recovery process.

Noise

In a SiPM noise can be divided into uncorrelated and correlated Noise.

The main example of uncorrelated noise is dark count, the random appear-
ance of an electron-hole pair in the depletion zone that trigger a breakdown.
The Dark Count Rate (DCR) is typically between 100kHz to a few MHz at
room temperature. This phenomenon can have a thermal origin (*thermally
generated DCR*), or can be caused by the operational voltage (*field assisted
DCR*). These two components can be reduced by decreasing respectively the
temperature and the bias voltage.

Correlated Noise on the other hand can be caused by optical cross-talk or
afterpulsing:
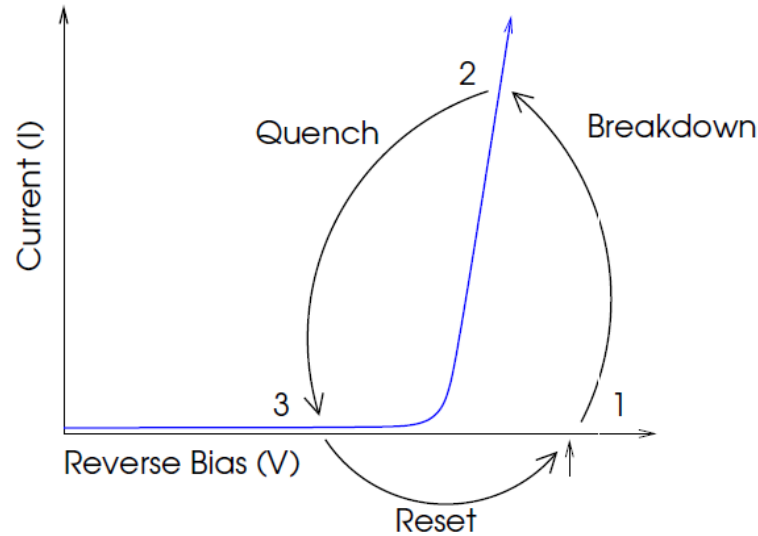
FIGURE 2.10: Breakdown, quenching and reset in a SiPM cell
(image from SensL)

- cross-talk happens *during* the breakdown: during the discharge of one cell few photons escape and trigger the discharge of neighboring cells. This type of noise can be avoided by placing optical trenches between the cells of the SiPM;

- afterpulsing happens instead *following* the breakdown: carriers can be trapped and released after the discharge, causing a second, less intense discharge.

Photon Detection efficiency

The probability of a single photon to trigger a spad to produce a pulse is called Photon Detection Efficiency (PDE) and can be expressed as:

$$PDE = QE \cdot \epsilon \cdot P_{trigger} \tag{2.8}$$

where

- QE is the Quantum Efficiency; it can reach values up to 90% for the active area and is a function of the wavelength of the optical photon;

- ϵ is the fill factor: it is defined as the ratio between the photosensitive area and the total surface of the SiPM;

- $P_{trigger}$ is the probability of an electron-hole pair to trigger an avalanche; it increases as the bias overvoltage increase.

The PDE for modern SiPMs reaches values up to 60%, compared to much lower values of PMTs (20-30%).

Recovery time

After every photon interaction, the avalanche is quenched and the cell is charged again. The time necessary for this process is called Recovery Time, and its time constant can be expressed as:

$$\tau_{recovery} = R_{quenching} \cdot C \tag{2.9}$$

where $R_{quenching}$ and C are the parameters of the quenching circuit. Given the proportionality of τ on R_q, and the dependence of the latter on the operation temperature of the SiPM, it is clear that the recovery time itself is a parameter of the temperature.

Typical values of 100 $k\Omega$ and 100 fF result in a recovery time of tens of nanoseconds. This value is kept as low as possible to maintain better linearity of the response of the SiPM.

Saturation

In a first approximation, the pulse produced by a SiPM upon receiving a certain quantity of light is proportional to the number of photons interacting with the single Spad cells. However, the finite number of cells present in a SiPM reduces the maximum amplitude of the signal produced for a given bias. For this reason, the intrinsic behavior of SiPMs is characterized by a saturation effect, which can be expressed with:

$$N_{firedcells} = N_{total} \cdot (1 - \exp(-\frac{N_{photons} \cdot PDE}{N_{total}})) \tag{2.10}$$

where N_{total} is the number of cells present in the SiPM and $N_{photons}$ is the number of optical photons exciting the photodetector. The difference in incident light required to switch from linear to saturation regime for SiPMs with a different number of cells is shown in figure 2.11.
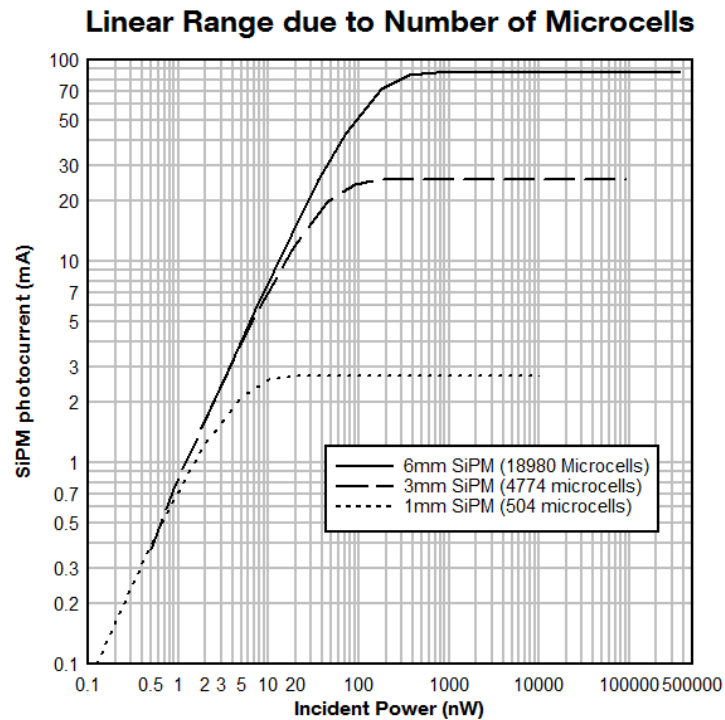
FIGURE 2.11: Saturation behaviour for SiPMs with different number of cells (SensLblu)

2.7 Electronics

The electronic board used in this thesis for the shaping of the signal coming from the SiPM for timing applications is called NINO (Anghinolfi et al., 2003).

NINO is an ultrafast front-end amplifier and discriminator. It was originally developed for Time Of Flight (TOF) particle discrimination in the ALICE experiment at CERN (Aamodt, 2008). The particular environment of operation of this module led to strict requirements in terms of speed, noise and slew rate. Moreover, the need to minimize signal reflection and cross-talk led to low input impedance (Anghinolfi et al., 2004).

The recent version of the NINO chip is based on a 0.25 μm CMOS technology and measures $2mm^2$. It is made of 32 channels, each able to process the signal in differential form, from input to output.

Each NINO channel is made of an input stage, followed by 4 cascade amplifiers and an output driver which adapt the output signal to the LVDS standard. The input stage is a current to voltage converted based on a common gate circuit; a voltage difference applies the threshold to the input stage. The
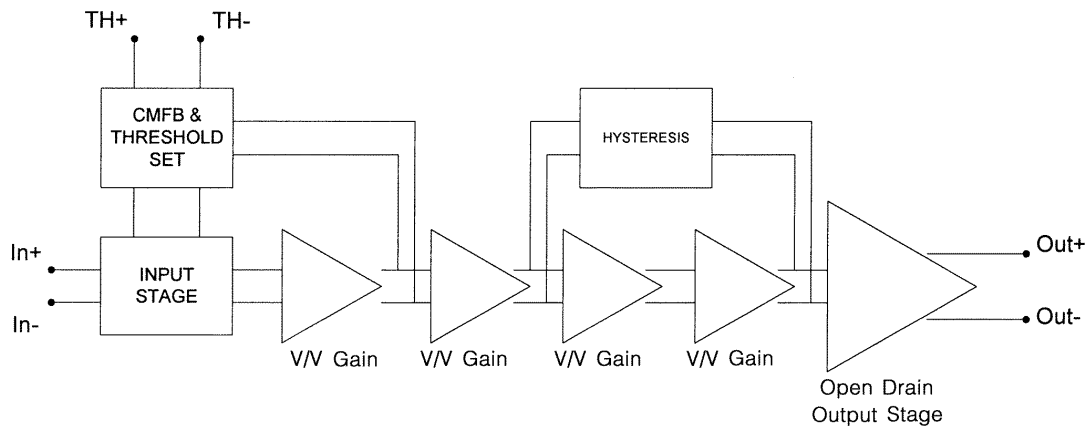
FIGURE 2.12: Schematic representation of the NINO chip (from Anghinolfi et al., 2004)
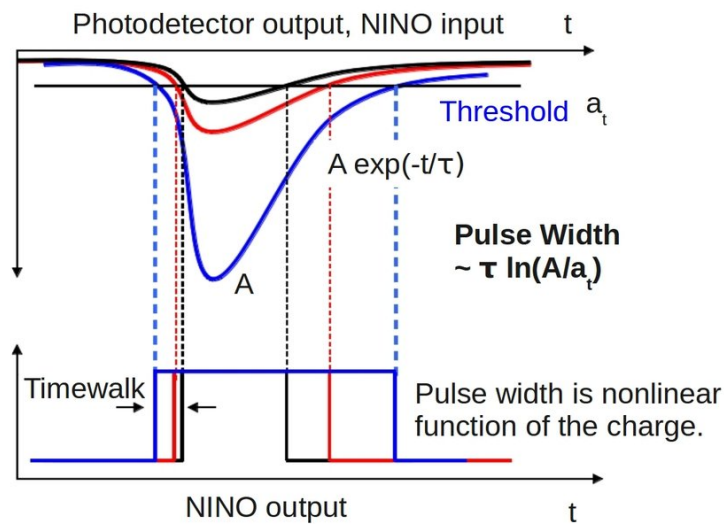
FIGURE 2.13: Output pulse of the NINO chip (from Gundacker et al., 2013)

following cascade amplifiers, producing a factor 6 factor gain, allow using NINO as a discriminator.

The output is a square pulse that carries both time and energy information: the leading edge provides a time stamp correlated to the input pulse (leading edge discrimination) and the pulse duration is correlated to the Time Over Threshold (TOT), therefore carrying information regarding the input pulse charge.

References

Aamodt, K. et al. (2008). "The ALICE experiment at the CERN LHC". In: *JINST* 3, S08002. DOI: 10.1088/1748-0221/3/08/S08002.

Anghinolfi, F et al. (2003). "NINO, an ultra-fast, low-power, front-end amplifier discriminator for the Time-Of-Flight detector in ALICE experiment". In: *2003 IEEE Nuclear Science Symposium. Conference Record (IEEE Cat. No. 03CH37515)*. Vol. 1. IEEE, pp. 375–379.

Anghinolfi, F et al. (2004). "NINO: an ultra-fast and low-power front-end amplifier/discriminator ASIC designed for the multigap resistive plate chamber". In: *Nuclear Instruments and Methods in Physics Research Section A: Accelerators, Spectrometers, Detectors and Associated Equipment* 533.1-2, pp. 183–187.

Bescher, Eric et al. (2000). "New lutetium silicate scintillators". In: *Journal of Sol-Gel Science and Technology* 19.1-3, pp. 325–328.

Birks, John B and DJ Dyson (1963). "The relations between the fluorescence and absorption properties of organic molecules". In: *Proceedings of the Royal Society of London. Series A. Mathematical and Physical Sciences* 275.1360, pp. 135–148.

Birks, John Betteley (1951). "Scintillations from organic crystals: specific fluorescence and relative response to different radiations". In: *Proceedings of the Physical Society. Section A* 64.10, p. 874.

Brooks, FD (1979). "Development of organic scintillators". In: *Nuclear Instruments and Methods* 162.1-3, pp. 477–505.

Crystals, Saint-Gobain (2014). *BC-418, BC-420, BC-422.*

Dorenbos, P, J Th M de Haas, and CWE Van Eijk (1995). "Non-proportionality in the scintillation response and the energy resolution obtainable with scintillation crystals". In: *IEEE Transactions on Nuclear Science* 42.6, pp. 2190–2202.

Eijk, C. W. E. van (2002). "Inorganic scintillators in medical imaging". In: *Physics in Medicine and Biology* 47.8, pp. 85–106. URL: https://www.ncbi.nlm.nih.gov/pubmed/12030568.

Green, Michael V et al. (2016). "Investigation of factors affecting a potential worldwide network of medical PET scanners to monitor the decay rate of Lu-176 and detect global radiation events". In: *2016 IEEE Nuclear Science Symposium, Medical Imaging Conference and Room-Temperature Semiconductor Detector Workshop (NSS/MIC/RTSD)*, pp. 1–3.

Gundacker, Stefan et al. (2013). "Time of flight positron emission tomography towards 100ps resolution with L (Y) SO: an experimental and theoretical analysis". In: *Journal of Instrumentation* 8.07, P07014.

Gundacker, Stefan et al. (2019). "High-frequency SiPM readout advances measured coincidence time resolution limits in TOF-PET". In: *Physics in Medicine & Biology* 64.5, p. 055012.

Henseler, Debora et al. (2009). "SiPM performance in PET applications: An experimental and theoretical analysis". In: *2009 IEEE Nuclear Science Symposium Conference Record (NSS/MIC)*. IEEE, pp. 1941–1948.

Holloway, WW and M Kestigian (1969). "Optical properties of cerium-activated garnet crystals". In: *JOSA* 59.1, pp. 60–63.

Knoll, G.F. (2010). *Radiation Detection and Measurement*. John Wiley & Sons. ISBN: 9780470131480.

Lecomte, Roger (2009). "Novel detector technology for clinical PET". In: *European Journal of Nuclear Medicine and Molecular Imaging* 36.1, pp. 69–85. ISSN: 1619-7089. DOI: 10.1007/s00259-008-1054-0.

Lecoq, Paul (2016). "Development of new scintillators for medical applications". In: *Nuclear Instruments and Methods in Physics Research Section A: Accelerators, Spectrometers, Detectors and Associated Equipment* 809.Supplement C. Advances in detectors and applications for medicine, pp. 130 –139. ISSN: 0168-9002. URL: http://www.sciencedirect.com/science/article/pii/S0168900215009754.

Lubsandorzhiev, Bayarto K (2006). "On the history of photomultiplier tube invention". In: *Nuclear Instruments and Methods in Physics Research Section A: Accelerators, Spectrometers, Detectors and Associated Equipment* 567.1, pp. 236–238.

Melcher, Charles L (2000). "Scintillation crystals for PET". In: *Journal of Nuclear Medicine* 41.6, pp. 1051–1055.

Milbrath, Brian D et al. (2008). "Radiation detector materials: An overview". In: *Journal of Materials Research* 23.10, pp. 2561–2581.

Moses, William W and SE Derenzo (1999). "Prospects for time-of-flight PET using LSO scintillator". In: *IEEE Transactions on Nuclear Science* 46.3, pp. 474–478.

Moszyński, M et al. (1981). "Timing properties of BGO scintillator". In: *Nuclear Instruments and Methods in Physics Research* 188.2, pp. 403–409.

Moszynski, M et al. (1997). "Absolute light output of scintillators". In: *IEEE Transactions on Nuclear Science* 44.3, pp. 1052–1061.

Moszynski, M et al. (2006). "New prospects for time-of-flight PET with LSO scintillators". In: *IEEE Transactions on Nuclear Science* 53.5, pp. 2484–2488.

Nikl, Martin (2006). "Scintillation detectors for x-rays". In: *Measurement Science and Technology* 17.4, R37.

Paff, Marc (2017). "Organic Scintillation Detectors for Spectroscopic Radiation Portal Monitors". PhD thesis.

Piemonte, Claudio and Alberto Gola (2019). "Overview on the main parameters and technology of modern Silicon Photomultipliers". In: *Nuclear Instruments and Methods in Physics Research Section A: Accelerators, Spectrometers, Detectors and Associated Equipment* 926, pp. 2–15.

Stillman, GE and CM Wolfe (1977). "Avalanche photodiodes". In: *Semiconductors and semimetals*. Vol. 12. Elsevier, pp. 291–393.

Swank, Robert K and Warren L Buck (1953). "The scintillation process in plastic solid solutions". In: *Physical Review* 91.4, p. 927.

Weber, Marvin J (2002). "Inorganic scintillators: today and tomorrow". In: *Journal of Luminescence* 100.1-4, pp. 35–45.

Chapter 3

The experimental setup

3.1 Introduction

In this chapter we are going to present the tools that were used for the measure throughout the thesis (DOI extraction, timing correction using DOI and Compton events recovery).

In the first part, we are going to present a PET module configuration that allows for DOI extraction and timing optimization using DOI information. Then we will move to the readout electronics and Data Acquisition system (DAQ) that were developed to maximize performance. Finally, we are going to characterize the setup in terms of energy, time and spatial resolution.

3.1.1 Description of the modules

The detector module is composed of a matrix of LYSO crystals, a photodetector, a light guide and a layer of reflective material.

The matrix of crystals is made of 16 or 64 LYSO pixels, each $3.1 \times 3.1 \times 15$ mm^3 or $1.53 \times 1.53 \times 15$ mm^3, with polished or depolished lateral surfaces, produced by Crystal Photonics INC. For some studies matrices of 64 LYSO $1.53 \times 1.53 \times 30$ mm^3 pixels and 144 LYSO $1.0 \times 1.0 \times 15$ mm^3 pixels were also used.

The photodetector is a 4x4 TSV MPPCs array from Hamamatsu (S13361-3050-AE-04), shown in 3.1a. Each SiPM measures 3.0×3.0 mm^2, with 3.2 mm pitches, and is composed of 3584 SPADs. The pixels are coupled to it by means of a 3M Optical Clear Adhesive (OCA 8172CL), $50 \mu m$ thick.

(A)

(B)   (C)
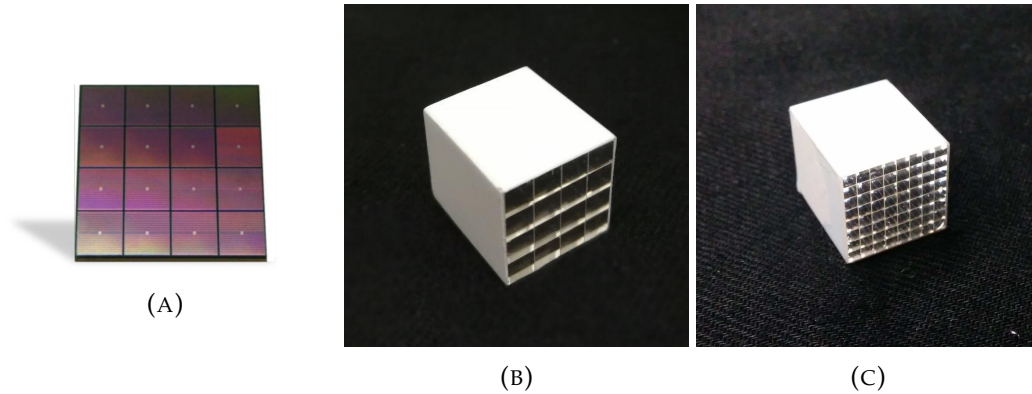
FIGURE 3.1: The SiPM (A), the 4x4 LYSO matrix (B) and the 8x8
LYSO matrix used in our module

The light guide is placed on the face of the matrix opposite to the photodetector. It consists in a 1mm Plexiglas tile, coupled to the detector with 3M OCA 8146-5, 125 μm thick.

The reflective layer is a 3M Enhanced Specular Reflector (ESR) foil ($70\mu m$ thickness), in dry contact with the light guide.

The matrix is wrapped in multiple layers of Teflon and the back hold in place using insulating tape.

The naming scheme used throughout the thesis for the crystal pixels and the SiPM channels in both 1:1 and 4:1 couplings is described in figure 3.2. In particular, having the photodetector the same number of channels in both cases, these are identified by a capital letter from A to D and a number from 1 to 4 (following the naming scheme of the manufacturer, Hamamatsu). Each crystal pixel C_i^j is identified instead by two indexes, i and j, running from 0 to 7 in the two directions of the plane defined by the SiPM array.

3.2 Description of the experimental setup

The DOI encoding method, which will be presented in section 4.2, is based on the accurate measurement of charge seen by the different channels in the SiPM array. The time correction technique, which will be explained in section 4.3, exploits this information to improve the coincidence time resolution. For these reasons, it is fundamental to measure charge and timing with the best possible energy and time resolution. This was achieved by developing a custom Front End Board (FEB) that splits the signal from each SiPM array
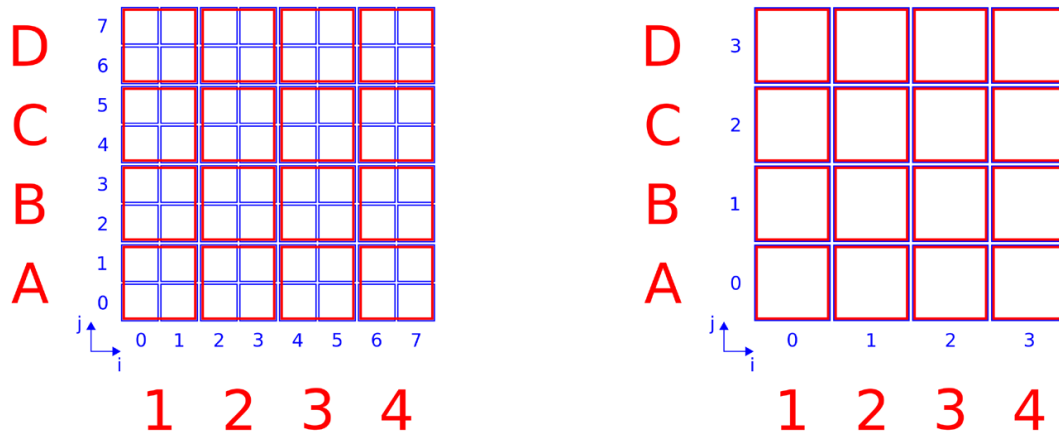
FIGURE 3.2: Naming scheme for crystal pixels and photodetector channels in 1:1 and 4:1 coupling

channel into two, and by setting up two parallel chains for the signal processing, one for the energy and one for the time measurement.

3.2.1 The Front End Board

The FEB is designed to host up to two SiPMs arrays, each with up to 16 channels, via Samtec connectors. The signal from each of these channels is split in two: the first is fed to a NINO chip and subsequently to the timing chain of the DAQ, the other is amplified and directed into the energy section of the DAQ.

The output of the board is therefore a number 2N of signals, N being the number of SiPM channels, plus a Sum signal which is the sum of all the charge signals; this signal is fundamental for trigger purposes, as will be explained later on.

The board is connected to multiple power supplies, necessaries to bias the SiPMs, to power the NINO chip and to amplify the charge signal.

A picture of the FEB is shown if figure 3.4: on the left, perpendicular to the board, the NINO chip is visible; on the right we can see the 32 amplifiers (one for each SiPM channel) as well as the connector for the flat cable used to carry the charge signal. The LEMO connectors are used for biasing purposes and for the Sum signal output.
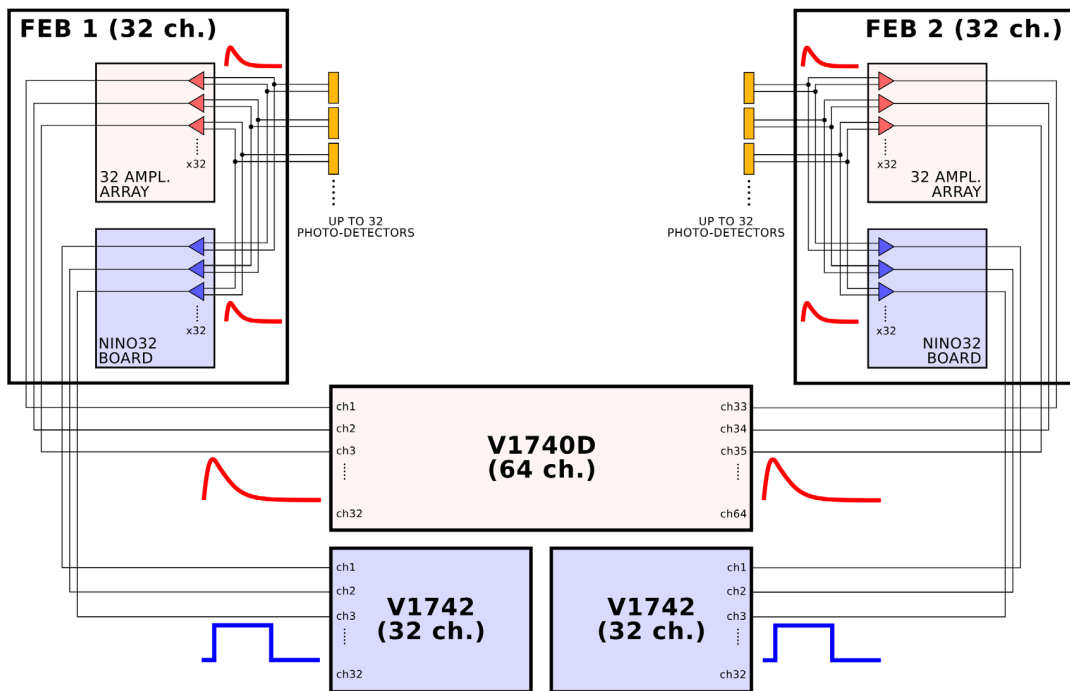
FIGURE 3.3: Scheme of the DAQ system
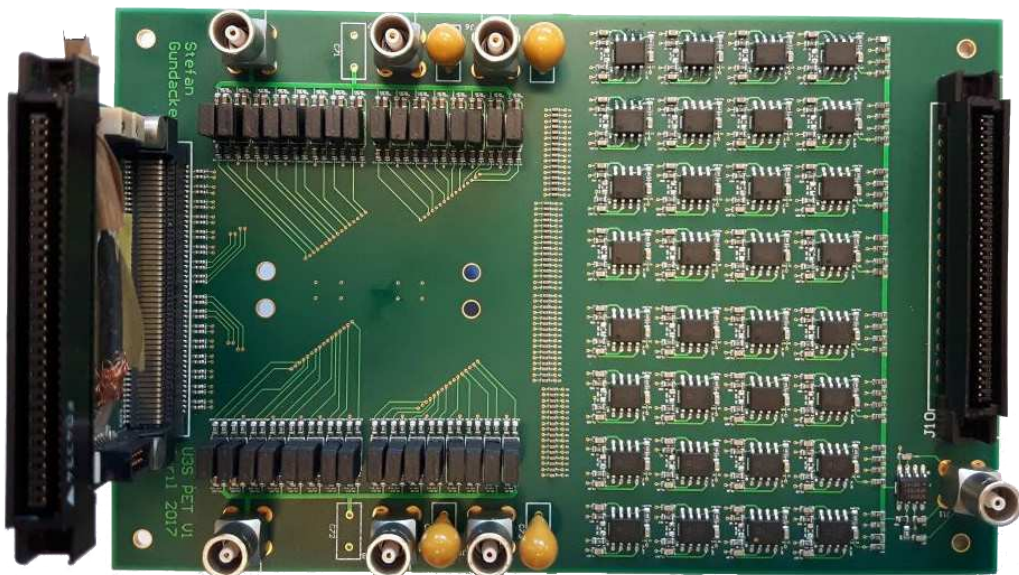
FIGURE 3.4: Picture of the FEB

3.2.2 Mechanical components

Depending on the applications, the FEBs were mounted on linear or rotational stages:

- linear stages from Zaber (model T-LRS150B) were used to move one of the two FEBs in the two directions of the plane perpendicular to the axis described by the reference crystal and sodium source. A picture of the setup is shown in figure 3.5: the FEB is mounted on one stage which in turn is connected to another one, to allow the movement of the FEB in two directions. This is the configuration used for DOI calibration measurements of Chapter 4 and Compton calibration measurements of chapter 6;

- rotational stages from Oriental Motors (model DGM130R-ARBC) were used for the point source reconstruction described in subsection 3.3.3. In this case, each stage was connected to a steel arm on which the FEB was held in place, in a configuration shown in figure 3.6

In both cases, the stages are connected to the computer used to run the acquisition and controlled by the main readout software, using secondary Python scripts: this way it was possible to automatize the steps and speed up the time required to complete long scans involving multiple acquisition positions.

3.2.3 The black box

The FEBs, the PET modules, the radioactive source and the stages are housed in a black box. The temperature inside the box is kept stable at 16C by an external cooling system (HRS018-AF-20-BM from SMC) and is monitored through a temperature sensor connected with a Raspberry Pi, connected to the main PC and controlled with a python script.

On one side of the box, a series of patch panels, mezzanines and holes allow connecting the electronics inside with the external section of the DAQ system. In particular, the positive and negative signals of each channel coming from the NINO chip are summed (after the inversion of the negative one) in order to obtain a single signal with a higher amplitude. This is done, for each FEB, in the mezzanine shown in figure 3.5.
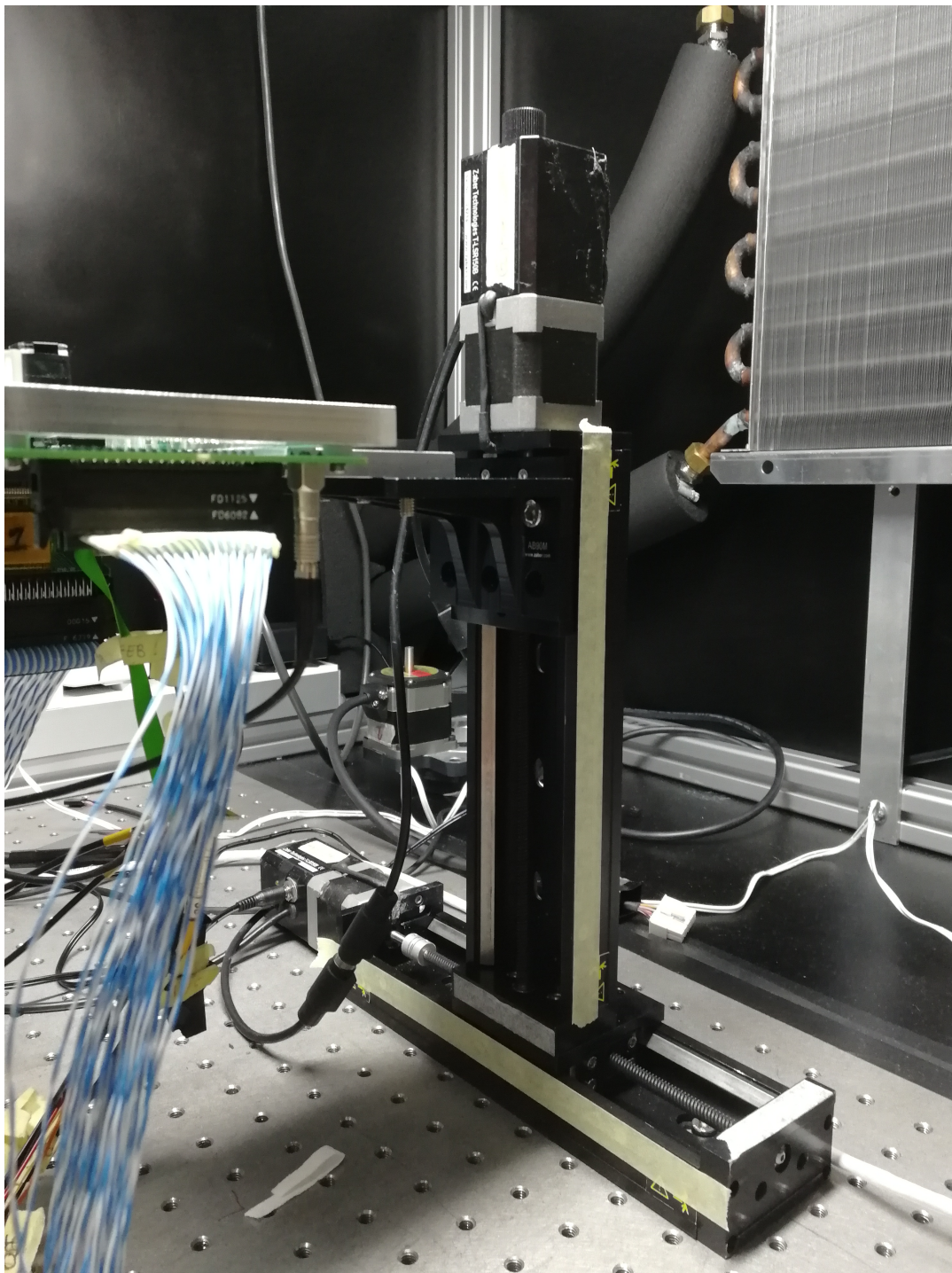
FIGURE 3.5: Scheme of the linear stages used to move one of
the two FEBs
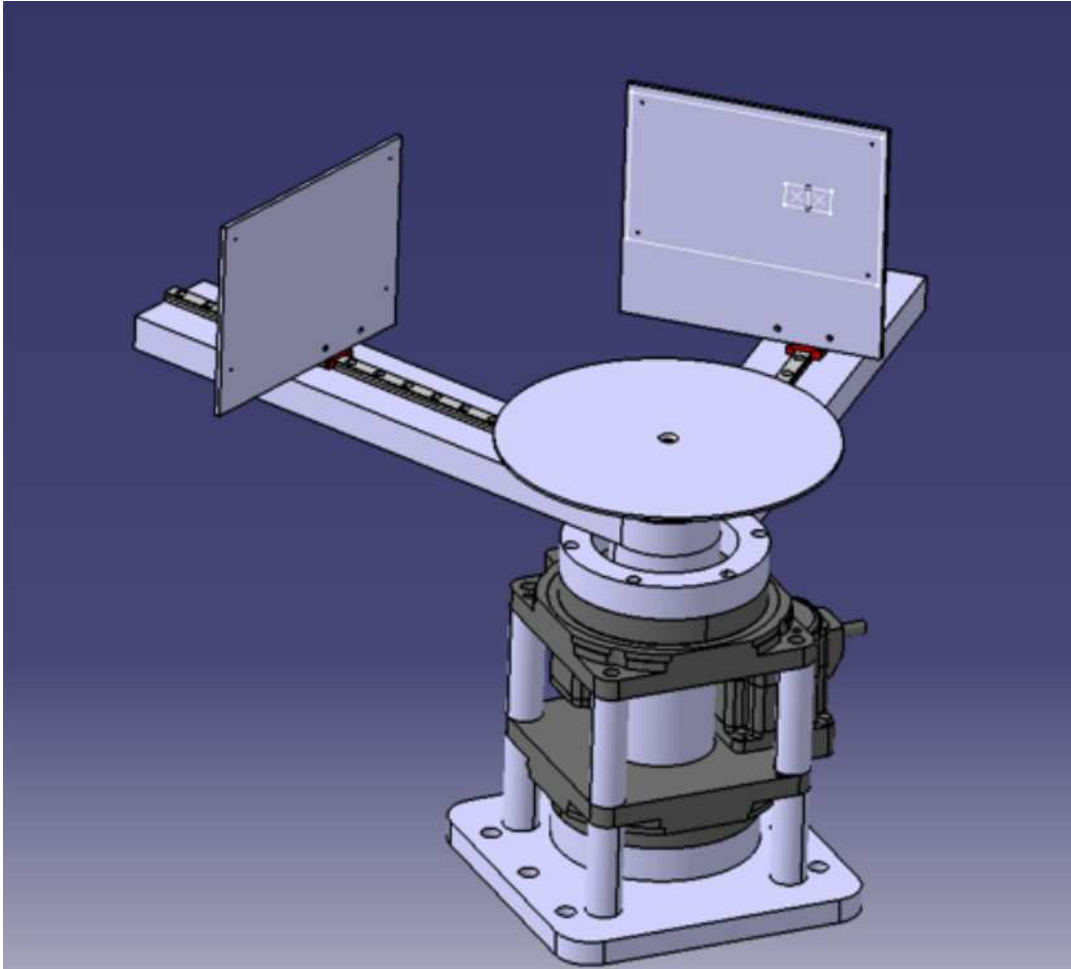
FIGURE 3.6: Scheme of the setup involving the two OM rotational stages (image courtesy of Oscar Sacristan De Frutos)

(A)

(B)
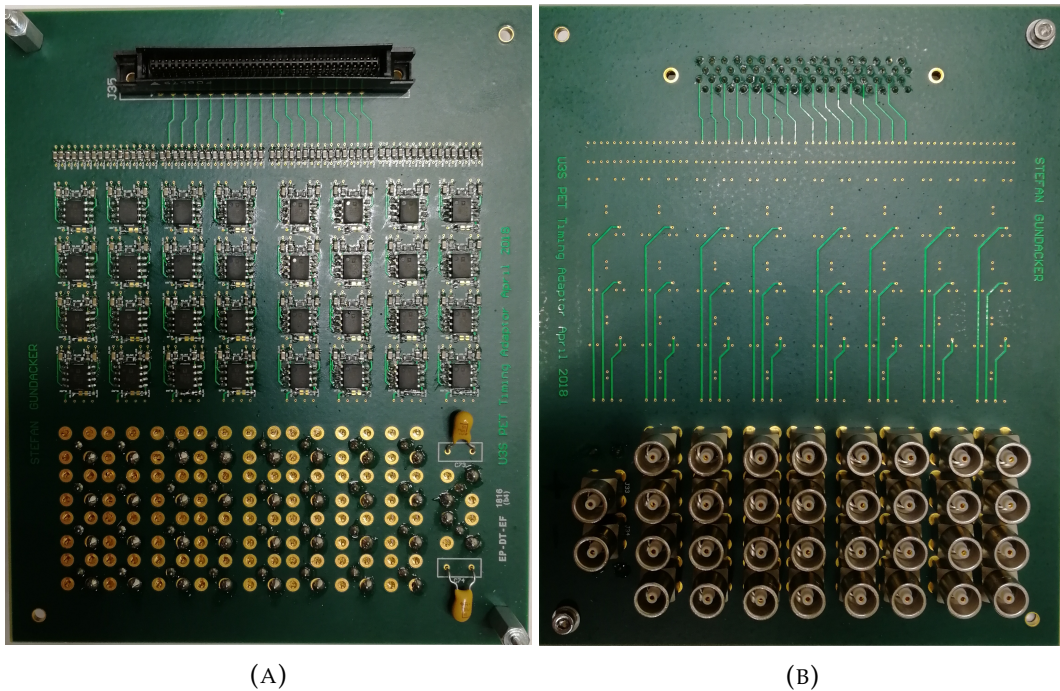
FIGURE 3.7: Pictures of the mezzanine installed on the patch panel of the black box, one for each FEB. Left: side of the mezzanine facing the inside of the box, with the black connector on top for the flat cable coming from the NINO chip and the electronic components in the middle to operate the conversion from differential signal to single-handed signal for each channel. Right: side of the mezzanine facing the outside of the box, with the LEMO connectors at the bottom used to feed the signal from each channel of the FEB to the TDC board via LEMO/MCX cables
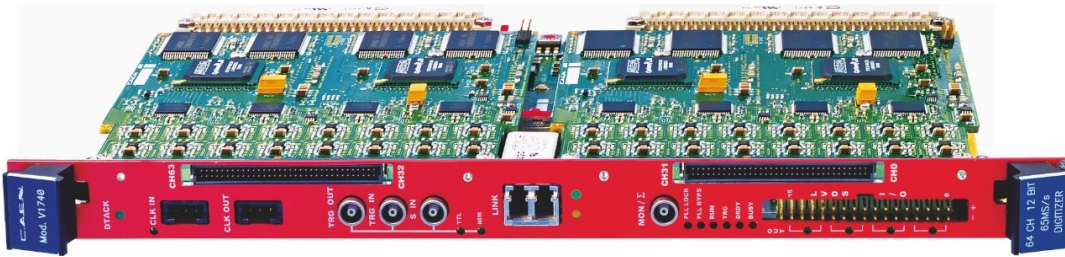
FIGURE 3.8: Picture of a Caen V1740D ADC

A patch panel allows to power all the components inside the box, through LEMO connectors on both sides of the panel. In particular, the two SiPMs arrays are connected through LEMO cables to two external Low Voltage Power supplies from Caen (model DT5485), one for each SiPM array, which are connected to the PC and remotely controlled through a Python script: this allowed to quickly complete Voltage scans and to remotely change the parameters of the acquisition.

Finally, simple holes are used to pass through the flat cables carrying the charge signals (and feeding them to the ADC module), the cable used to control the stages and the Ethernet cable for the Raspberry Pi.

3.2.4   Energy chain

The charge signal, preliminarily amplified by the FEB, is fed to a 32 channels Analog to Digital Converter (ADC) by Caen, model V1740D (shown in figure 3.8). This module samples the signal with a frequency of 62.5 MS/s. The digital signal is subsequently integrated by the FPGA present on the module itself, and for each event the values of the integrals of the signals from each channel are dumped to the computer through an optical fiber cable.

3.2.5   Timing chain

The time signal, output of the NINO chip, is fed to two Time to Digital Converters (TDC) by Caen (V1742, shown in figure 3.9), one for each FEB. These modules are based on a DRS4 chip and sample the signal with a frequency of 5 GS/s. In this case, the output of the NINO chip is a square pulse: the TDC FPGA digitize it (1024 points, 200 ps apart) and the waveform is subsequently sent to the PC via optical link and analyzed by the DAQ software: the timestamp for each pulse is computed as the intersection of the rising edge with a fixed threshold, which corresponds as 50% crossing of the rising edge.
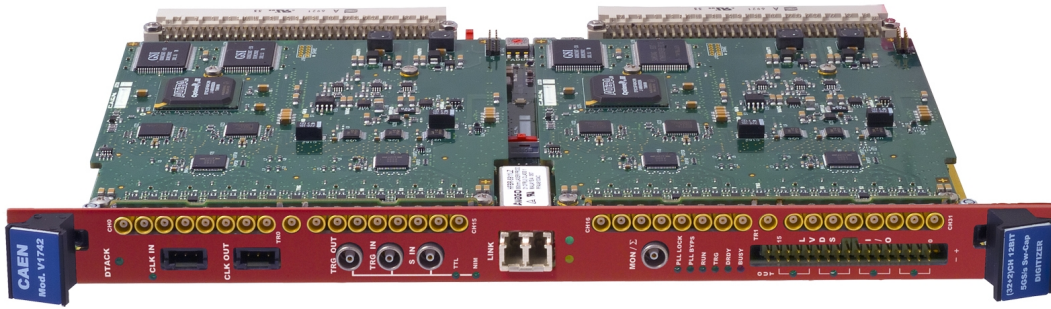
FIGURE 3.9: Picture of a Caen V1742 TDC

3.2.6   The trigger system

The Sum channel of the two FEBs is used to generate the trigger. This involves several NIM modules and is done in multiple steps:

- the Sum signal from each FEB is inverted using a Lecroy 428F FAN IN/FAN OUT to match the following modules input requirements;

- the inverted signal is fed to a LRS 623A Octal Discriminator with fixed threshold: if the signals are high enough, they produce a square pulse;

- one of the two square pulses is extended in time using a Caen 2255B Dual Timer module, in order to account for the different relative distances between radioactive source and detectors;

- the square pulses are used as input in a LRS 622 Quad Coincidence module (with AND/OR switches), which produce as output, depending on the application, a square pulse if the input pulses are overlapping or if only one input is present;

- the coincidence square pulse is multiplied and fed to each Caen board, to provide a trigger timestamp (TTT)

3.2.7   The readout software

The output of each of the three boards is saved in a separate file. The output of the V1740 ADC board is saved as it is, given that is already the integral of the charge signal. For each event, the board saves the TTT (trigger timestamp) and the charge values of the 64 channels. The output of the two V1742 TDC boards is instead analyzed online to extract the timestamp. Also in this case, each board saves the TTT and the 32 timestamps, one for each channel. Once the data acquisition is finished, the software parses the 3 files and

compares the TTTs, matching those close enough to be considered relative to the same event. The output of this procedure is a single file that contains, for each event, the TTT, 64 charges and 64 timestamps. The final step is to convert this file in ROOT format for the offline analysis. This readout software, which governs the acquisition of the 3 Caen boards, also controls the 2 low voltage power supply for the SiPMs arrays and the movement of the stages eventually involved in the acquisition, either the linear or the rotation one.

A scheme of the cables connecting the FEBs to the DAQ system and the Trigger propagation is shown in figure 3.10.

3.3 Characterization of the setup

3.3.1 Time resolution

The intrinsic time resolution of the system was tested using a sodium-22 source, a small LYSO pixel and a SiPMs array. A scheme of the setup is shown in figure 3.11. The signal from the SiPMs array is split in two and fed to two different channels of the system. The measured time difference between the two signals is used to fill the histogram in figure 3.12. The FWHM of the histogram is used as an estimation of the intrinsic time resolution for the two channels under study. A histogram with the values of different channel couples is shown in figure 3.13 for FEB number 1 and in figure 3.14 for FEB number 2. The average is 21 ± 2 ps and 19.9 ± 1.9 ps respectively.

3.3.2 Energy resolution

In order to evaluate energy resolution, it was necessary to preliminarily calibrate the system. In fact, there are two points to consider: first of all, that the output of the ADC is in arbitrary units and that the response of the SiPM array saturates. This means that a calibration function between the ADC channels and the energy deposited has to be found; moreover, because of the saturation of the photodetector, this function is not linear (Van Dam et al., 2010).

For the energy calibration multiple gamma ray sources of different emission energies were used. The complete list of sources used is reported in table 3.1. In order to calibrate all the channels of each SiPM array at the same time, the photodetector was coupled with a matrix of LYSO crystals, and the matrix was irradiated with a wide beam.
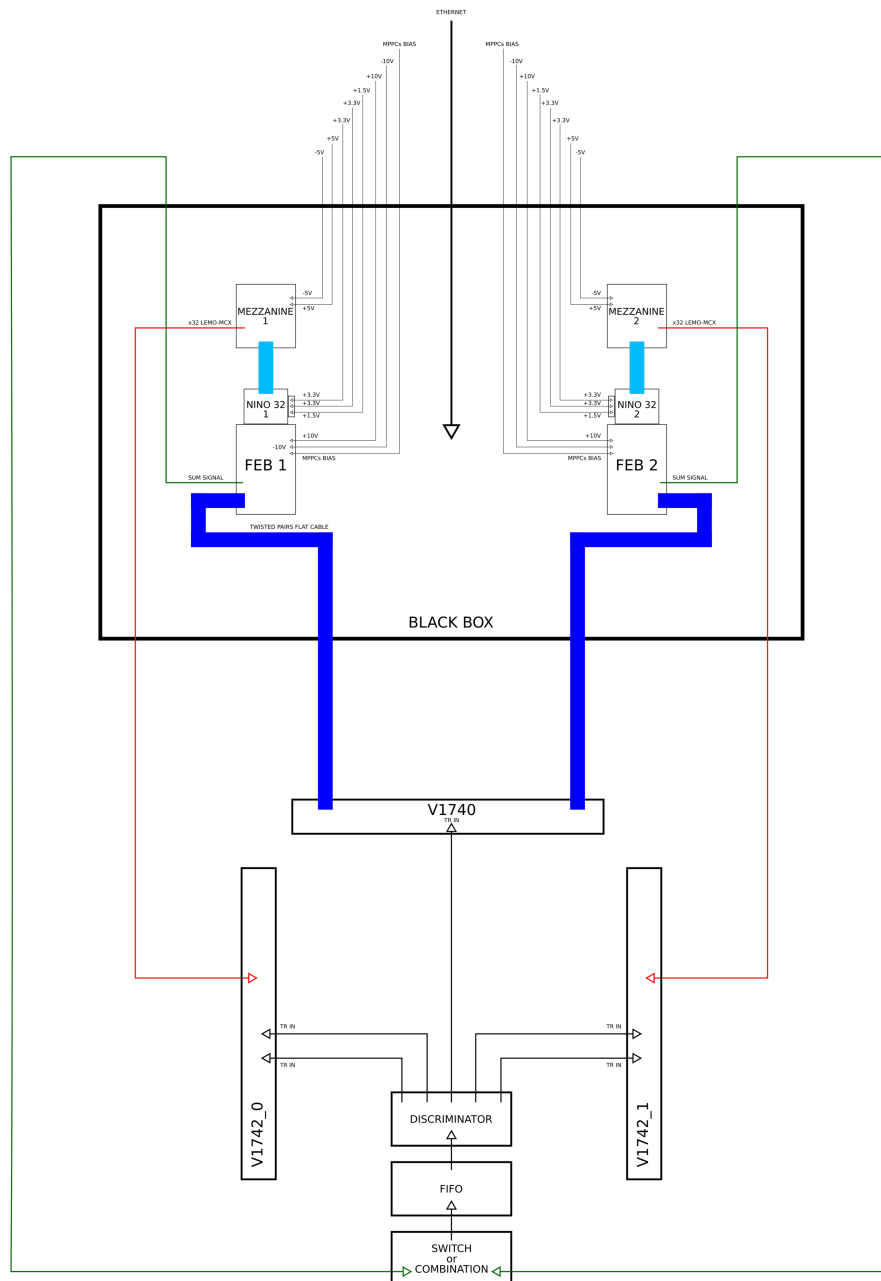
FIGURE 3.10: Scheme of the connections between FEBs, DAQ and PC
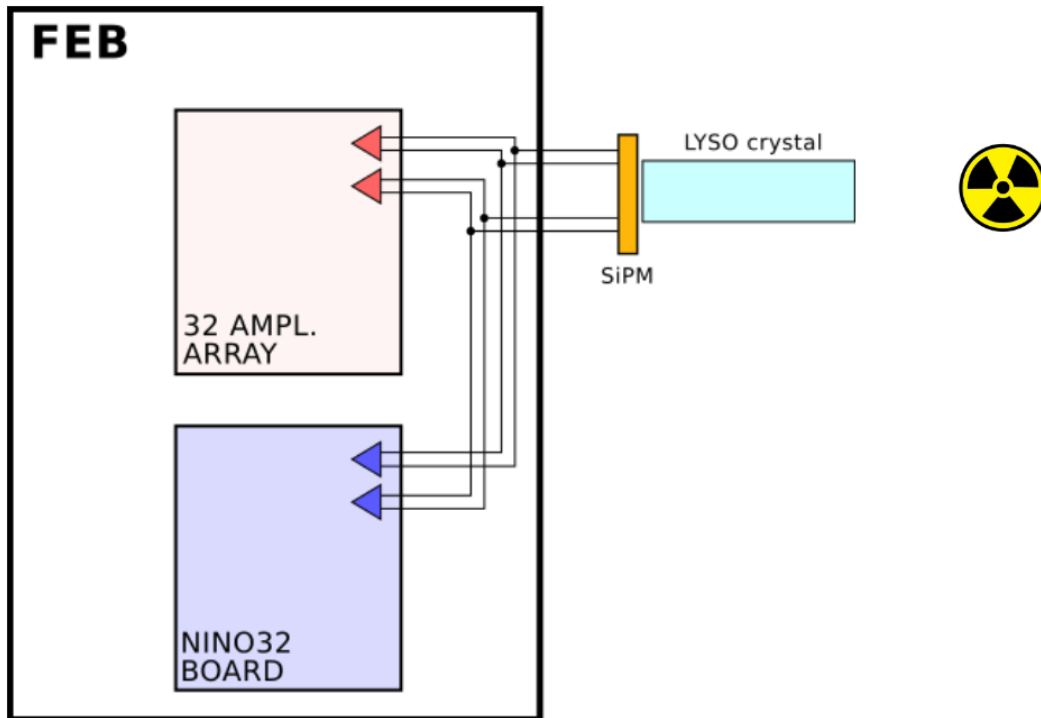
FIGURE 3.11: Scheme of the setup used to determine the intrinsic time resolution of the system
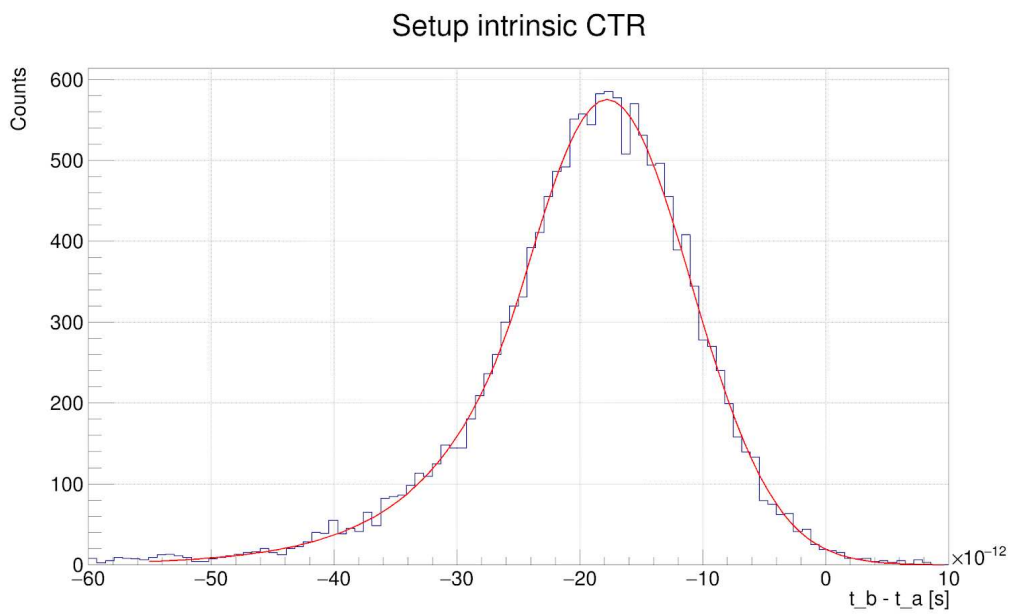
FIGURE 3.12: Intrinsic CTR of the system for one couple of channels measured with the setup shown in figure 3.11
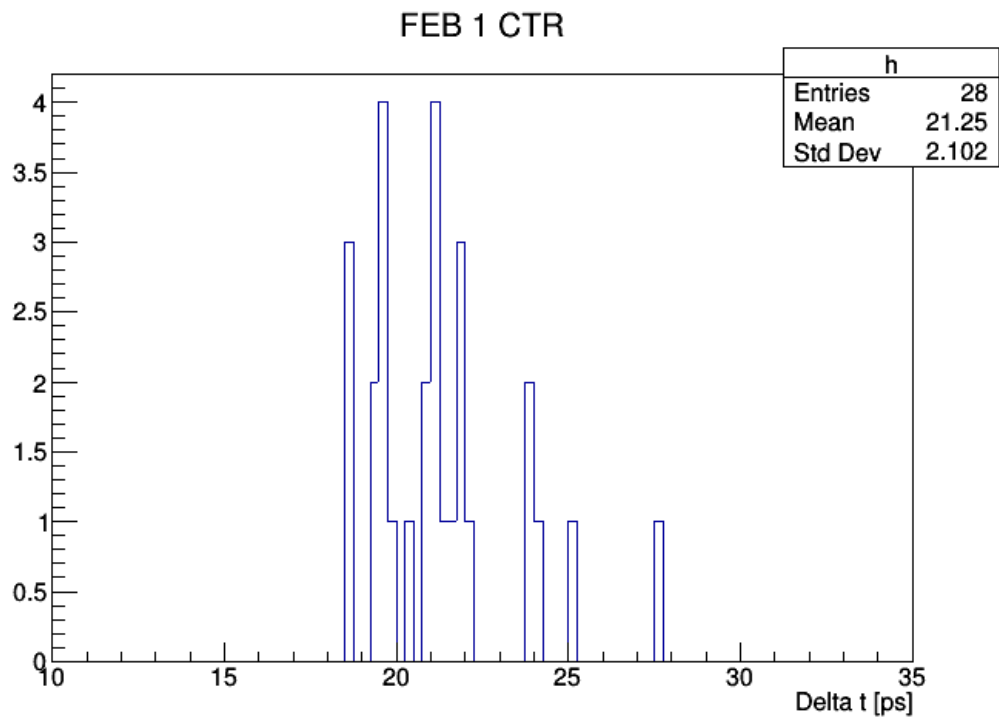
FIGURE 3.13: CTR values for different channels couples of FEB
1
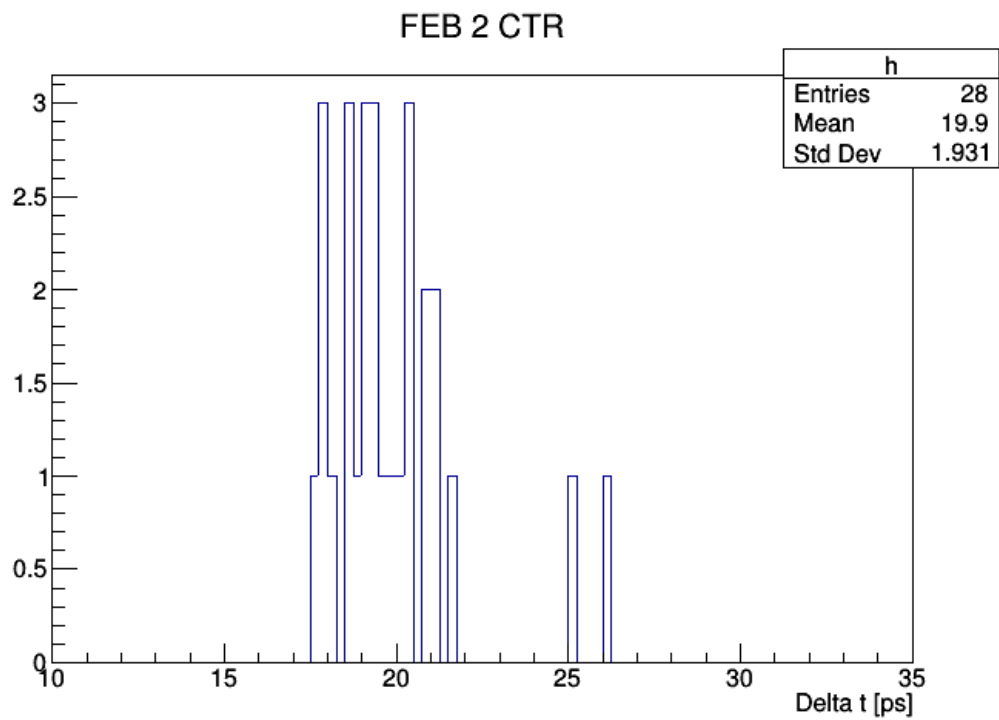
FIGURE 3.14: CTR values for different channels couples of FEB
2

Element	Emission Energy [keV]
Lu-176	202
Lu-176	307
Na-22	511
Co-60	1173
Na-22	1274
Co-60	1333

TABLE 3.1: Isotopes and respective energies used for the saturation calibration of the photodetector

For each SiPM array channel, the position of the photopeak for each spectrum was plotted against the nominal energy of the source for all the different sources, including the internal radioactivity of LYSO (Bircher and Shao, 2012). An example of these plots is shown in figure 3.15 for one the SiPM array channels; as we can see, the experimental points are fitted with an exponential function:

$$ADC_{ch} = a \cdot \left(1 - exp \left[-\frac{E_{source} \cdot b}{a} \right] \right) \tag{3.1}$$

where a and b are fit parameters.

This function was chosen because of the behavior of the SiPMs: given the finite number of SPAD in each SiPM, the response of the SiPM to a high amount of light tends to saturate, with the highest possible output corresponding to all cells firing at the same time (Acerbi and Gundacker, 2019). The saturation calibration was repeated at different bias voltages of the photodetector, in order to obtain the parameters for any operational voltages. The saturation functions for different bias V are shown in figure 3.16. As we can see, the gain of the SiPM increase as the operational voltage increase. These fit functions were used as calibration functions from this point onward.

From the spectra of the sodium source corrected for saturation the energy resolution at 511 keV was computed for all SiPM array channels, and the average is found to be 9.5 ± 0.2 % FWHM for the 4×4 module and 9.9 ± 0.2
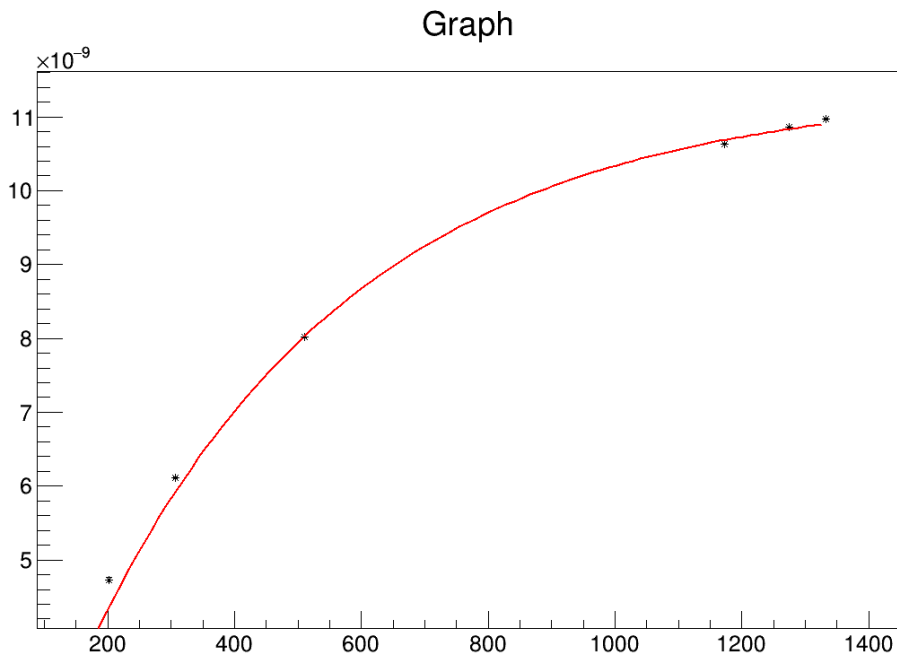
FIGURE 3.15: Saturation function for one of the 16 channels of
the SiPM array as the fit of multiple sources peaks positions
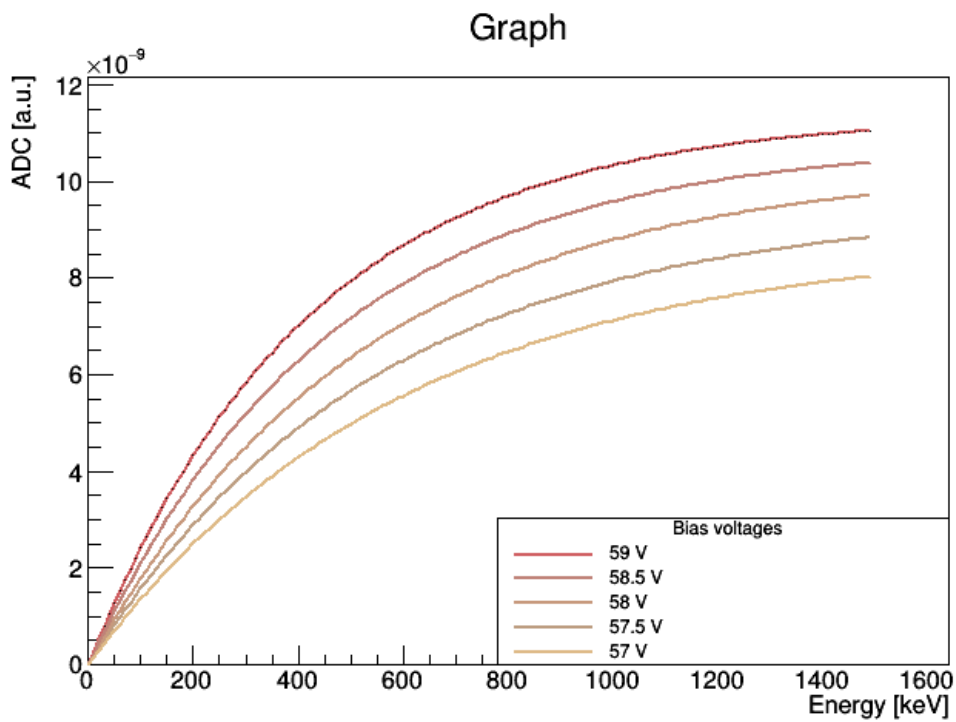
FIGURE 3.16: Saturation functions for one of the 16 channels of
the SiPM array at different voltages
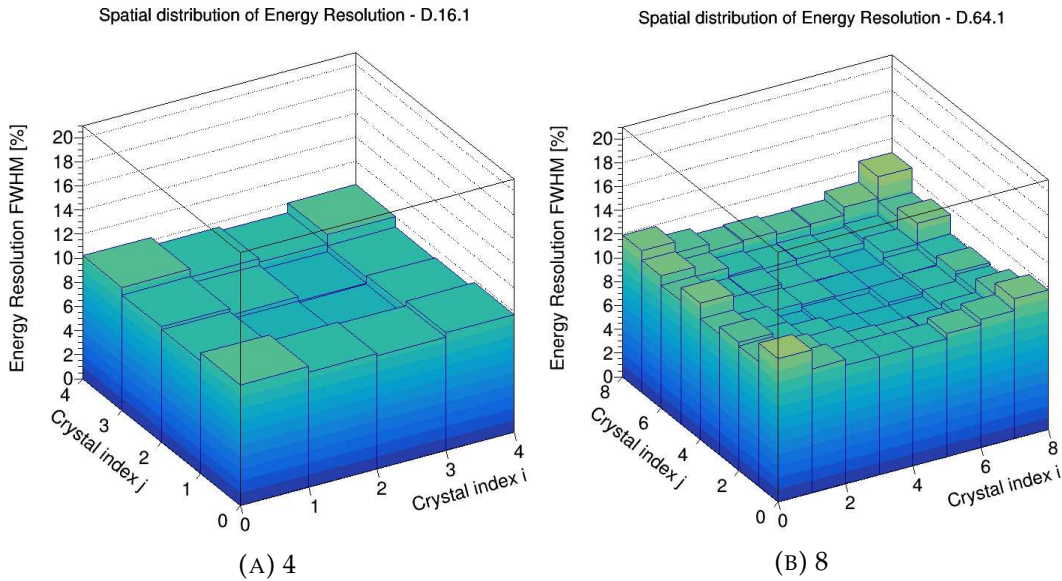
FIGURE 3.17: Spatial distribution of energy resolution for 4 (left) and 8 (right) modules

% FWHM for the 8×8 module (in both cases, for this measurement were used polished LYSO matrices without light sharing).

3.3.3 Spatial Resolution

The spatial resolution was measured reconstructing a sodium-22 point source and later a couple of sodium-22 point sources with two matrices of LYSO. Each matrix is made of 64 $1.53 \times 1.53 \times 15\text{mm}^3$ LYSO pixels coupled to a 4x4 TSV MPPCs array from Hamamatsu (S12642-0404PB-50). The matrices are mounted on two identical FEBs as described above, fixed on steel arms connected to two stages, free to rotate independently. The single source was placed at the center of the Field Of View; the two sodium-22 sources were placed at the center of the Field Of View as well, 1cm apart. A picture of the setup is shown in figure 3.18.

The acquisition is carried out in multiple steps. For every position of the first matrix, the second one moves on the opposite side, in order to cover all the possible Line Of Response. The procedure is repeated for the next position of the first matrix, and so on. With this technique the two matrices, rotating around the (two) source(s), simulate a complete ring of detectors of approximately 20cm in diameter. The data obtained are used to reconstruct the activity (see figure 3.19 for the profiles of the reconstructed activity of the single source and figure 3.20 for the profiles of the two point sources).
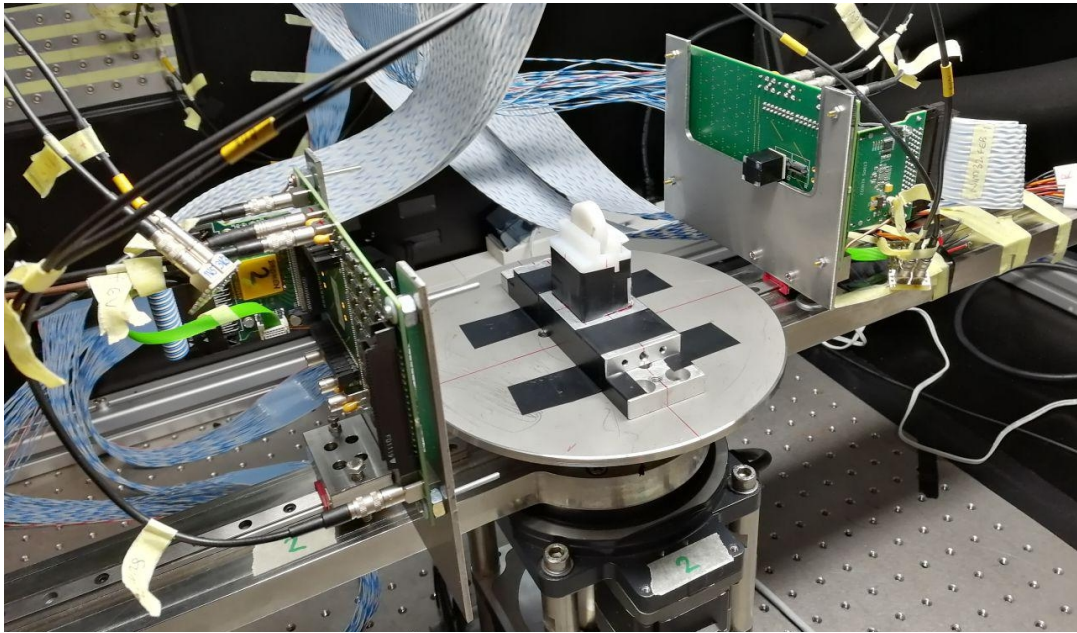
FIGURE 3.18: Scheme of the setup for the single sodium-22 point source reconstruction
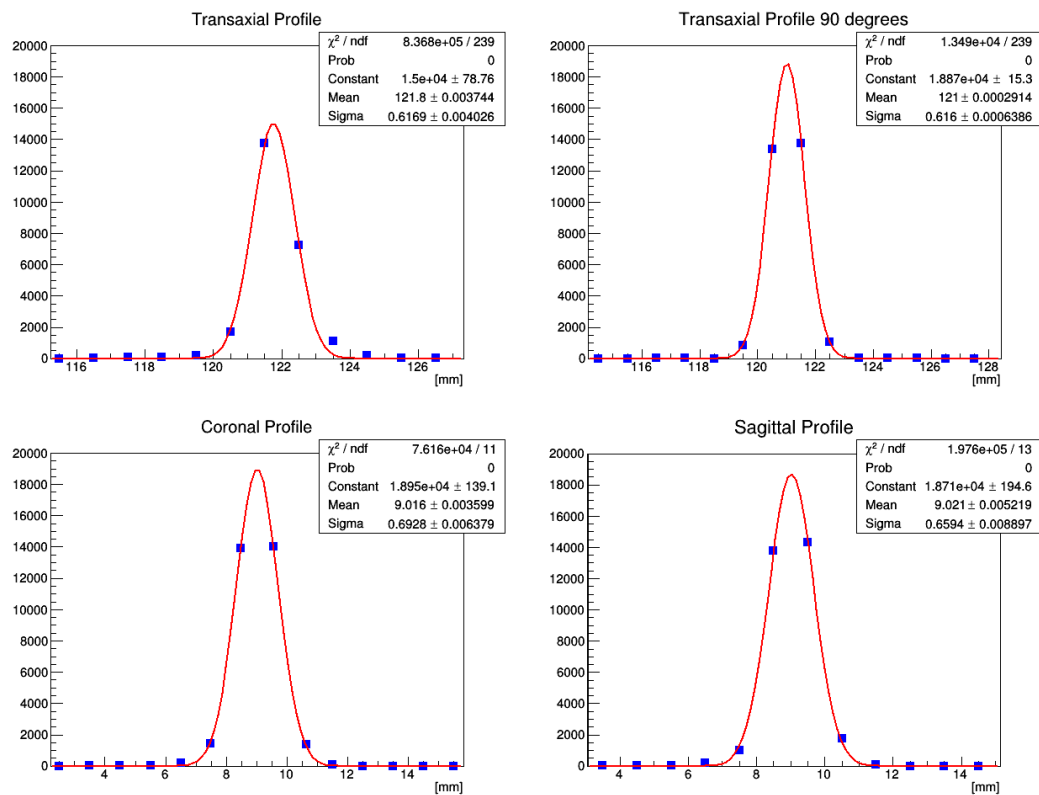
FIGURE 3.19: Profiles of the reconstructed activity fitted with a Gaussian for the single point source
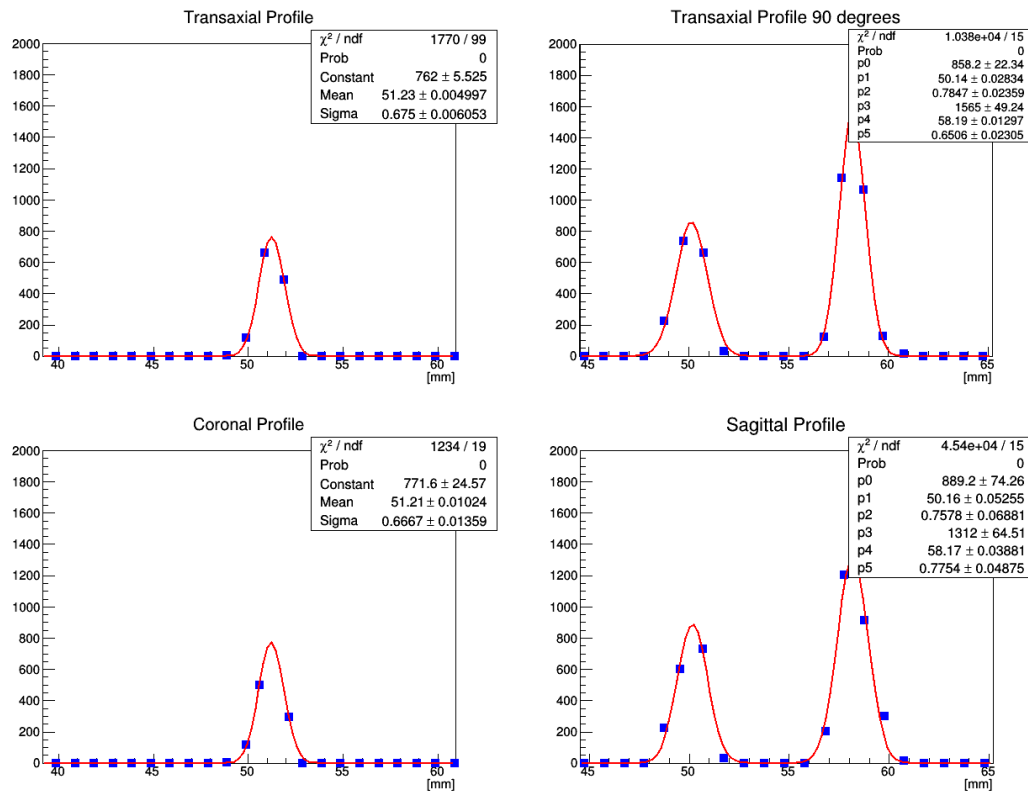
FIGURE 3.20: Profiles of the reconstructed activities fitted with
two Gaussians for the two point sources

The algorithm used for the reconstruction of the image is based on a list mode
Maximum Likelihood Estimation Method (MLEM, Shepp and Vardi, 1982)
software previously developed for the ClearPEM project (Cao et al., 2011).
The original code was modified to include the Time Of Flight information in
the reconstruction kernel. The values for the spatial resolution obtained from
the fit of the reconstructed activities are shown in 3.2.

References

Acerbi, Fabio and Stefan Gundacker (2019). "Understanding and simulating
SiPMs". In: *Nuclear Instruments and Methods in Physics Research Section A:
Accelerators, Spectrometers, Detectors and Associated Equipment* 926, pp. 16–
35.

Bircher, Chad and Yiping Shao (2012). "Use of internal scintillator radioactiv-
ity to calibrate DOI function of a PET detector with a dual-ended-scintillator
readout". In: *Medical physics* 39.2, pp. 777–787.

Direction	Single	Double (left)	Double (right)
Transaxial	(1.45 ± 0.01)mm	(1.59 ± 0.01)mm	
Transaxial 90 deg.	(1.451 ± 0.001)mm	(1.85 ± 0.05)mm	(1.53 ± 0.05)mm
Coronal	(1.63 ± 0.01)mm	(1.57 ± 0.01)mm	
Sagittal	(1.55 ± 0.01)mm	(1.8 ± 0.1)mm	(1.8 ± 0.1)mm

TABLE 3.2: FWHM spatial resolution for different directions of
the reconstructed sources

Cao, Liji et al. (2011). "List-mode maximum-likelihood reconstruction for the ClearPEM system". In: *2011 IEEE Nuclear Science Symposium Conference Record*. IEEE, pp. 4171–4174.

Shepp, Lawrence A and Yehuda Vardi (1982). "Maximum likelihood reconstruction for emission tomography". In: *IEEE transactions on medical imaging* 1.2, pp. 113–122.

Van Dam, Herman T et al. (2010). "A comprehensive model of the response of silicon photomultipliers". In: *IEEE Transactions on Nuclear Science* 57.4, pp. 2254–2266.

Chapter 4

Improving Coincidence Time Resolution using Depth Of Interaction Information

4.1 Introduction

As explained in Chapter One, Depth Of Interaction (DOI) plays an important role both in small animal PET detectors (where it helps to reduce parallax error), as well as in full-body Time Of Flight (TOF) PET scanners (in which is fundamental to reduce the time jitter caused by the interaction of the primary gamma photon at different DOI). In the latter case, an improvement in Coincidence Time Resolution (CTR) is directly correlated to an increase in Signal to Noise Ration (SNR) in the reconstruction process, ultimately leading to better images of the region under study.

In this chapter we will present an innovative method to improve CTR exploiting DOI information obtained with a light sharing and recirculation mechanism. The first section will be dedicated to the characterization of the experimental setup, the following one to the description of the DOI encoding technique and the last one to the CTR correction method itself.

4.2 DOI

In PET detectors, Depth Of Interaction (DOI) is the quantity that measures the position of the interaction of the γ photon along the longitudinal axis of the crystal pixel.

In modern full-body detectors, the Time Of Flight (TOF) information is used to estimate the position of the point of annihilation along the LOR (see figure 4.1a). This additional information is useful to improve the Signal to Noise Ratio (SNR) in the reconstructed image, ultimately leading to a better diagnosis (Brown et al., 2014). A higher Coincidence Time Resolution (CTR) improves the spatial resolution on the annihilation point estimation, according to equation 1.15.

To reduce the contribution to CTR caused by the different possible points of interaction of the gamma photons inside the detector, it is possible to use DOI information. Correcting the measured time of detection of the optical photons with their propagation time inside the detector, would lead to a more precise measure of the real time of interaction of the gamma photon and therefore to a better CTR ((Toussaint et al., 2019)).

In PET scanners dedicated to small animals, on the other hand, DOI information could be included to reduce the parallax error caused by the position of the interaction of the gamma photons (see figure 4.1b) (Green et al., 2010). This is particularly severe for gamma couples generated in the external regions of the Field Of View (FOV) (Yao, Lecomte, and Crawford, 2012). Given the abundance of such events in pre-clinical scanners, where the body of the animal almost fills the FOV, and the high ratio between the size of the crystal and the scanner size, this problem particularly affects this category of machines.

4.2.1 The light recirculation technique

There are many different techniques and technologies available to obtain DOI information (Ito, Hong, and Lee, 2011, Orita et al., 2005, Yang et al., 2006, Van Dam et al., 2011, Yang, Wu, and Cherry, 2009, Shao et al., 2014,). In this section, a method developed at CERN (Pizzichemi et al., 2016) is tested using the setup described in section 3.2.

This method is based on the sharing and recirculation of the scintillation light: the optical photons produced in each crystal pixel of the detector are recirculated through the backside of the array and shared among the other crystals, eventually reaching different channels of the photodetector. A scheme of the detector is shown in figure 4.2.

Fundamental for the circulation of the light across all pixels are the light guide and the layer of reflective material coupled to it. With these elements,
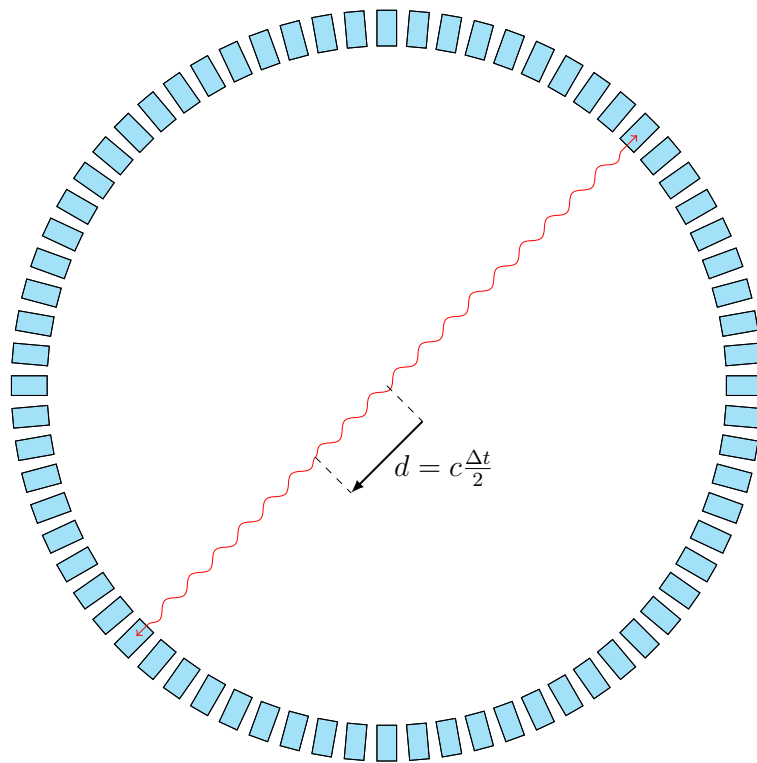
(A) Benefit of knowledge of TOF in a Whole Body PET scanner
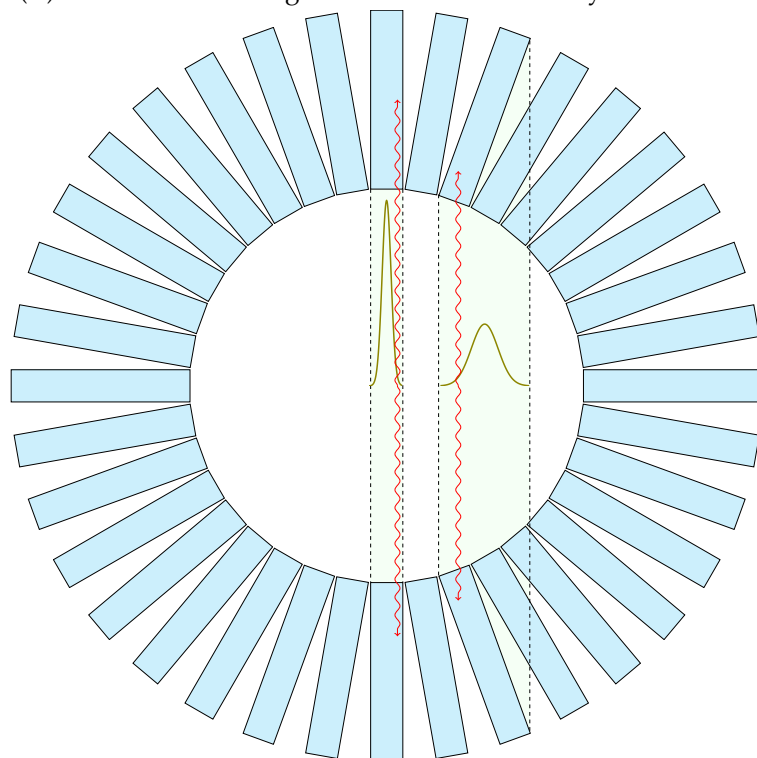
(B) Importance of TOF in a small animals or organs dedicated PET scanner

FIGURE 4.1: Role of TOF in two different types of PET scanners
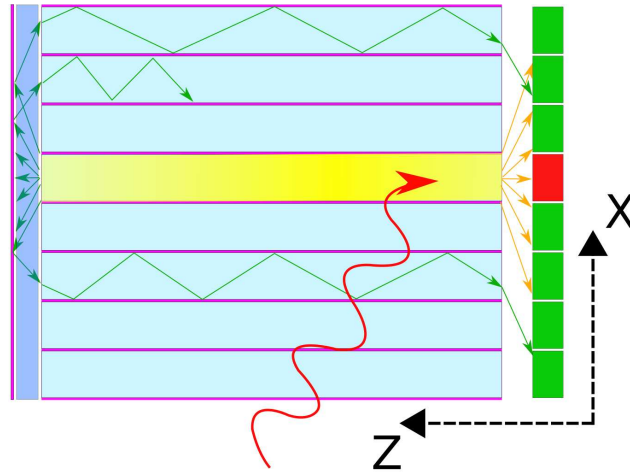
FIGURE 4.2: Working principle of the light recirculation technique

photons that escape from the back of the crystal pixel that was hit by the gamma photon are redirected in other crystals, that would not produce any scintillation photons otherwise and work as a light guide in this case.

In order to correlate the asymmetry of the light emitted directly towards the photodetector and the light shared among the other crystals to the DOI, it is necessary to lightly depolish the lateral surfaces of the crystal pixels (Vilardi et al., 2006, Trummer, Auffray, and Lecoq, 2009). In fact, in a perfectly polished crystal, half of the scintillation light would be emitted from the front side and half from the back. However, due to the depolishing treatment and the resulting Lambertian scatter at the surfaces, it is more likely for the photons to exit from the front face of the crystal when the gamma interaction happens close to this area than from the back, and vice versa.

The DOI information is therefore obtained from the ratio between the light seen by the channel coupled to the crystal that was hit by the gamma photon, and the total light seen by the photodetector array, obtained as the sum across all channels. This method, compared to other solutions, has the advantage of requiring a small modification of the detector module while not requiring a second light readout.

4.2.2   Notation

Each interaction point of a gamma photon inside the detector can be denoted by a set of 3 space coordinates, (x, y, z). x and y are the 2 coordinates in the

plane perpendicular to the main axis of the crystal pixels, and z the one along the latter.

Denoting with X_i and Y_i the coordinates of the centre of the SiPM channels, with p_i the light collected by the trigger SiPM and with P_{tot} the total light seen by the photodetector array, a set of three estimators (u, v, w) is defined for the three space coordinates (x, y, z):

$$u = \frac{\sum_1^N p_i X_i}{P_{tot}} \tag{4.1}$$

$$v = \frac{\sum_1^N p_i Y_i}{P_{tot}} \tag{4.2}$$

$$w = \frac{p_i}{P_{tot}} \tag{4.3}$$

u, v and w coordinates are used in the clustering algorithm (presented in the following section, 4.2.3) to determine the crystal of energy deposition for each event. To each event the coordinates of the center of the corresponding crystal are then assigned as the x and y coordinates. However, in order to correlate w and z a calibration is required to determine the nature of the function that link the two quantities:

$$z = f(w) \tag{4.4}$$

This calibration will be presented in section 4.2.4.

4.2.3 The clustering algorithm

The (u, v, w) coordinates of each event are plotted in a 3D histogram (shown in figure 4.3): the events corresponding to full energy deposition in a single crystal are clustered in 16 or 64 regions, depending on whether the matrix under study is made of 16 or 64 crystals. The events where the energy is deposited in more than one crystal, are found between them in a diffuse cloud.

The clustering algorithm operates iteratively over the spatial voxels containing the events. Starting from the voxel V_0 with the highest number of events, the algorithm moves to the surrounding voxels and discards all those with a number of entries below a threshold defined as a fraction of the events in
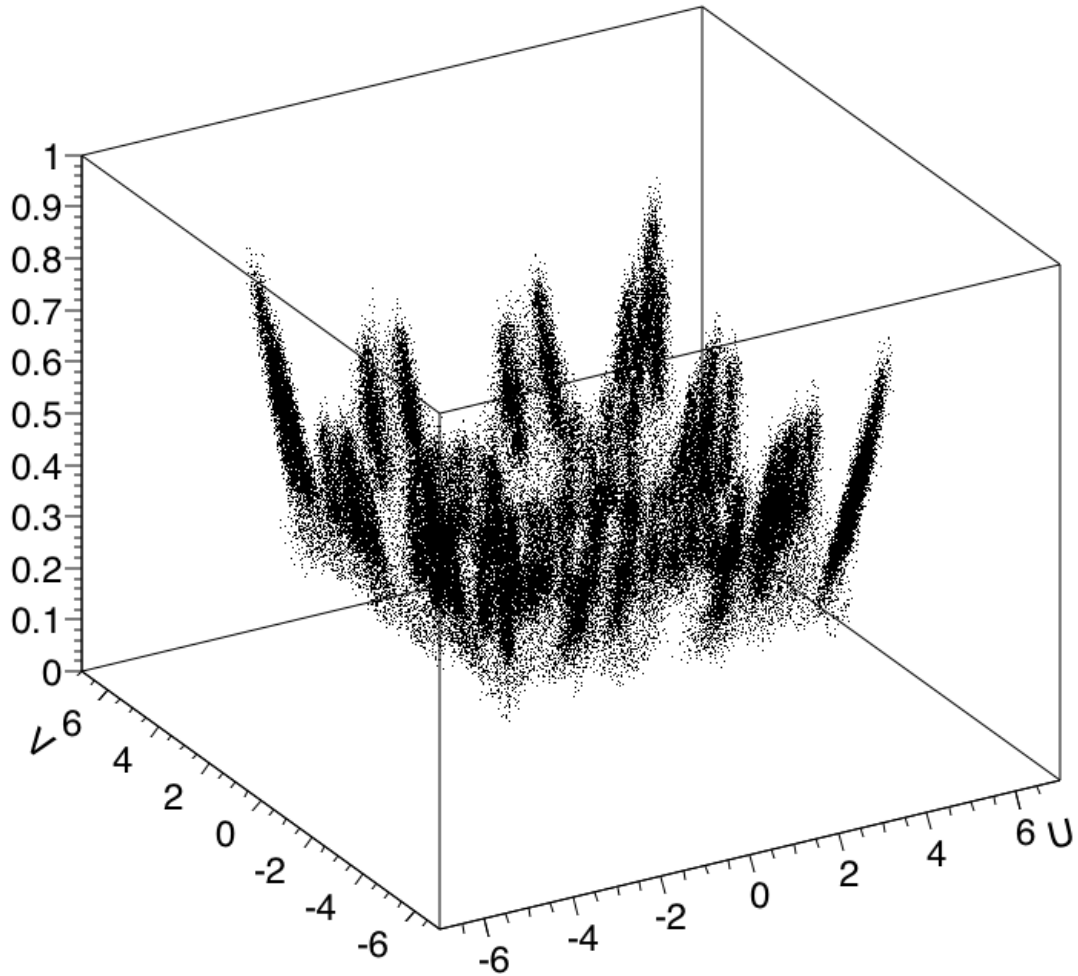
FIGURE 4.3: 3D representation of all the events recorded inside
the matrix, without any cut

V_0; the remaining voxels are added to the list of seeds. The algorithm starts again from one of these voxel seeds and the procedure is repeated until no seeds are left. At this point, the collection of all seeds found defines a cluster, which is removed from the original 3D plot and the procedure starts again, until 64 regions are found.

The 4 distributions corresponding to a single MPPC before the algorithm is applied are shown in 4.4a and after in figure 4.4b.

4.2.4   DOI measurements

To determine the function in equation 4.4, and therefore validate the method, it is necessary to know *a priori z* and to measure *w*.

For this purpose, a set-up with an external Tagging Crystal (shown in figure 4.5, with a scheme shown in figure 4.6) was used. The matrix is irradiated
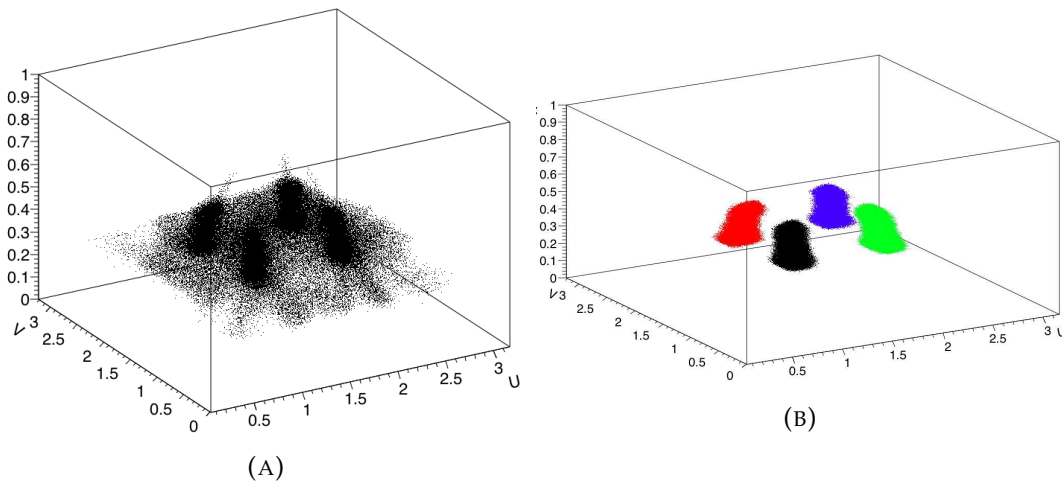
FIGURE 4.4: 3D plot of all the events associated to a single MPPC, before and after the clustering algorithm was applied

from the side with a sodium-22 source; the tagging crystal, kept perpendicular to the matrix, allows focusing the irradiation spot. The position of the matrix, with respect to the axis defined by the source and the external crystal, allows the choice of the DOI of the irradiation spot.

In figure 4.7 is shown the distribution of the w coordinate of each event, with each color representing events relative to different source positions. The distributions are Gaussians and their mean value shift along the w axis as the beam spot moves along the matrix longitudinal axis (with $z0$ corresponding to the SiPM side of the matrix).

The DOI of the irradiation spot of each acquisition is shown in figure 4.8 against the mean of the gaussian of each w distribution. As demonstrated by the fit, the two variables are linearly correlated. The parameters of the fit function are used for the calibration of the method:

$$z = m \cdot w + q \tag{4.5}$$

defining the form of the function in equation 4.4.

This equation is then used to compute the DOI resolution: for each event the dispersion between the z coordinate obtained through the formula 4.5 and the "true" z given by the position of the beam spot is computed, and the resulting distribution is fitted with a Gaussian function. This procedure is repeated for all positions and all crystals, averaging on all these values.
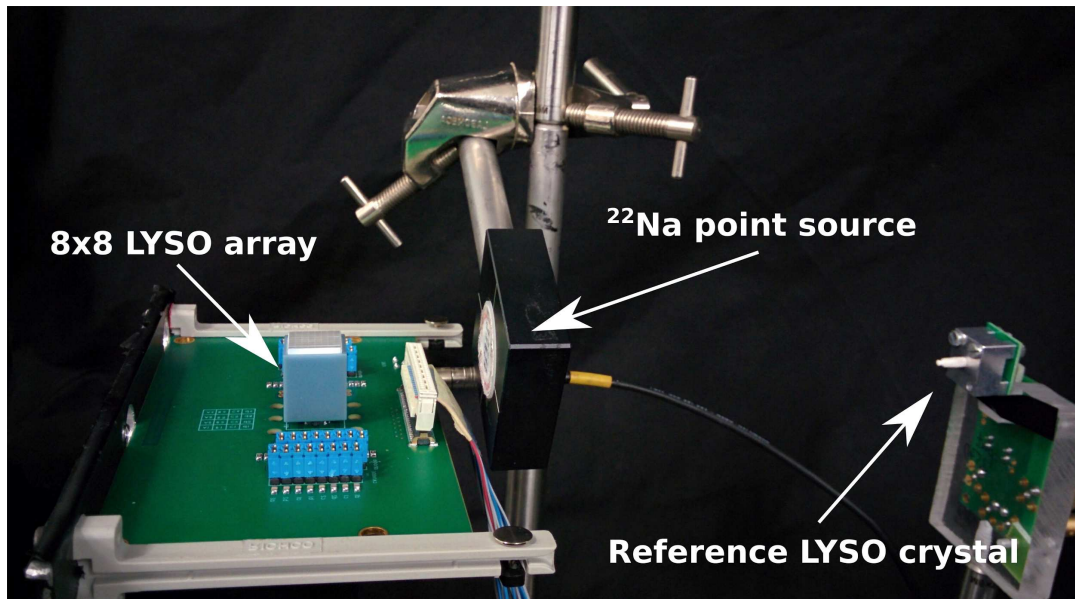
FIGURE 4.5: Picture of the experimental setup used for lateral irradiation of the detector
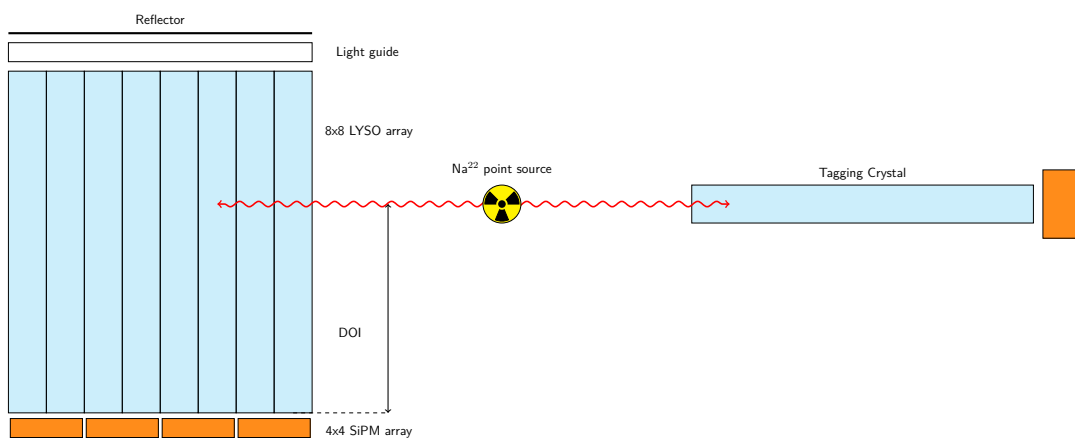
FIGURE 4.6: Scheme of the experimental setup used for lateral irradiation of the detector
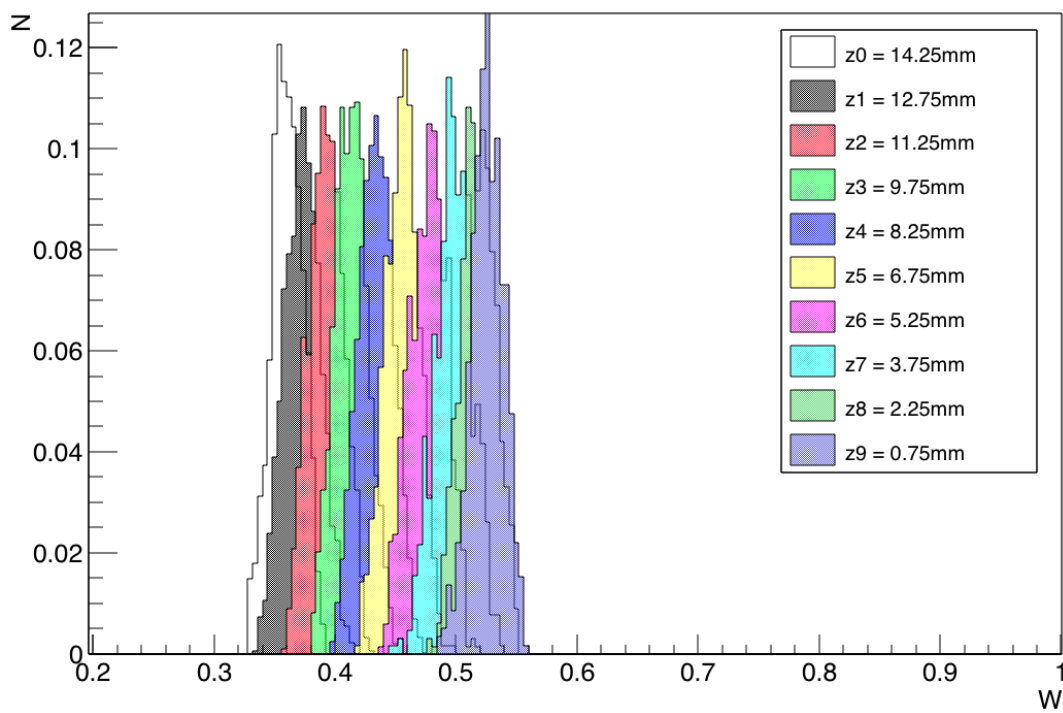
FIGURE 4.7: Distribution of w coordinate, for different values of DOI
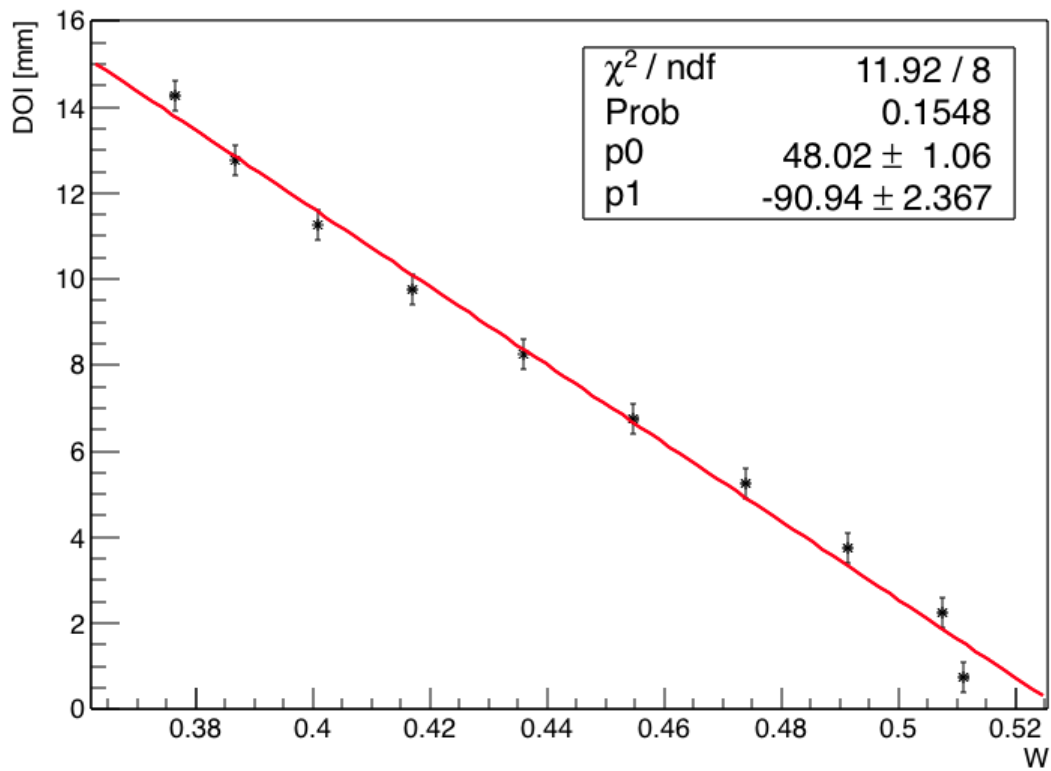
FIGURE 4.8: Fit of the DOI values as a function of the mean values of the distributions shown in 4.7

Array type	Length (mm)	DOI resolution FWHM (mm)
4 ×4	15	3.3 ±0.1
8 ×8	15	3.2 ±0.1
8 ×8	30	3.4 ±0.1
12 ×12	15	4.2 ±0.2

TABLE 4.1: Overview of the DOI resolution obtained with different depolished arrays.

The measurements are carried out on 4×4, 8×8 (both 15 mm and 30 mm long) and 12×12 matrices . The results are summarised in the table 4.1.

4.2.5 An alternative calibration method

The calibration method described in the section 4.2.4 cannot be applied in the case of a module assembled in a full ring of detectors: in addition to being time-consuming, it would require disassembling the detector in order to irradiate each module from the side.

For this reason a different calibration method was developed (Stringhini et al., 2016). It consists in an irradiation in a PET-like configuration to obtain the equation 4.5 and it is based on the use of the normalized w distribution as a pdf, taking into account the exponential attenuation of the gamma ray inside the matrix:

$$z = D + \lambda \ln \left[1 - (1 - \exp^{-D/\lambda}) \int_0^w PDF(w)dw \right] \qquad (4.6)$$

where λ is the attenuation length of the LYSO (Shao, Yao, and Ma, 2008). The setup used for this calibration is shown in figure 4.9.

This method was compared with the data from the previous system and was found in good agreement with it ($\pm$ 1mm), allowing to achieve the same DOI resolution (see figure 4.10 for the comparison between the data from the lateral scan and the function 4.6 and figure 4.11 for the dispersion between the two methods).

(A)

(B) test
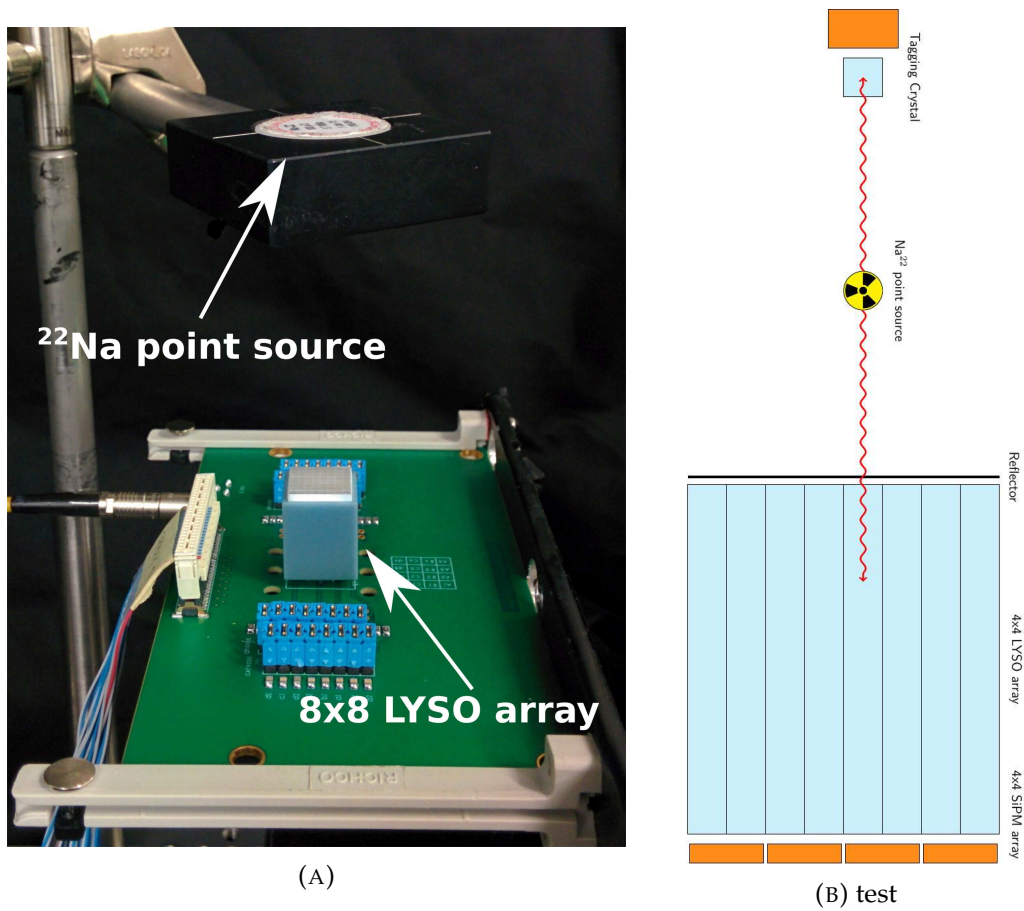
FIGURE 4.9: Image and scheme of the experimental set-up used
for the alternative calibration method
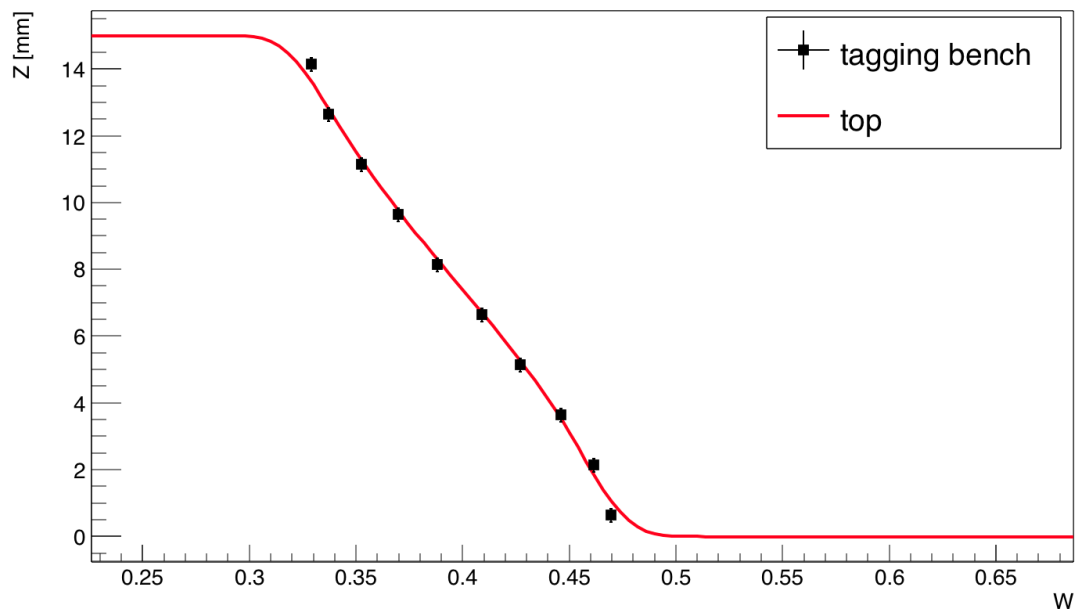
FIGURE 4.10: Superposition of the calibration function with the
experimental data obtained with the external tagging crystal
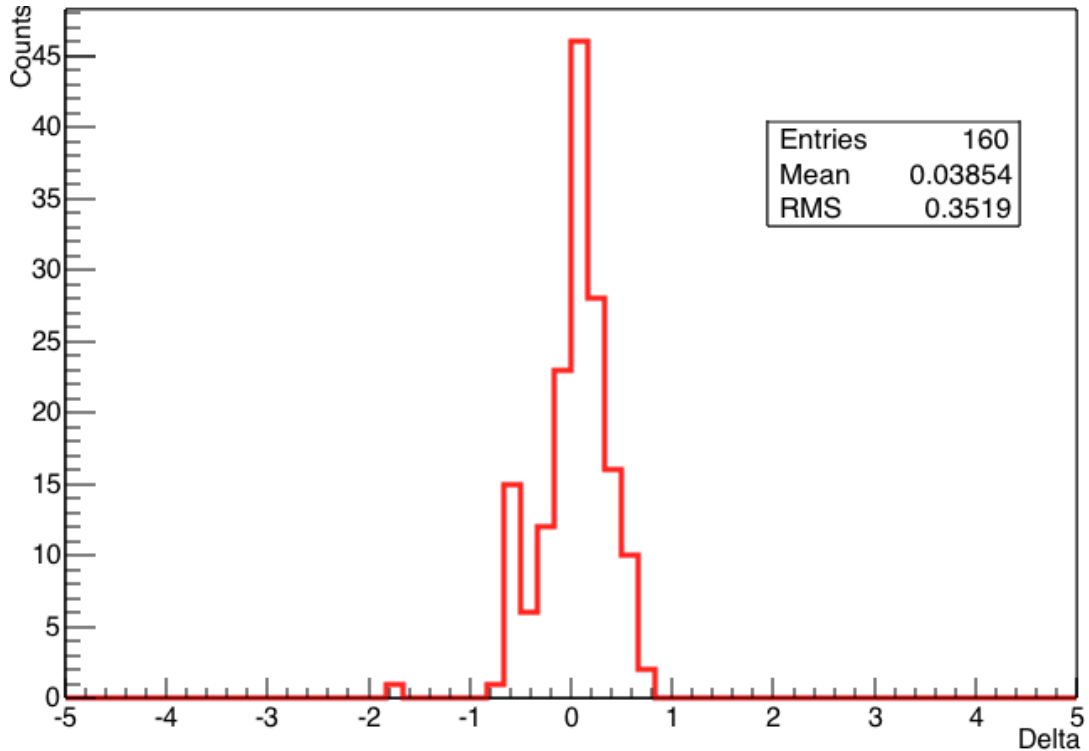
FIGURE 4.11: Dispersion between DOI values obtained with
the calibration function and with the external crystal

4.2.6 DOI with BGO

Similar to the procedure applied to LYSO matrices, DOI can be obtained with the same configuration but using different scintillators. In particular, the possibility to use a BGO matrix and measure DOI was investigated.

The matrix is made of 16 $3.1 \times 3.1 \times 15\text{mm}^3$ BGO pixels, with depolished lateral surfaces, produced by Epic Crystal. Photodetector, reflector and couplings are the same as in the LYSO module: Hamamatsu S13361-3050-AE-04, ESR and OCA respectively. .

Similar to the procedure adopted with LYSO, the BGO matrix was irradiated from the side with a narrow beam, in order to know the DOI of each event *a priori*. In figure 4.12 is shown the average of the w histogram for each position of the external reference, versus the DOI of the irradiation spot. As with LYSO, there is a linear correlation between these two quantities, suggesting the ability to extract DOI information.

However, the histogram for w for a DOI of 7 mm, as an example, is shown in figure 4.13. From this plot is clear that the dispersion of the w coordinate around its average value is comparable to the range of values of the averages
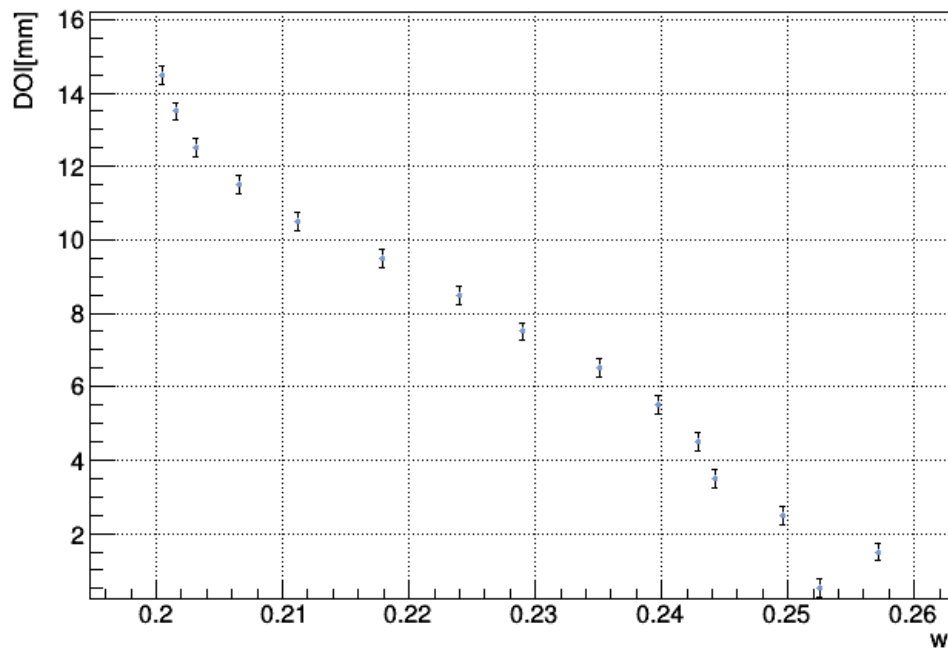
FIGURE 4.12: DOI position of the external source/reference crystal setup versus the mean values of the distributions of w quantity

of w for each position itself. This has an impact on the DOI spatial resolution, which is on average 8mm FWHM across the length of the matrix.

4.3 The time correction

The depolishing treatment applied to the lateral surfaces of each crystal pixel, necessary for the DOI method explained in section 4.2.1 degrades time resolution (Bircher and Shao, 2012). Where for small animal detectors applications this may not be a limiting factor, it is a problem in whole-body PET machines, in which the main advantage of having access to DOI information would be to improve CTR and therefore the Signal to Noise Ratio.

Moreover, the difference in terms of index of refraction of the crystal seen by gamma and optical photons causes jitter in the time of arrival of the first optical photons at the photodetector depending on the point of interaction of the gamma photon. In particular, for a hypothetical emission of two gamma photons at the same time, the optical photon produced by the gamma that interacts closer to the photodetector will reach the photodetector earlier than the optical photons produced the gamma interacting far away from it (see
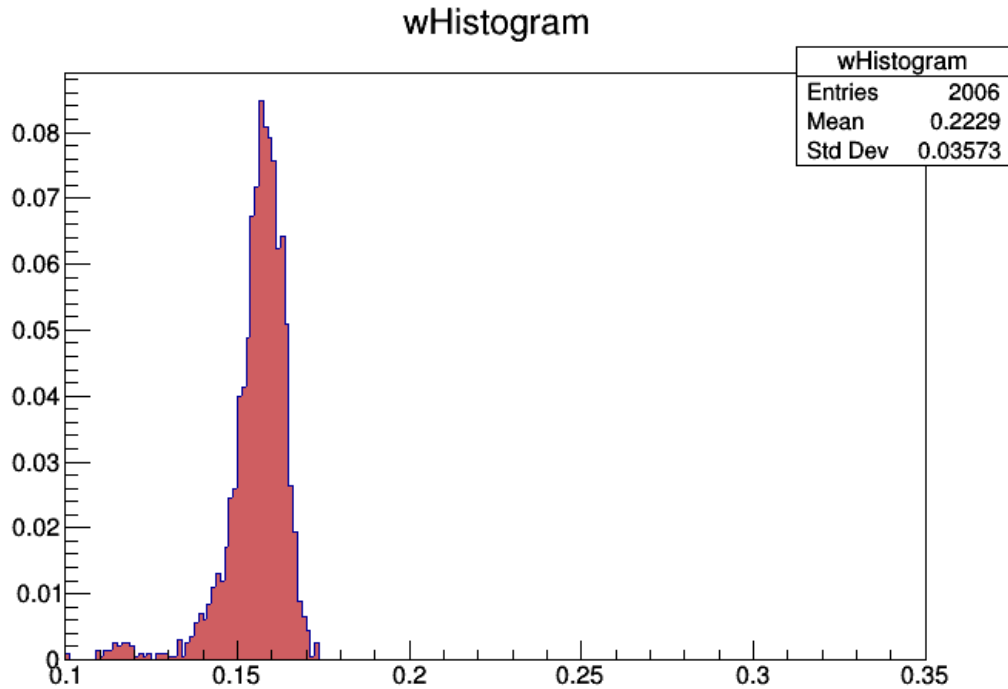
FIGURE 4.13: Distribution of the w coordinate for events at DOI 7mm

figure 4.14). This effect is present also in detectors with polished lateral surfaces.

4.3.1 How the correction works

DOI information could help to reduce the spread in the time of arrival of the optical photons. For any event, these photons are emitted from the crystal in which the interaction of the gamma photon took place in both directions: some towards the photodetector channel directly coupled to the crystal, some in the opposite direction; thanks to light recirculation, these are collected by the neighboring channels.

The time necessary for the optical photons to travel across the crystal pixels is a function of the DOI. In the case of depolished lateral faces, at each interaction of the photon with the surface, the Lambertian nature of the scatter causes it to bounce in a random direction. Therefore, the distribution of the light collected across all channels depends on DOI itself, as explained in more detail in section 4.2.1.

For these reasons, it should be possible to use the DOI information (accessible thanks to the light sharing configuration) to correct the timestamps produced
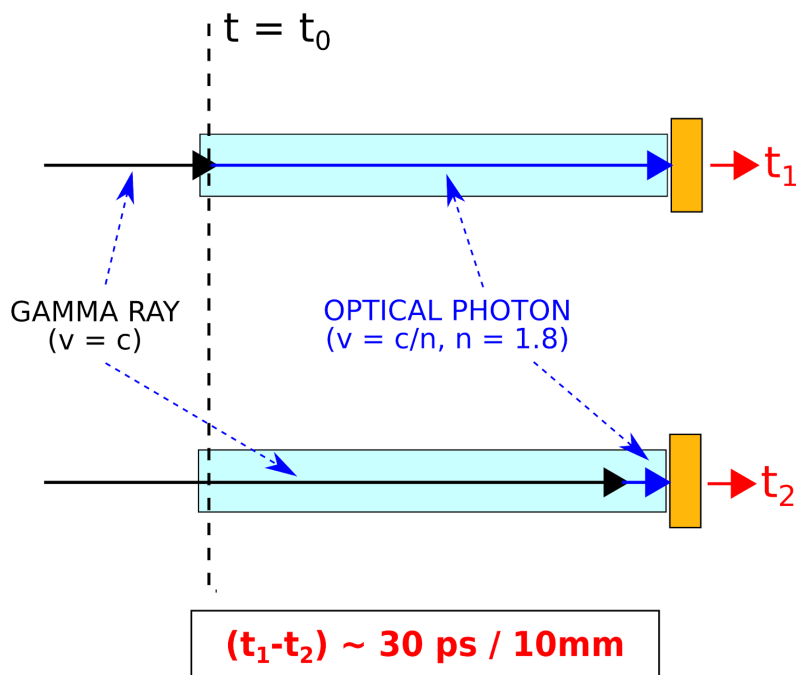
FIGURE 4.14: Difference in DOI and propagation time of gamma and optical photons in the crystal bulk cause a time jitter

by each event, knowing from a calibration run how long it should take, on average, for a photon to reach any of the photodetector channels.

4.3.2 Notation

Referring to the module described in section 3.1.1, the most simple estimator of the time of interaction of the gamma photon t_{int} in the matrix is given by the time of detection t_1 for the channel D_1 coupled to the crystal C_1 hit by the gamma photon, where

- t is one of the timestamps ($\{t\}$) provided by the 16 photodetector channels $\{D\}$;

- D is one of the 16 channels ($\{D\}$) of the photodetector;

- C is one of the 16 (or 64) crystals of the matrix ($\{C\}$).

The index 1, in particular, is used for the crystal C where the interaction occurred.

Because of light sharing, also any of the surrounding channels D_i will detect a portion of the scintillation light emitted by the crystal C_1. As depicted in

(A) DOI=0   (B) DOI=h
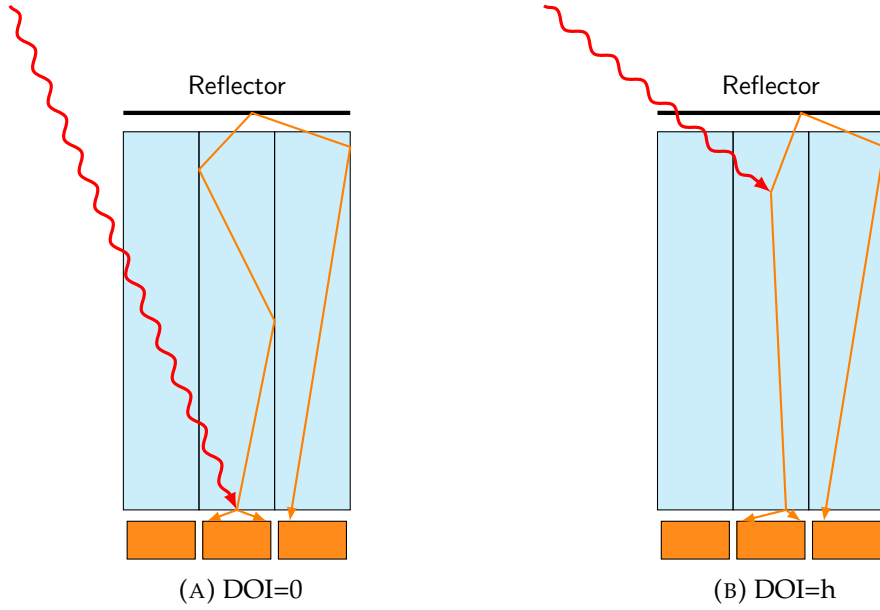
FIGURE 4.15: Optical photons travel inside the matrix through different routes, according to the DOI

figure 4.15, all these timestamps t_i will have a certain delay with respect to t_1. The fundamental hypothesis here is that this delay is dependent on the DOI of the interacting gamma photon, as the optical photons have to travel different lengths depending on where they were produced. For this reason, we assume there is a relation

$$g_i(w) = [t_i - t_1](w) \tag{4.7}$$

between the average delay of the photodetector D_i with respect to D_1 and the DOI coordinate w. In the limit case of D_1, the relation reduces to the trivial expression $g_1(w) \equiv 0$.

Once the relations $g_i(w)$ are known, for any event it is possible to have K independent estimation of t_1, where K is the number of photodetectors:

$$t_1^{(i)} = t_i - g_i(w) \tag{4.8}$$

where each $t_1^{(i)}$ is obtained as difference between the ith timestamp t_i and the expected delay from D_1 computed at the specific w of the event.

The set of timestamps $t_1^{(i)}$ can then be combined to give the best possible estimator of t_1, written as

$$\hat{t}_1 = \frac{\sum_{i=1}^{K}(1/\sigma_i^2) \cdot t_1^{(i)}}{\sum_{i=1}^{K}(1/\sigma_i^2)} \tag{4.9}$$

The weights σ_i are the widths of the histograms of the $t_1^{(i)}$ measurements, evaluated at the w of the event.

Finally, the quantity $\hat{t}_1$ itself, if measured from the emission of the gamma, can be supposed to depend on DOI as well. Therefore to find the real time of interaction $\hat{\theta}_{int}$, it is necessary to subtract from $\hat{t}_1$ the expected delay due to DOI, to give

$$\hat{\theta}_{int} = \hat{t}_1 - [d(w_0) - d(w)] \tag{4.10}$$

where $d(w)$ is the average delay expected between t_1 and an external reference, at the w of the event, and $d(w_0)$ the average delay at a fixed DOI used at reference.

4.3.3 Calibration measurements

To obtain the delays $g_i(w)$ and $d(w)$ and the weights σ_i the same setup described in section 4.2.5 was used. In this case, along with the charges q_i, also the time stamps t_i produced by each channel were recorded, using as reference for each event the t_{ref} provided by the reference crystal.

The first step is to plot, for each channel of the photodetector, the time difference $t_i - t_1$ for each event as a function of the coordinate w; as an example, one of these plots is shown in figure 4.16. It is clearly visible that for high DOI (high w) the time difference is higher because the optical photons produced in crystal C_1 have to travel greater length in order to reach the photodetector channel D_i. From these plots, both the average delays $g_i(w)$ and the weights σ_i are obtained.

The second step instead is to plot the time difference $t_1 - t_{ref}$ for each event, again as a function of the coordinate w; the result is shown in figure 4.17. In this case, the correlation is in the opposite direction compared to figure 4.16: the closer is the point of interaction of the gamma photon in crystal C_1 to the photodetector channel D_1, the less it takes for the optical photons to reach D_1. From this plot the average delays $d(w)$ are obtained.
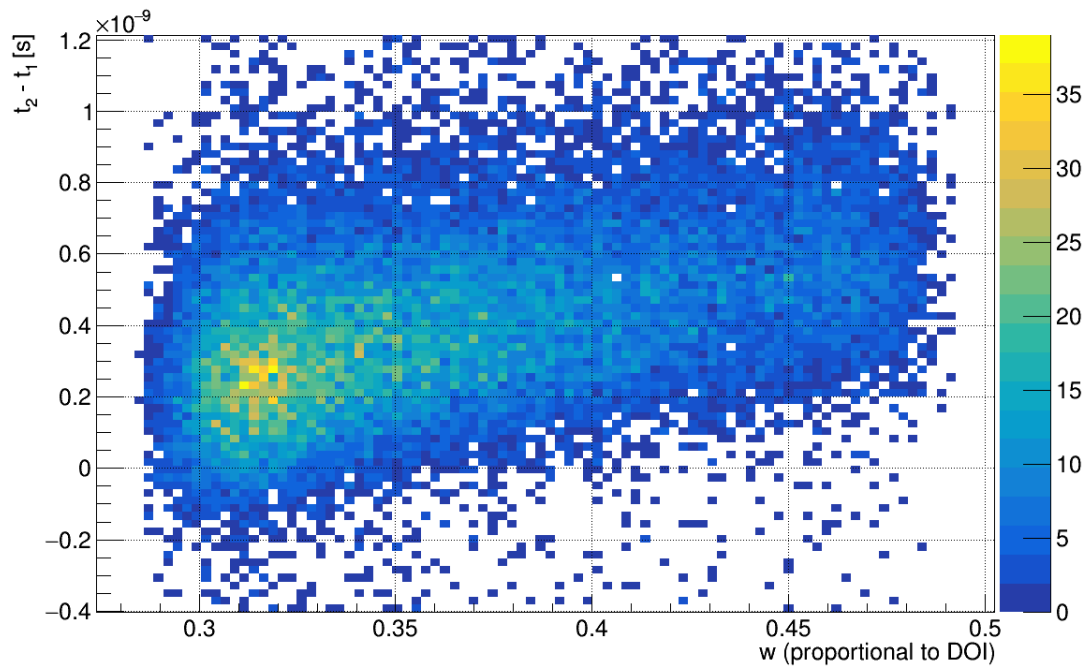
FIGURE 4.16: Scatter plot of the time difference $t_i - t_1$ for each event as a function of the coordinate w
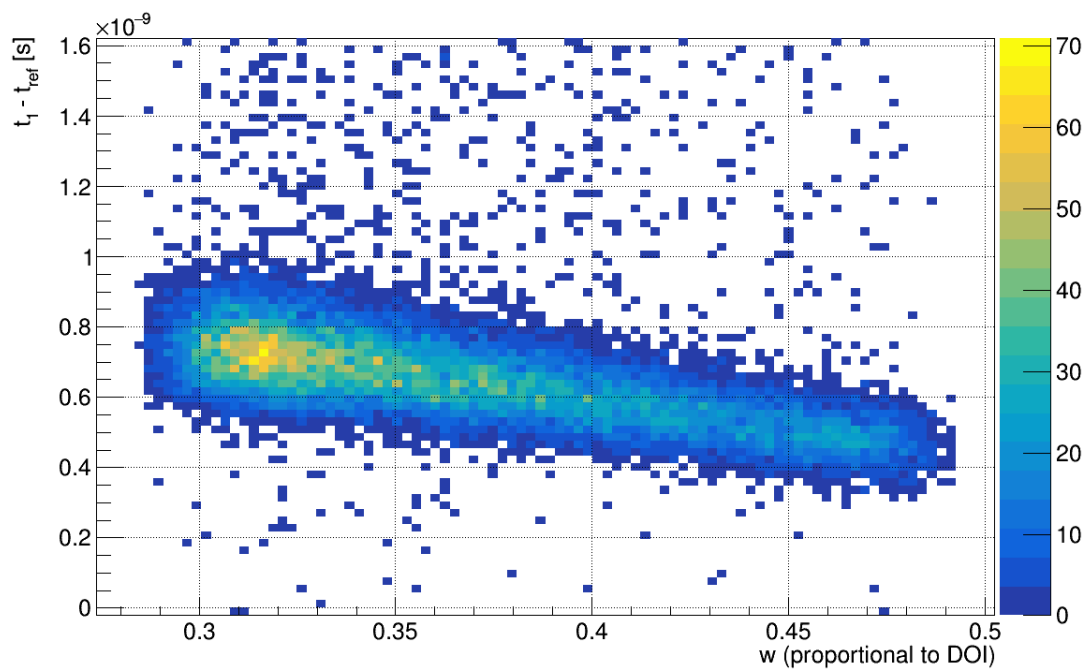
FIGURE 4.17: Scatter plot of the time difference $t_1 - t_{ref}$ for each event as a function of the coordinate w
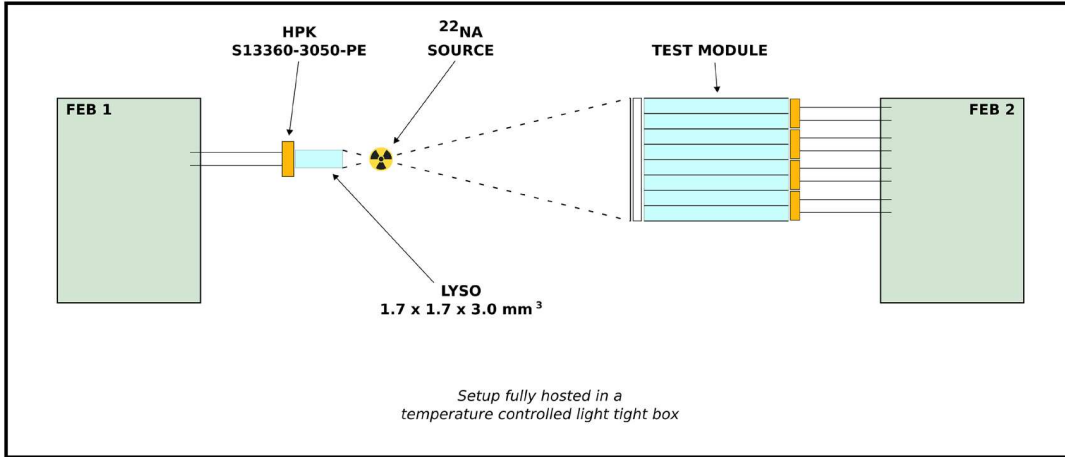
FIGURE 4.18: Scheme of the setup used for CTR measurements.

4.3.4 CTR measurements

In order to test the method, the matrix is irradiated with a wide beam in a PET-like configuration (see figure 4.18). This way, it is possible to have events at different DOI in each crystal, similar to what would happen in a PET scanner.

For every event, the difference between the timestamp of the reference crystal and the timestamp provided by the channel coupled to the crystal hit by the gamma photon is computed as:

$$\Delta t_{std} = t_1 - t_{ref} \tag{4.11}$$

and is used to fill a first histogram, H_{std}. A second histogram H_{corr} is later filled applying the DOI correction explained in section 4.3.2:

$$\Delta t_{corr} = \hat{\theta}_{int} - t_{ref} \tag{4.12}$$

The width of these histograms is correlated to the CTR of the system. In order to estimate it, they were fitted with an exponentially modified Gaussian distribution

$$G_e(t; \mu, \sigma, \lambda) = \frac{\lambda}{2} \cdot \exp \frac{\lambda}{2} (2\mu + \lambda\sigma^2 - 2t) \cdot E \left(\frac{\mu\lambda\sigma^2 - t}{\sqrt{2}\sigma} \right) \tag{4.13}$$

where μ and σ are the mean value and the standard deviation of the Gaussian
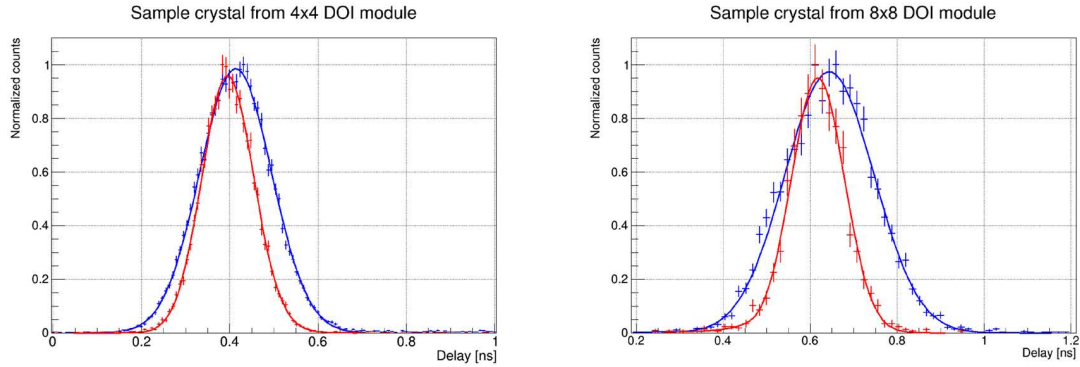
FIGURE 4.19: CTR histograms, before (blue) and after (red) DOI correction, for a 4x4 (left) and 8x8 (right) DOI module.

component, λ is the parameter of the exponential part and E is the complementary error function. The fit function is used to compute the FWHM of the histogram, from which the CTR of the reference crystal is subtracted (using $CTR_{matrixVSreference} = \sqrt{(CTR_{matrix})^2 + (CTR_{reference})^2}$) and the result multiplied by $\sqrt{2}$, in order to obtain the CTR of two modules identical to the one under study.

As a reference, an array with polished lateral surfaces and no light guide was irradiated as well, in order to obtain a comparison value for the best possible CTR in the standard module without light sharing and depolishing.

4.3.5 Results

The procedure described in the previous section was repeated for crystals of different sizes. In particular both 1:1 and 4:1 coupling between crystal pixels and SiPM were investigated. The histograms of the CTR values before and after the DOI corrections are shown in figure 4.19. For both configurations, the obtained CTR was compared to the CTR obtained with an identical matrix with polished lateral surfaces. All the CTR values obtained are shown in table 4.2.

Furthermore, for both couplings, a smaller subset of channels was considered: given the fact that in a complete ring of detector the vast majority of the crystals are surrounded by other crystals, to have a better idea of the performance of the correction in this configuration we considered events where energy deposition happen inside crystals coupled to the 4 central channels of the photodetector. This is referred to as *all* and *central* in table 4.2.

array type	crystals	$CTR_{depo}[ps]$	$CTR_{depo,corr}[ps]$	$CTR_{poli}[ps]$
8 ×8	all	307 ±3	166 ±2	158 ±2
8 ×8	central	308 ±3	157 ±2	154 ±2
4 ×4	all	233 ±2	165 ±2	162 ±2
4 ×4	central	234 ±2	159 ±2	158 ±2

TABLE 4.2: Overview of the CTR obtained with different depolished arrays, before and after DOI correction, compared with the reference polished one.

In all cases, the external reference contribution to CTR is subtracted from the value obtained and the result is multiplied by $\sqrt{2}$: this way, it is possible to have an estimation of what the CTR would be having to identical modules in coincidence.

4.3.6 Discussion

Results shown in table 4.2 demonstrate that correcting for the DOI of the gamma photon effectively improves the CTR of the modules. In particular, CTR values obtained considering only the crystals couples to the central channels of the photodetector are slightly better than those obtained including all crystals. This is expected because the correction method relies on the information obtained from the neighboring channels: in the case of an external channel, only a few other channels can be taken into account for the estimation of the time of interaction.

Moreover, comparing the results obtained considering only the central channels to the CTR of the reference matrices (polished and without any light sharing), we can see from table 4.2 that they are compatible with them. This means that the degradation in CTR performance, caused by the depolishing treatment necessary to obtain DOI, can be successfully recovered exploiting the DOI information itself.

References

Bircher, Chad and Yiping Shao (2012). "Investigation of crystal surface finish and geometry on single LYSO scintillator detector performance for depth-of-interaction measurement with silicon photomultipliers". In: *Nuclear Instruments and Methods in Physics Research Section A: Accelerators, Spectrometers, Detectors and Associated Equipment* 693.Supplement C, pp. 236 –243. ISSN: 0168-9002. DOI: https://doi.org/10.1016/j.nima.2012.07.029.

Brown, Mark S et al. (2014). "Influence of depth of interaction upon the performance of scintillator detectors". In: *PloS one* 9.5, e98177.

Green, Michael V et al. (2010). "Experimental evaluation of depth-of-interaction correction in a small-animal positron emission tomography scanner". In: *Molecular imaging* 9.6, pp. 7290–2010.

Ito, Mikiko, Seong Jong Hong, and Jae Sung Lee (2011). "Positron emission tomography (PET) detectors with depth-of-interaction (DOI) capability". In: *Biomedical Engineering Letters* 1.2, p. 70.

Orita, Narimichi et al. (2005). "Three-dimensional array of scintillation crystals with proper reflector arrangement for a depth of interaction detector". In: *IEEE transactions on nuclear science* 52.1, pp. 8–14.

Pizzichemi, M. et al. (2016). "A new method for depth of interaction determination in PET detectors". In: *Physics in Medicine & Biology* 61.12, p. 4679. URL: http://stacks.iop.org/0031-9155/61/i=12/a=4679.

Shao, Yiping, Rutao Yao, and Tianyu Ma (2008). "A novel method to calibrate DOI function of a PET detector with a dual-ended-scintillator readout". In: *Medical physics* 35.12, pp. 5829–5840.

Shao, Yiping et al. (2014). "Development of a prototype PET scanner with depth-of-interaction measurement using solid-state photomultiplier arrays and parallel readout electronics". In: *Physics in Medicine & Biology* 59.5, p. 1223.

Stringhini, G. et al. (2016). "Development and evaluation of a practical method to measure the Depth of Interaction function for a single side readout PET detector". In: *Journal of Instrumentation* 11.11, P11014. URL: http://stacks.iop.org/1748-0221/11/i=11/a=P11014.

Toussaint, Maxime et al. (2019). "Analytical model of DOI-induced time bias in ultra-fast scintillation detectors for TOF-PET". In: *Physics in Medicine & Biology* 64.6, p. 065009.

Trummer, J, E Auffray, and P Lecoq (2009). "Depth of interaction resolution of LuAP and LYSO crystals". In: *Nuclear Instruments and Methods in Physics*

Research Section A: Accelerators, Spectrometers, Detectors and Associated Equipment 599.2-3, pp. 264–269.

Van Dam, Herman T et al. (2011). "A practical method for depth of interaction determination in monolithic scintillator PET detectors". In: *Physics in Medicine & Biology* 56.13, p. 4135.

Vilardi, I et al. (2006). "Optimization of the effective light attenuation length of YAP: Ce and LYSO: Ce crystals for a novel geometrical PET concept". In: *Nuclear Instruments and Methods in Physics Research Section A: Accelerators, Spectrometers, Detectors and Associated Equipment* 564.1, pp. 506–514.

Yang, Yongfeng, Yibao Wu, and Simon R Cherry (2009). "Investigation of depth of interaction encoding for a pixelated LSO array with a single multichannel PMT". In: *IEEE transactions on nuclear science* 56.5, pp. 2594–2599.

Yang, Yongfeng et al. (2006). "Depth of interaction resolution measurements for a high resolution PET detector using position sensitive avalanche photodiodes". In: *Physics in Medicine & Biology* 51.9, p. 2131.

Yao, Rutao, Roger Lecomte, and Elpida S Crawford (2012). "Small-animal PET: what is it, and why do we need it?" In: *Journal of nuclear medicine technology* 40.3, pp. 157–165.

Chapter 5

ICS: method description and simulations

5.1 Introduction

In commercial PET scanners, events where a gamma deposits its energy in two or more crystals (Inter-Crystal Scatter (ICS) events, figure 5.1) lead to the deterioration of the spatial resolution because of the misposition of the crystal of first interaction. Depending on the crystals' size, material and geometry, these events can contribute up to over half of the total coincidence events (Zeraatkar et al., 2011).

This problem is particularly severe in those systems that are based on pixellated detectors with shared light readout; these scanners are often the preclinical ones, with small detector pixels and high spatial resolution. The ability to correctly assign each scintillation event to the crystal of first interaction would allow achieving the best possible spatial resolution without giving up on sensitivity, a key parameter in PET scanners.

In general, three different approaches to ICS events treatment are found in literature:

- coincidence events where more than two crystals are involved can be discarded,

- a specific algorithm can be applied to them to determine the crystal of first interaction,

- they can be included in the reconstruction process as different possible LOR.
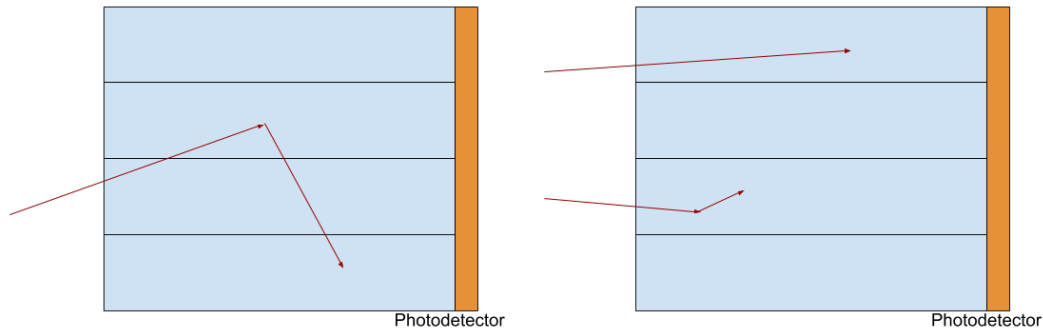
FIGURE 5.1: Left: an ICS event, where the primary gamma energy is deposited in two different crystals
Right: two events in which all the primary gamma energy is deposited in one single crystal

While the first approach completely avoids dealing with the problem (at the cost of a sensitivity loss, even if they are correctly identified), there are different options in terms of the type of algorithm to apply to ICS events (Comanor, Virador, and Moses, 1996, Shao et al., 1996 and Clerk-Lamalice et al., 2012) and also to the reconstruction methods to include multiple LORs for a single event (Gillam et al., 2014). A brief overview of these methods will be given in the next section.

A more drastic approach to the subject, consists of detector designs specifically dedicated to resolving ICS events. This is the case, for example, of Peng, Judenhofer, and Cherry, 2019: a 4 layer crystal detector whose scintillation light is read from all 4 lateral sides. Despite the high performance, these solutions require higher costs and results in lower sensitivity, limiting their application in the commercial market.

In this chapter we present a new method, based on the pixelated detector with light sharing described in the previous chapter, to resolve ICS events that would allow to correctly determine the true Line Of Response (LOR). The method is also preliminary evaluated by means of Monte Carlo simulation in this chapter, while the experimental results are presented in the next one.

5.1.1 Common methods overview

As briefly mentioned before, one of the possible approaches to ICS events is to use an algorithm to try to determine the crystal of first interaction. The most common one found in literature are:
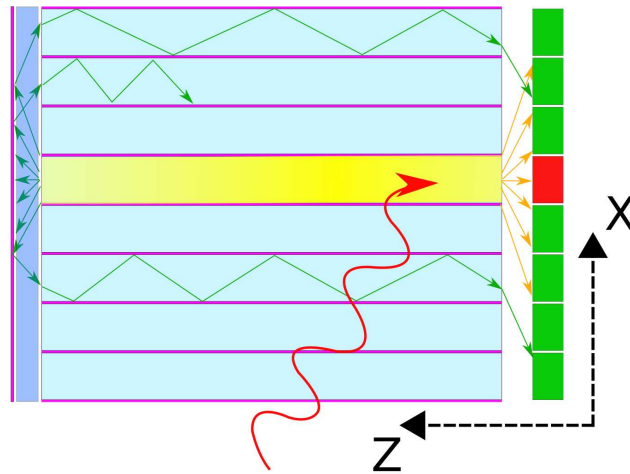
FIGURE 5.2: Working principle of the light recirculation technique

- *maximum energy*: the crystal of first interaction is selected as the one with the highest energy;

- *weighted energy*: the crystal of first interaction is chosen as the crystal containing the centroid of the weighted average of the two energy depositions;

- *minimum energy*: the crystal of first interaction is selected as the one with the second highest energy;

- *random*: the crystal of first interaction is chosen randomly;

- *shortest LOR*: the event associated with the shortest LOR is kept as true LOR for the event;

- *closest to center*: the event associated with the crystal closest to the center $(0, 0, 0)$ of the scanner is chosen as first step of the interaction.

5.2 A new ICS algorithm

The method was developed for a DOI-capable light sharing module. In our case, we used to detector described in chapter 4. Briefly, it is made of a matrix of LYSO crystals with depolished lateral surfaces; on one side it is coupled to the photodetector (an array of SiPM), and on the other one to a light guide and a reflector (see figure 5.2). This configuration allow to share the scintillation light emitted by each crystal among the other pixels and to collect it with all photodetector channels.

Each SiPM provides an integrated charge and a timestamp. These quantities, as explained in more detail in chapter 4, are necessary to determine in which pixel the primary gamma photon interacted, how much energy was deposited, at which position (DOI coordinate) and when. In particular, the light distribution across the array of photodetectors allows also to select ICS events: these are the events that fall between the cluster of full energy deposition event in each crystal.

To solve the ICS kinematic involving two crystals, we apply a two-steps procedure:

- the two hypothesis in which each of the two crystals is hit first are considered separately, and for both the most likely depths of interaction and energies deposited are calculated;

- subsequently, the probability of the two hypothesis are computed and compared, and the most likely one is selected.

5.2.1 Notation

In reference to figure 5.3, we consider two hypothesis: $K_0 = (A \rightarrow B)$ (right) and $K_1 = (B \rightarrow A)$ (left). For each of the two hypothesis, the algorithm iterate every possible combination of (z_A, z_B) and compute the expected light output Q_m for each photodetector channel D_m. Q_m is computed as

$$Q_m = M_m^{(A)}(z_A, E_A) + M_m^{(B)}(z_B, E_B) \tag{5.1}$$

where $M_m^{(A)}(z_A, E_A)$ is the light expected in photodetector channel D_m due to a deposition of energy E_A at DOI z_A in crystal A and $M_m^{(B)}(z_B, E_B)$ the light expected in photodetector channel D_m due to a deposition of energy E_B at DOI z_B in crystal B. The complete set of $N \times M$ maps $M_m^n(z, E)$ for any Crystal C_n and photodetector channel D_m is obtained through a calibration procedure that will be described in the next section.

The $\{Q\}$ values are then compared to $\{q\}$, the measured charges in the corresponding photodetector channel. To estimate the most likely combination of (z_A, z_B) for each of the two hypothesis K_0 and K_1, a χ^2 value is computed for every (z_A, z_B) couple. The best couple $(z_A^{best}, z_B^{best})^0$ and $(z_A^{best}, z_B^{best})^1$ are then used to compute an overall probability P_K for both hypothesis.

The probability P_K is computed as
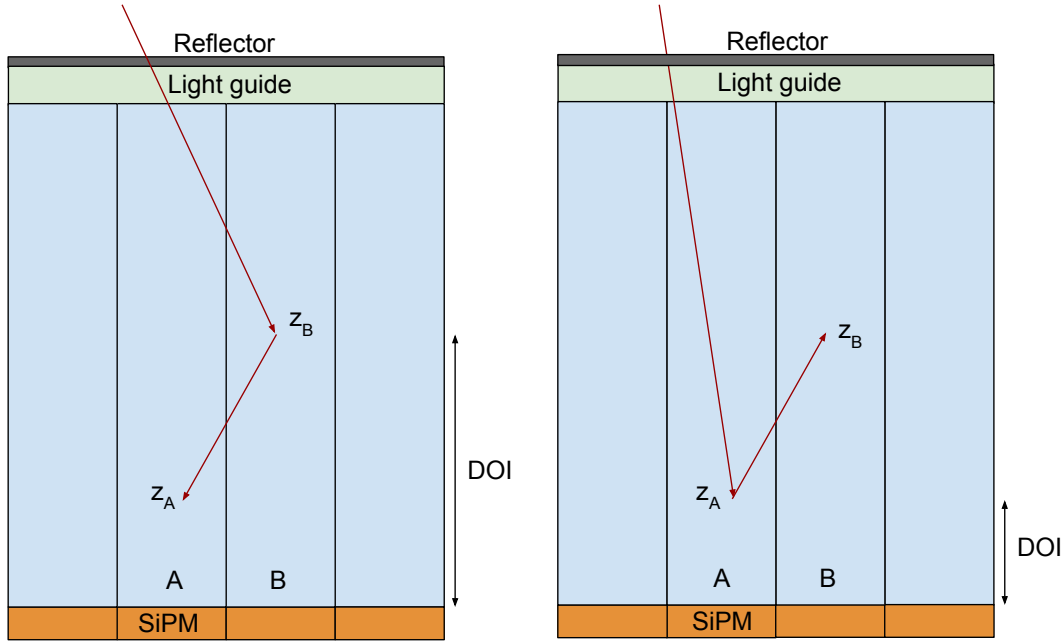
FIGURE 5.3: An illustration of the ambiguity in the photon trajectory in case of ICS events.

$$P_K = P_{l_0} \times P_{Compton} \times P_{l_1} \times P_{PE} \times P_q \quad (5.2)$$

where

- P_{l_0} is the probability for the gamma photon to reach the first interaction point. It is a function of the energy of the incoming gamma photon;

- $P_{Compton}$ is the probability for a Compton scatter at the first interaction point towards the interaction point in the second crystal. It is a function of the energy of the incoming gamma photon and of the scattered one (the latter is determined by the two coordinates (z_A, z_B))

- P_{l_1} is the probability for the scattered gamma photon to travel between the first interaction point and the second one. It is a function of the energy of the scattered gamma photon;

- P_{PE} is the probability for a photoelectric interaction of the scattered gamma photon. It is a function of the energy of the scattered gamma photon;

- P_q is the probability of detecting the charges q_m given the expected values Q_m.

P_0 and P_1 are compared and the *K* hypothesis with the corresponding highest probability is chosen.

5.3   Simulations

A preliminary study of the method was done using the *Geant*4 simulation toolkit (Agostinelli et al., 2003, Allison et al., 2006 and Allison et al., 2016). In the simulation, each crystal C_n of the matrix is irradiated with a beam of 511 keV gamma rays. The full ray-tracing simulation of the DOI detector has been prepared, allowing to track all the interactions of the primary gamma ray with the crystal pixels, as well as the propagation of the optical photons across the module and their final impact point in each photodetector channel. An scheme of the setup used is shown in figure 5.4. Throughout the chapter, the coordinate system used is the same as in Geant4 (the reference system is shown in figure 5.4 as well); in particular, it is worth noticing the DOI coordinate, which runs from -7.5 mm (where the gamma photons enter the matrix) to 7.5 mm (where the photodetector is coupled to the crystals).

5.3.1   Simulation description

The detectors simulated are the one described in section 3.1.1, both in the 16 and 64 pixel configurations. The material is LYSO, defined in Geant4 as a combination of Lutetium, Silicon and Oxygen with density of $7.1 g/cm^3$ and Light Yield of 40000 photons per MeV. The depolishing of the lateral surfaces is implemented, through the Unified model for ground surfaces, with the parameter SigmaAlpha set to 0.221 (value obtained from previous studies).

For each event, all the optical photons are propagated by the software, and for each photon the coordinates (space and time) of the interaction with the photodetector are saved. The Photon Detection Efficiency (PDE) of the photodetector is set to 40% (as stated from Hamamatsu for the SiPM array used in the experimental measurements) and a gaussian smearing is applied to each timestamp, in order to account for the Single Photon Time Resolution (SPTR) of the photodetector.
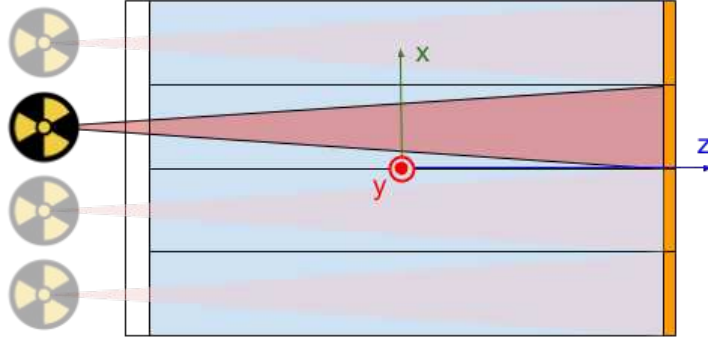
FIGURE 5.4: Scheme of the setup used for the simulation, with
the system of coordinated highlighted

The analysis software selects events with energy depositions in a single crystal, sum the energy deposited in each energy deposition, compute the z coordinate and record for all the optical photons emitted in these energy depositions the point of impact with the SiPM array, assigning them to the different photodetector channels $\{D\}$. These are the $\{q\}$ values later used by the Compton algorithm.

5.3.2 Calibration

In order to obtain the $N \times M$ maps $M_m^n(z, E)$ set, a Calibration procedure is needed.

Primary gamma photons are propagated by the software, but only events with energy deposition in just the C_n pixel under study are selected. For every such event, the coordinate of interaction z, the energy deposited E and the light q_m seen by each photodetector D_m in the SiPM are stored. For every photodetector channel D_m, the light q_m collected is plotted as a 2D-distribution as a function of the the coordinate of interaction z and the energy deposited E. An example of one of these plots is shown in figure 5.5.

This distribution is fitted with a plane with equation

$$f(z, en) = p_{00} + p_{10} \cdot z + p_{01} \cdot en_{deposited} \tag{5.3}$$

and the obtained fit function is used as map $M_m^n(z, E)$ for the light output of channel D_m when an energy E is deposited in crystal C_n at DOI z. The fit of the distribution plotted in figure 5.5 is shown in 5.6, with the contour plot of the fit plane shown in figure 5.7. As an example of the light output in one of the lateral channels, a fit is shown in figure 5.8 for the crystal on the right of
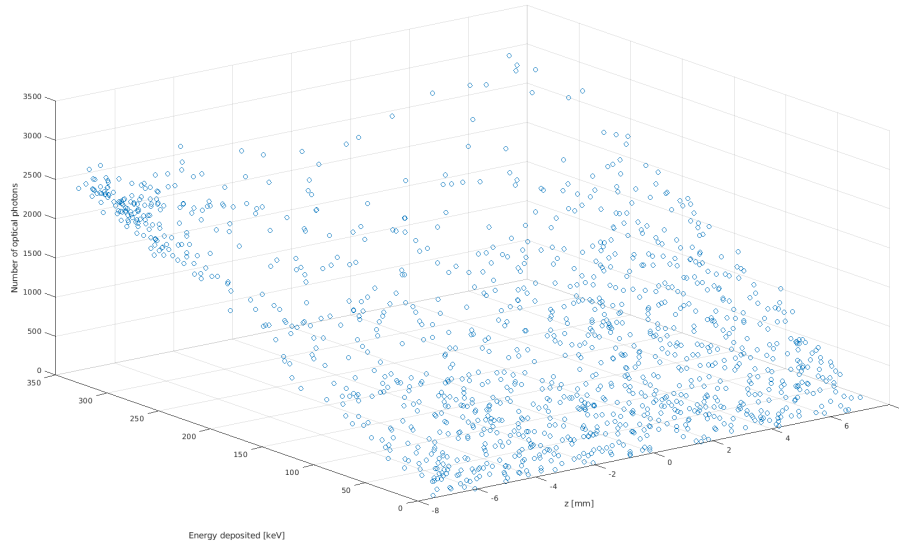
FIGURE 5.5: Example of one of the 64×64 maps $D_m^{(n)}(z, E)$

the one hit by the gamma photon: as we can see from the color levels (figure 5.9), in this case higher light outputs correspond to lower DOI in the crystal of first interaction.

With the same dataset, all the maps for the other photodetector channels $\{D\}$ are obtained. The procedure is then repeated for every other crystal in the matrix, resulting in $N \times M$ maps $M_m^{(n)}(z, E)$.

5.3.3   Evaluation of the method

Once the calibration maps $M_m^{(n)}(z, E)$ are ready, it is possible to test the method. In this case, only events where energy deposition happens in two crystals are selected from the simulation. As explained in section 5.2, the algorithm look for a set of values $(z_A, z_B)^{(K)}$ for the hypothesis K_0 and K_1 by comparing the response obtained in the simulation (charges $\{q\}$) with the one predicted according to the calibration maps (charges $\{Q\}$).

The scan of the coordinates (z_A, z_B) happens over a fine grid of elements (300 values for each coordinate, as tradeoff between accuracy and computational cost), and for each couple of positions, the energies deposited (E_A, E_B) are computed from the Compton scattering formulas:

$$E_B = \frac{E_{511}}{1 + (E_{511}/(m_e c^2)(1 - cos\theta)} \tag{5.4}$$
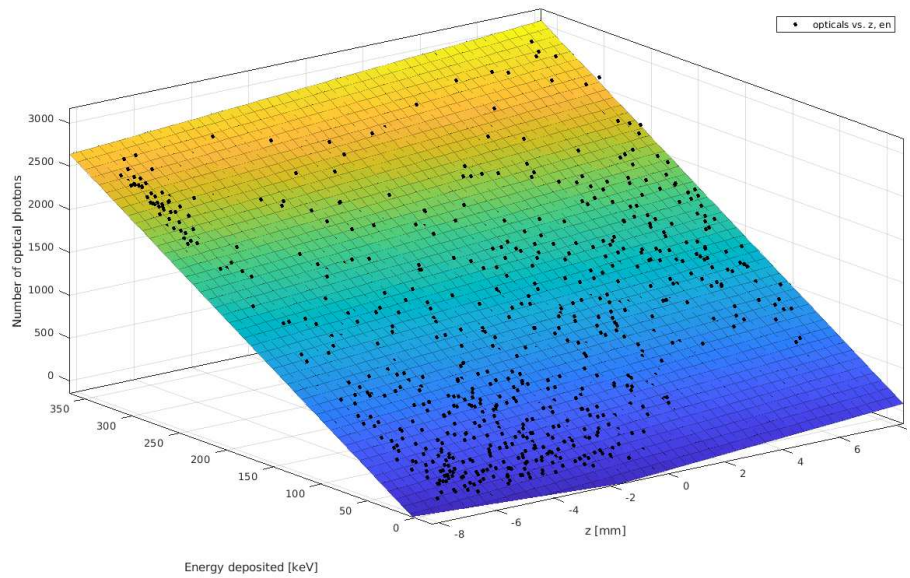
FIGURE 5.6: Fit of the distribution of $M_m^n(z, E)$ for the photodetector channel coupled to the crystal i=3,j=4 (hit by the gamma photon). Fit equation $f(z, en) = p00 + p10 * z + p01 * energy_deposited$, fit parameters $p00 = 22.3$, $p10 = 23.7$ and $p01 = 7.6$

FIGURE 5.7: Contour plot of the fit shown in figure 5.6, highlighting the dependence of the light output on (z, Energy deposited)
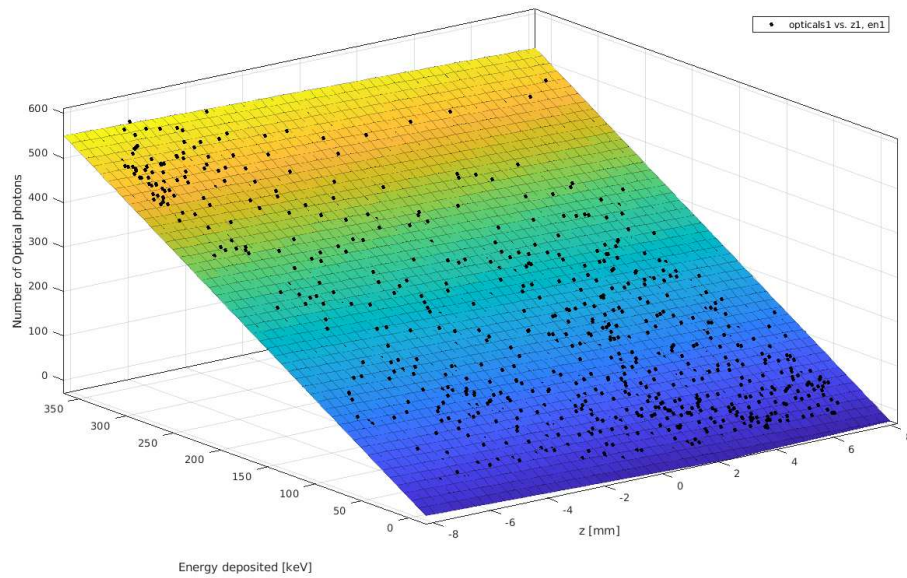
FIGURE 5.8: Fit of the distribution of $M_m^n(z, E)$ for the photode-tector channel coupled to the crystal i=3, j=3 (next to the crystal 28, hit by the gamma photon). Fit equation $f(z, en) = p00 + p10 * z + p01 * energy_d eposited$, fit parameters $p00 = -0.1$, $p10 = -1.7$ and $p01 = 1.4$
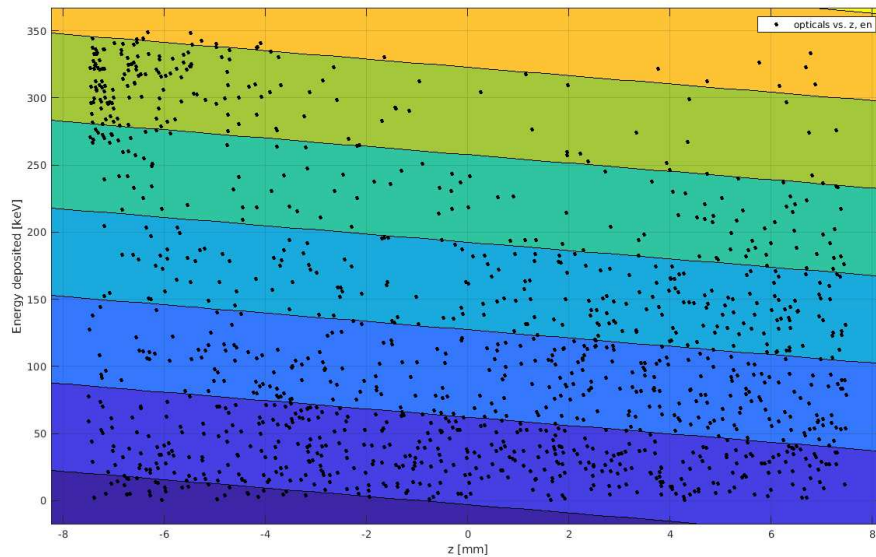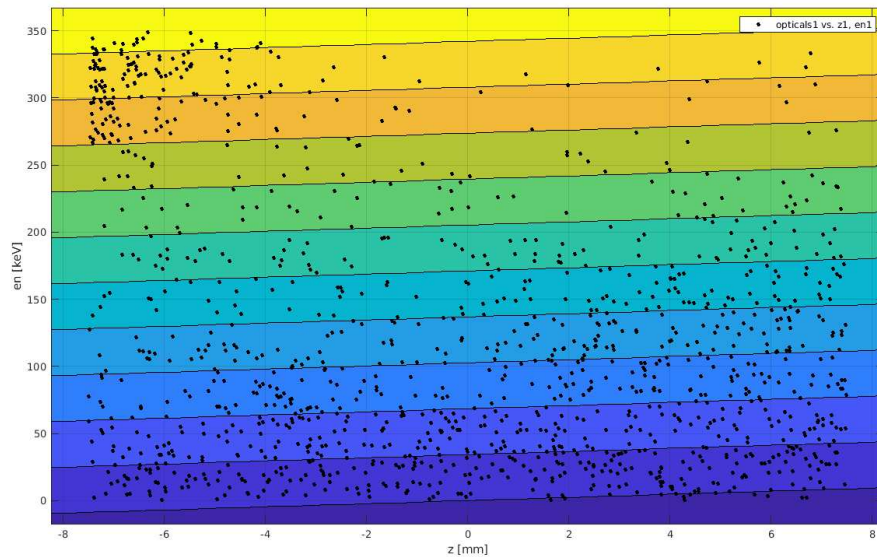

FIGURE 5.9: Contour plot of the fit shown in figure 5.8, high-lighting the dependence of the light output on (z, Energy de-posited)
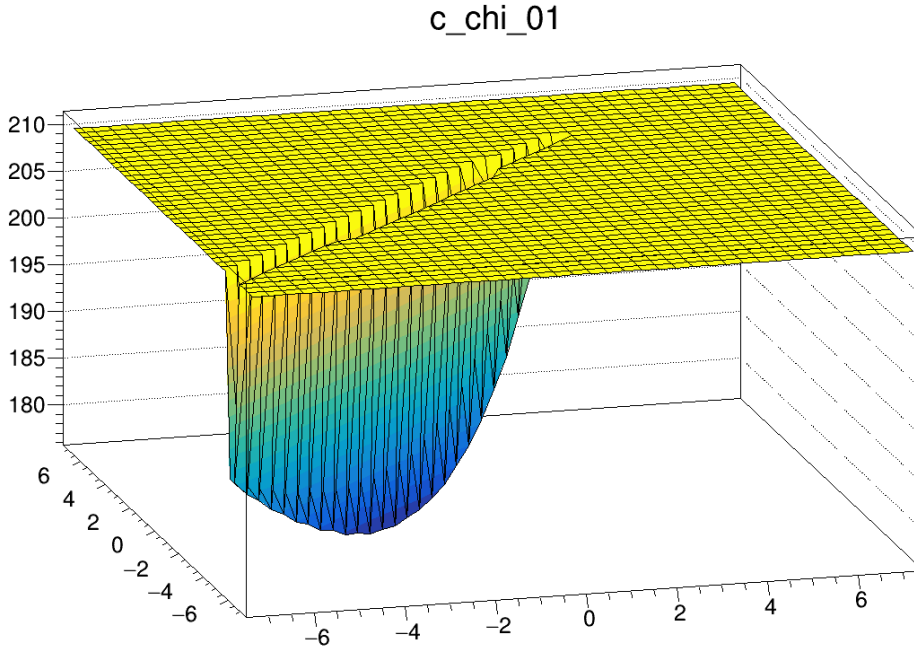
FIGURE 5.10: Example of χ^2 quantity to be minimized

$$E_A = E_{511} - E_B \tag{5.5}$$

The values (z_A, E_A) and (z_B, E_B) are plugged in the corresponding maps $M_m^{(A)}(z_A, E_A)$ and $M_m^{(B)}(z_B, E_B)$ for every photodetector channel D_m and the obtained charges Q_m are compared to the values from simulation q_m to give a χ^2 value. In figure 5.10 is shown the $\chi^2(z_A, z_B)$ surface for the hypothesis K_0 for one event as an example.

The minimum of the surfaces for the hypothesis K_0 and K_1 are found using the TMinuit package of ROOT, yielding $(z_A^{best}, z_B^{best})^0$ and $(z_A^{best}, z_B^{best})^1$. For each hypothesis the probability described in equation 5.2 is subsequently computed using these values, in order to pick K_0 or K_1. The algorithm is considered to give a correct prediction for the event if the choice between K_0 and K_1 corresponds to the truth from the simulation.

5.4 Results and discussion

The parameter used to assess the performance of the algorithm is the accuracy, defined as
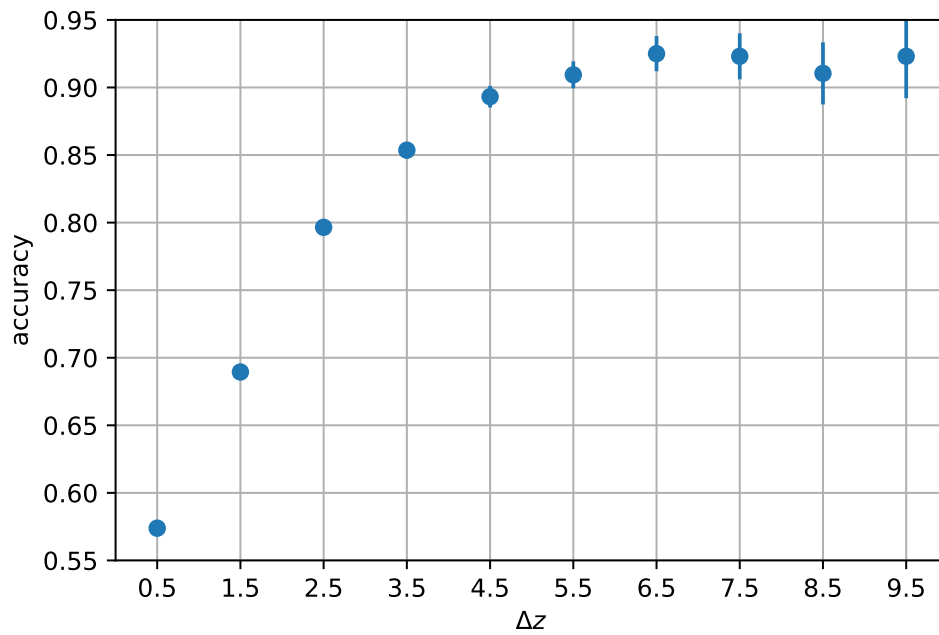
FIGURE 5.11: Accuracy of the algorithm (average over the 4x4 array, expressed as ratio) as a function of the relative distance, in mm, between the two interaction points.
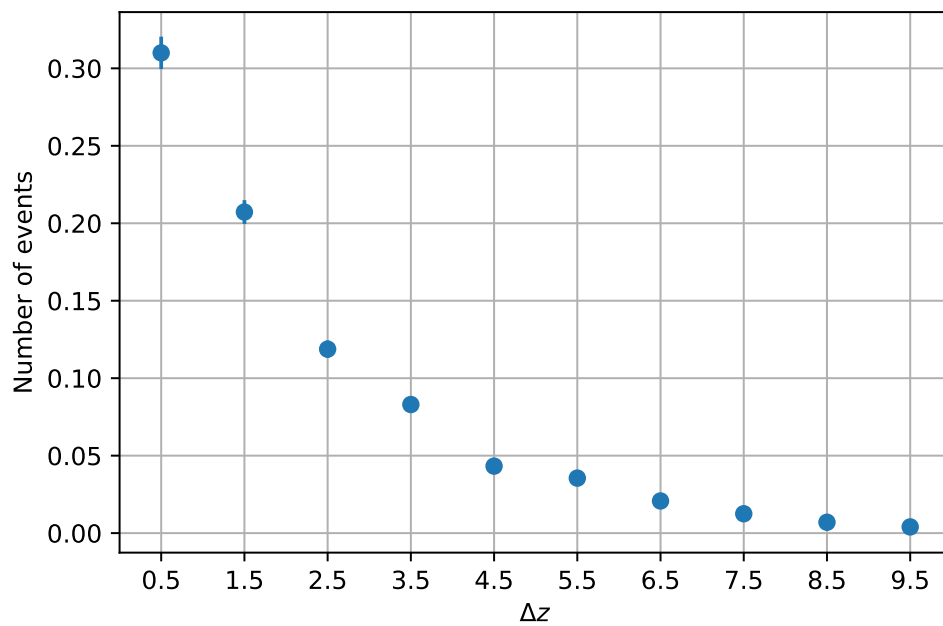
FIGURE 5.12: Number of events in each range of Δz (mm) for the 4x4 array.

$$accuracy = \frac{N_{correct}}{N_{ICS}} \tag{5.6}$$

where $N_{correct}$ is the number of events where the algorithm correctly identified the crystal of first interaction and N_{ICS} is the total number of ICS events selected.

As shown in figure 5.11, where the accuracy (expressed as ratio) is plotted as a function of the quantity Δz (the difference between the DOI of energy deposition in the two crystals involved in the ICS), there is a correlation between these two variables. In fact, the accuracy of the method is poor for events with low Δz (< 1-2mm): in these cases, because of the angle θ of the Compton scattering, the energy is shared in almost equal parts between the two pixels, resulting in a very similar light output from both crystals. In such events, the probabilities of the ICS kinematics is almost symmetric between K_0 and K_1.

On the other hand, as Δz increases (> 2mm), the accuracy rapidly increases as well, reaching values up to 90% the events with high Δz (> 5mm). In figure 5.12 is shown the percentage of events for every range of Δz: because of the pixels geometry and the solid angles, the number of events decreases as Δz increases. Overall, the algorithm has an accuracy higher than 70% for at least 50% of the total number of ICS events.

Similar results have been obtained with the 8×8 LYSO array, with the plot for the accuracy already discussed for the 4×4 matrix shown in figure 5.14.

5.5 Conclusion

The algorithm developed to resolve the kinematic in ICS events has shown promising preliminary results. The accuracy is higher than 70% for at least 50% of the events, peaking at values higher than 90% for events with a high difference in terms of coordinates of energy deposition.

The calibration stage could be further optimized, like the minimization technique and the Probability computation. The impact of these events on the reconstructed images has to be investigated; however, these results show already the potential to increase the sensitivity parameter.
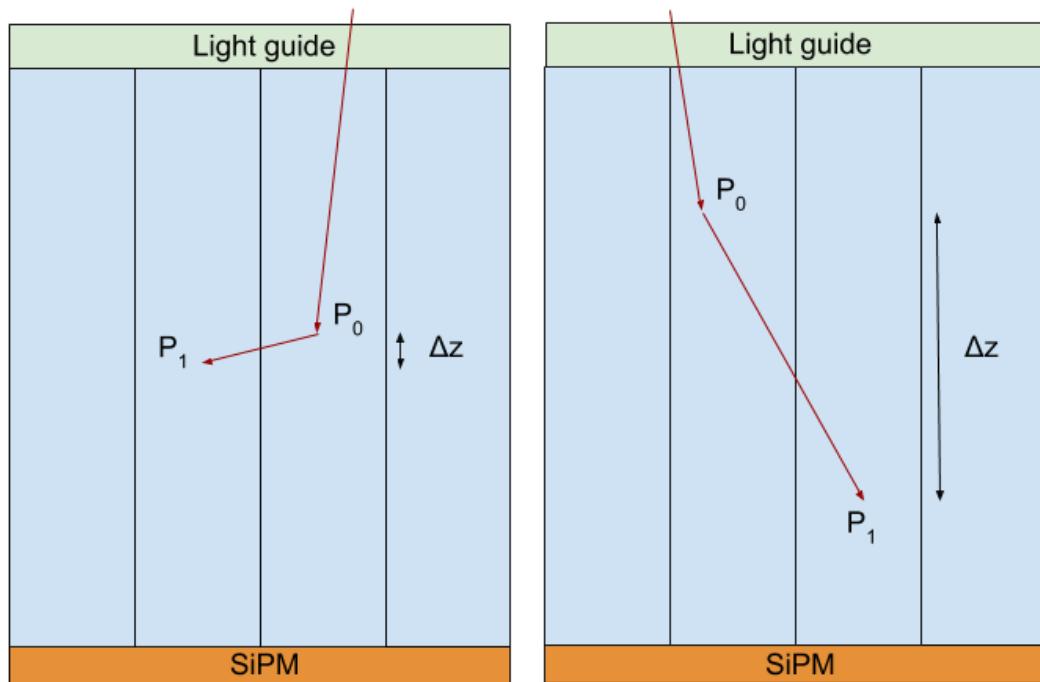
FIGURE 5.13: Left: example of an ICS event with similar z in
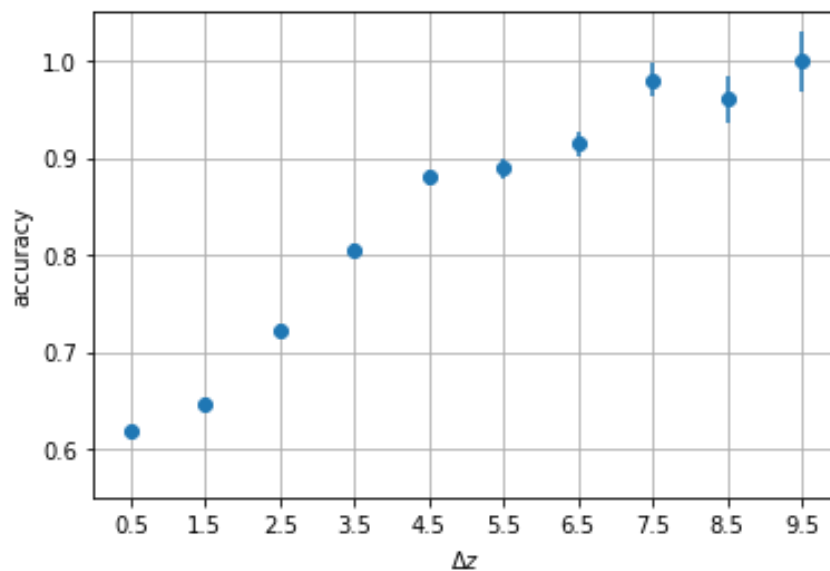both crystal. Right: example of ICS event with high Δz

FIGURE 5.14: Accuracy of prediction (average over the 8x8 array) as a function of the relative distance between the two interaction points (Δz) in mm.

In the next chapter the method will be adapted and tested in an experimental setup, to assess the real performances with the acquisition system introduced in chapter 4.

References

Agostinelli, Sea et al. (2003). "GEANT4—a simulation toolkit". In: *Nuclear instruments and methods in physics research section A: Accelerators, Spectrometers, Detectors and Associated Equipment* 506.3, pp. 250–303.

Allison, J et al. (2016). "Recent developments in Geant4". In: *Nuclear Instruments and Methods in Physics Research Section A: Accelerators, Spectrometers, Detectors and Associated Equipment* 835, pp. 186–225.

Allison, John et al. (2006). "Geant4 developments and applications". In: *IEEE Transactions on nuclear science* 53.1, pp. 270–278.

Clerk-Lamalice, Julien et al. (2012). "Evaluation of easily implementable inter-crystal scatter recovery schemes in high-resolution PET imaging". In: *2012 IEEE Nuclear Science Symposium and Medical Imaging Conference Record (NSS/MIC)*. IEEE, pp. 2196 –2199.

Comanor, KA, PRG Virador, and WW Moses (1996). "Algorithms to identify detector Compton scatter in PET modules". In: *IEEE transactions on nuclear science* 43.4, pp. 2213–2218.

Gillam, John E et al. (2014). "Sensitivity recovery for the AX-PET prototype using inter-crystal scattering events". In: *Physics in Medicine & Biology* 59.15, p. 4065.

Peng, Peng, Martin S Judenhofer, and Simon R Cherry (2019). "Compton PET: a layered structure PET detector with high performance". In: *Physics in Medicine & Biology* 64.10, 10LT01.

Shao, Yiping et al. (1996). "A study of inter-crystal scatter in small scintillator arrays designed for high resolution PET imaging". In: *IEEE Transactions on Nuclear Science* 43.3, pp. 1938–1944.

Zeraatkar, N et al. (2011). "Monte Carlo-based evaluation of inter-crystal scatter and penetration in the PET subsystem of three GE Discovery PET/CT scanners". In: *Nuclear Instruments and Methods in Physics Research Section A: Accelerators, Spectrometers, Detectors and Associated Equipment* 659.1, pp. 508–514.

Chapter 6

ICS: measurements

6.1 Introduction

In order to identify Inter-crystal Compton Scatter events in an experimental setup with a pixelated detector, a multi-channel readout system with high energy and time resolution is needed; this setup was described in chapter 4.

Moreover, in order to correctly assign the scintillation event to the crystal of first interaction, it is also necessary to develop a technique to solve this task: this was the algorithm presented and preliminarily validated through simulations in chapter 5.

In this chapter, we are going to test the algorithm on the DOI-capable light-sharing module with our DAQ system, to investigate the possibility to apply it in near future state-of-the-art detectors.

6.2 Experimental setup

Throughout this chapter, the modules tested will be those described in section 3.1.1: a LYSO matrix coupled to a Hamamatsu photodetector array and a light guide to allow light sharing. As in the previous chapters, the couplings tested were two: a $1:1$ coupling with a 4×4 crystal matrix coupled to a 4×4 photodetector array and a $4:1$ coupling with an 8×8 crystal matrix coupled to the same photodetector array.

The DAQ system used was described and characterized in section 3.2: it consists of a multi-channel parallel readout of the charge and time signals with high energy and time resolution.

The setup used were two: one for the calibration measurement and one for the validation phase. Both are based on a sodium-22 source (with diameter D
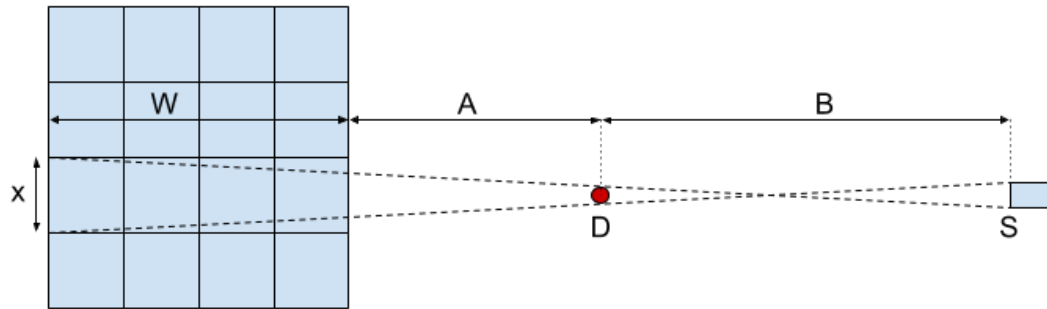
FIGURE 6.1: Scheme of the setup used for calibration measurements

CHECK) and a secondary small LYSO reference crystal, in coincidence with the matrix under study.

6.2.1 Calibration setup

The setup used for calibration is the same as the one described in section 4.2.4: sodium source and reference crystal are kept on the side of the matrix, and shifted along the main axis of the crystal pixels in order to irradiate them at different DOI positions. The relative distances between matrix, source and reference crystal are such that the gamma beam is narrow enough to irradiate only one crystal even in its widest point, at the opposite side of the matrix from the gamma source (see figure 6.1). With reference to figure 6.1, the distance *A* between matrix and source was 1 cm and the distance *B* between point source and reference crystal was 5 cm.

6.2.2 Validation setup

For the validation measurements, the setup was described in section 4.3.4: in this case the source and the reference crystal lay on the line described by the main axis of the crystal pixel, each time different of each element of the matrix. Also in this case, the relative distances between matrix, source and reference crystal are such that the gamma beam is narrow enough to irradiate only one crystal at its widest point, at the opposite side of the matrix from the gamma source, close to the photodetector (see figure 6.2). With reference to figure 6.2, the distance *A* between matrix and source was 1 cm and the distance *B* between point source and reference crystal was 5 cm.

FIGURE 6.2: Scheme of the setup used for validation measurements

6.3 Calibration

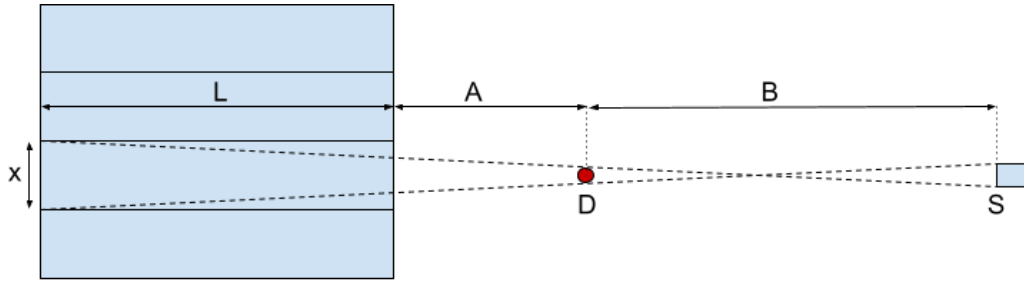Experimentally, the calibration maps $M_m^{(n)}(z, E)$ were obtained through a lateral scan of the crystal matrices. Using figure 6.3 as a reference, each row of pixels was irradiated at multiple positions along with the crystals, ensuring that each acquisition was long enough to have sufficient statistics in the crystal most distant from the source. This results in acquisitions at multiple DOI positions for each crystal, and for all events of each acquisition in each crystal the light measured in all the SiPM channels was recorded.

The matrix is shifted up and down and left and right using two linear stages, which ensure high spatial resolution and the automation of the whole acquisition.

As an example for the 4×4, the flood map for the second row of crystals, at $DOI = 7mm$, is shown in figure 6.4. In this plot, four distinct clusters of events are present, one for each pixel. These clusters are connected by events falling in a straight line: these are events where the energy is shared between more than one pixel, among the irradiated ones. Finally, there are some events that lie on lines connecting these pixels to other, non-irradiated ones. These are events in which the photon from the source deposit a fraction of energy through Compton scattering in one of the irradiated crystal and the remaining part in one of the neighboring one.

The same plot is shown in figure 6.5 for the 8×8 matrix; in this case, as there are 8 crystals for each row of the matrix, 8 different clusters of events are visible, aligned along the gamma beam line.

The datasets for each row were subsequently merged, gathering events for each crystal at multiple DOI. The events relative to a single crystal, those accumulating in the clusters shown in figure 6.4 and 6.5, were selected and for
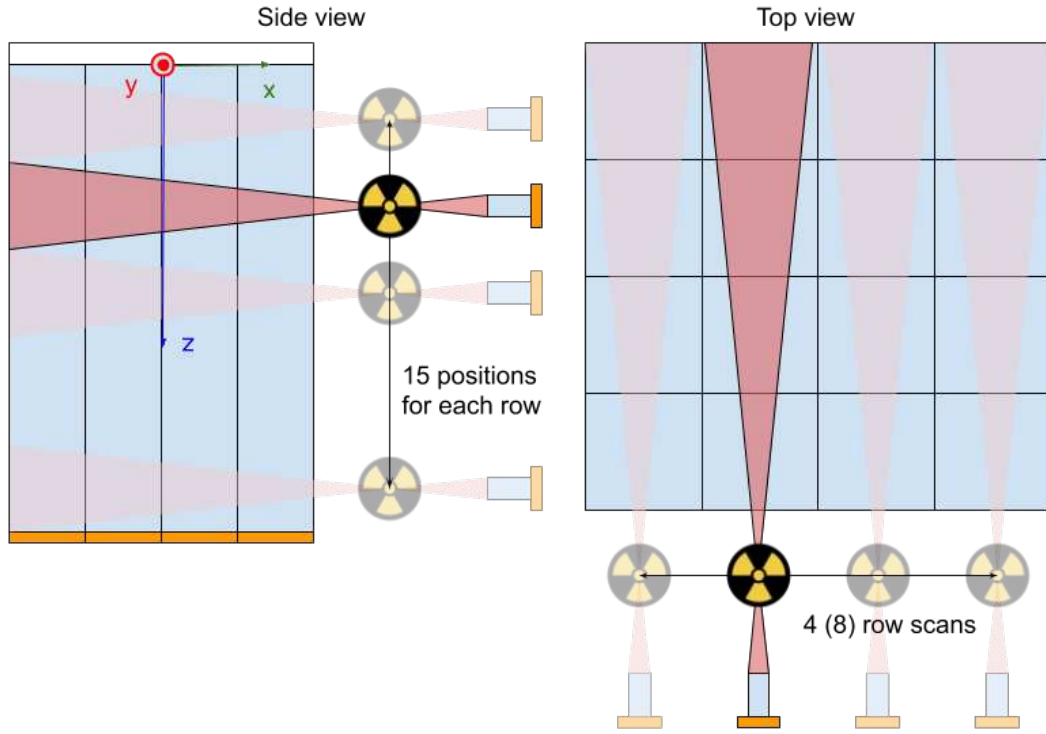
FIGURE 6.3: Scheme of the setup used for calibration measurements

each pixel the maps for the light output in every other photodetector channel were obtained. As we can see from figure 6.6, differently from what happened in the simulations, here the events are discretely distributed along the z axis. This is due to the fact that the lateral scan happens at multiple DOI, each $1mm$ apart. In the case of measurement data, the fit was more stable excluding events in the photopeak region; this is not a limitation because the calibration functions are used for events involving a Compton scatter and therefore with energies included in the fit region.

However, they still lay on a plane and therefore the same procedure as explained in section 5.3.2 was applied to these distributions: a fit with a linear function of the two coordinates z and E,

$$f(z, E) = p_{00} + p_{10} \cdot z + p_{01} \cdot E \tag{6.1}$$

whose parameters p_{00}, p_{10} and p_{01} are used for the calibration maps $M_m^{(n)}(z, E)$. In case of measurements, the E coordinate was obtained from the ADC channels using the calibration functions described in section 3.3.2.

FIGURE 6.4: Flood map ((x, y) plane) of the events in an acquisition for calibration. 4×4 module, DOI = 7mm, second row of crystals

FIGURE 6.5: Flood map $((x, y)$ plane) of the events in an acquisition for calibration. 8×8 module, DOI = 7mm, fourth row of crystals
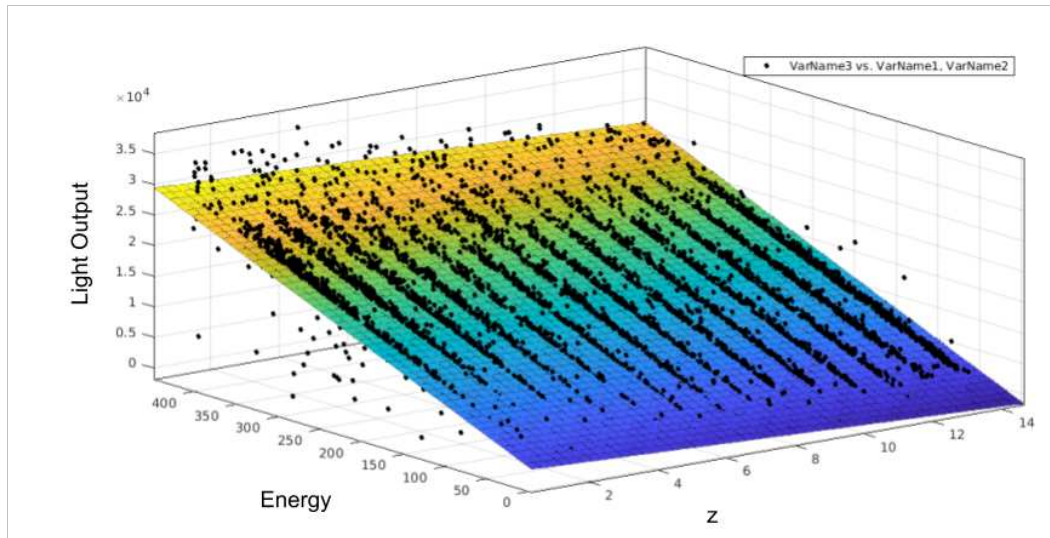
FIGURE 6.6: Planar fit of the distribution of $M_m^n(z, E)$ for the photodetector channel coupled to the crystal hit by the gamma photon
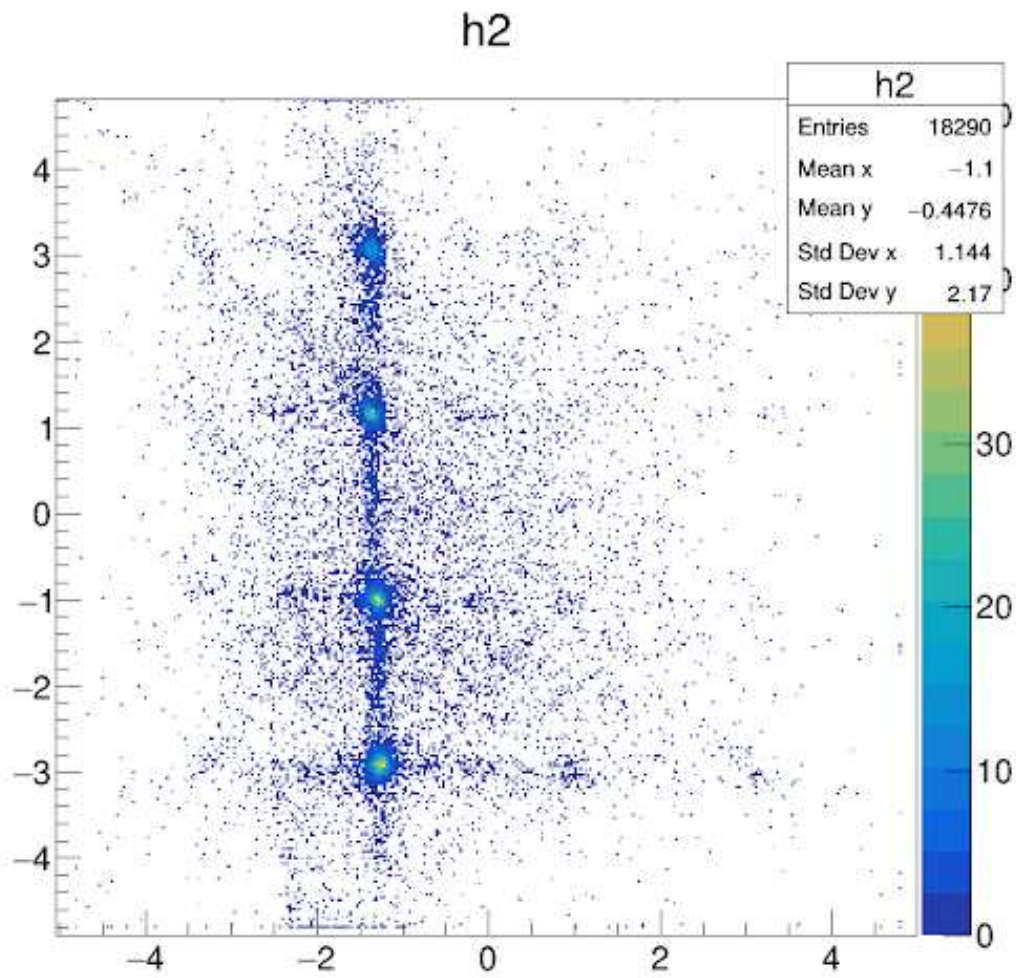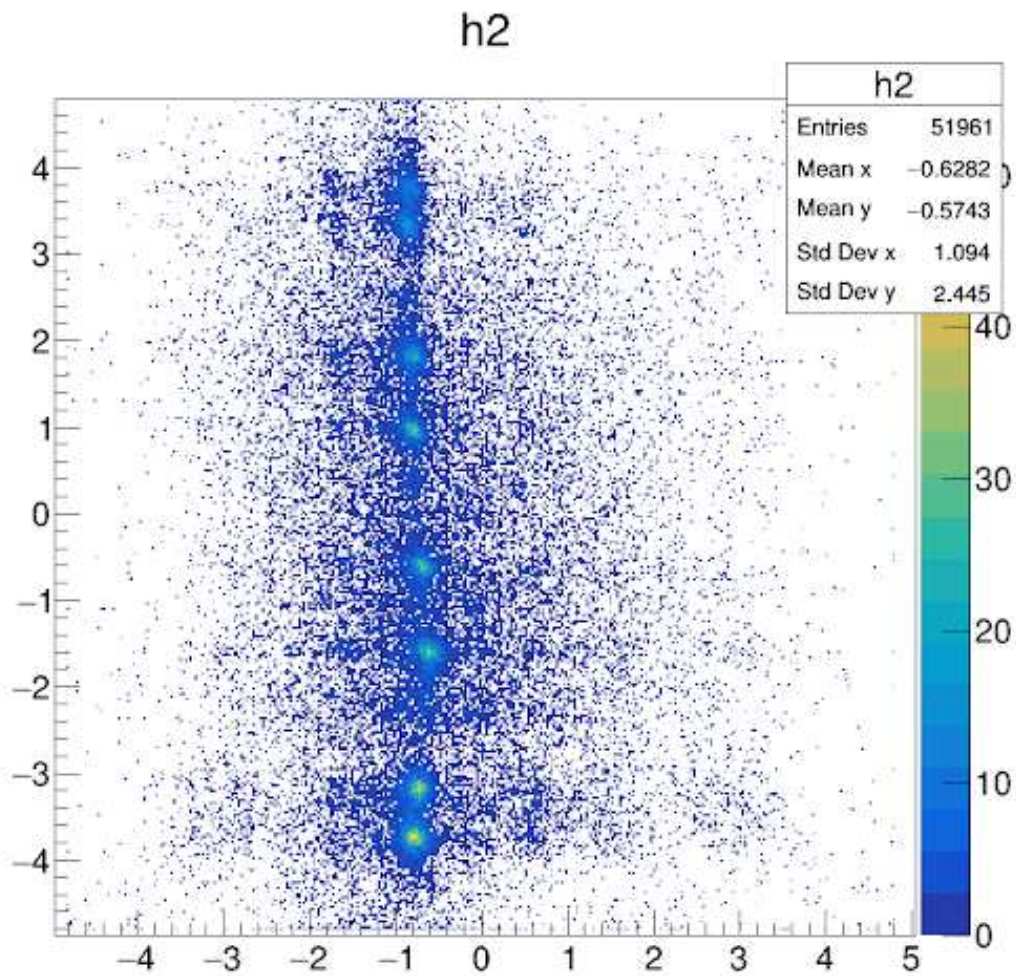
6.4 Validation

In the case of the measurements with the experimental setup, the validation was done using a narrow beam focused on a single crystal. With reference to figure 6.7, the gamma photons enter the matrix from the side opposite to the photodetector, as they would in a PET scanner.

Figure 6.8 shows the flood map for the acquisition relative to a single crystal. As we can see, only one cluster is present in this case: these are the event with full energy deposition in the pixel irradiated. From this spot, many lines go in the direction of other pixels: these are the events in which energy is shared between two crystals thanks to Compton scattering.

The validation measurements are repeated for every crystal, obtaining a dataset similar to the one shown in figure 6.8 for every other pixel. The fact that the beam is narrow enough to hit only one pixel at a time, allows obtaining datasets in which the crystal of first interaction is know by construction.

The algorithm is then applied to Compton events selected from each dataset. These are the events that lie, in the flood map, between the two crystals under study. The choice of the two crystals for the algorithm to consider is based on the amount of light that reaches the photodetector channels: the two channels with the highest output are used as hypothesis K_0 and K_1 (Comanor, Virador, and Moses, 1996). This way, the method is not relying on the position of the beam as information to determine which crystals to consider as candidates
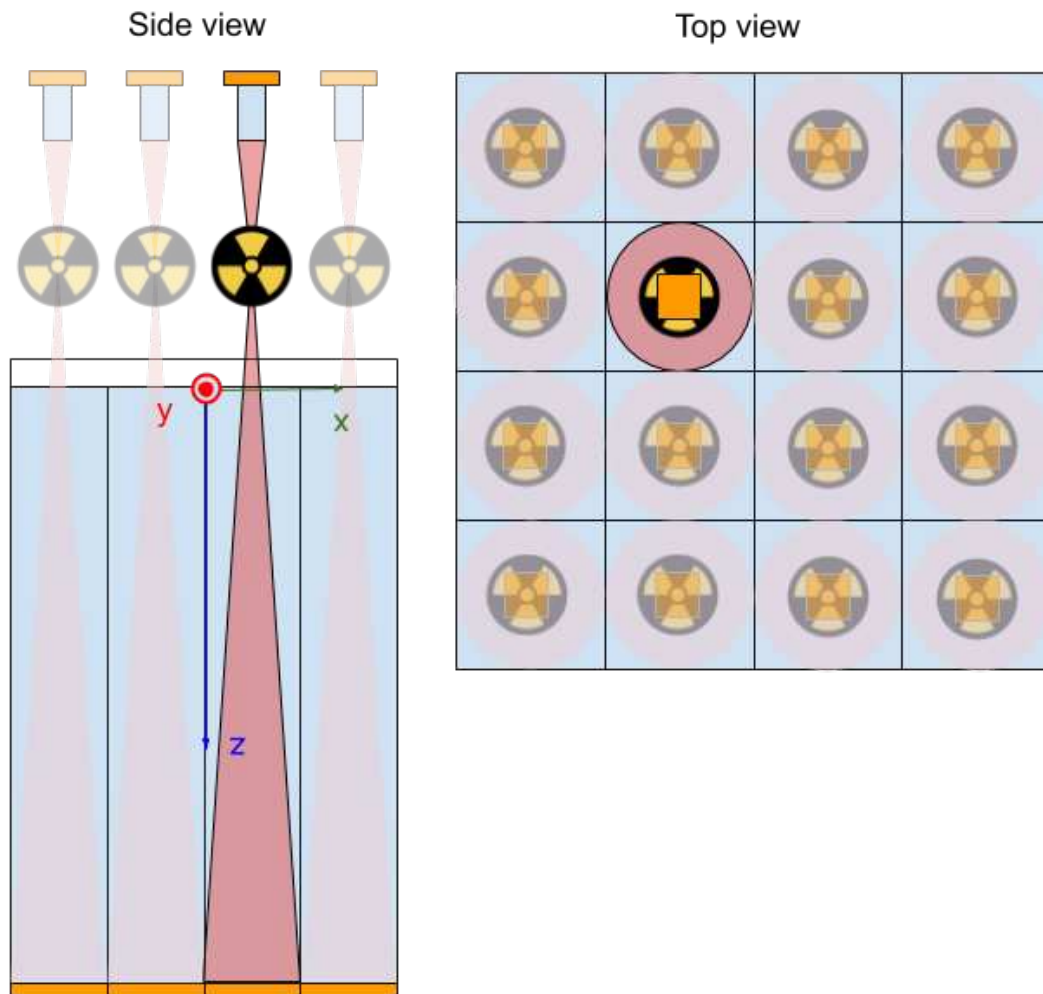
FIGURE 6.7: Scheme of the setup used for validation measurements
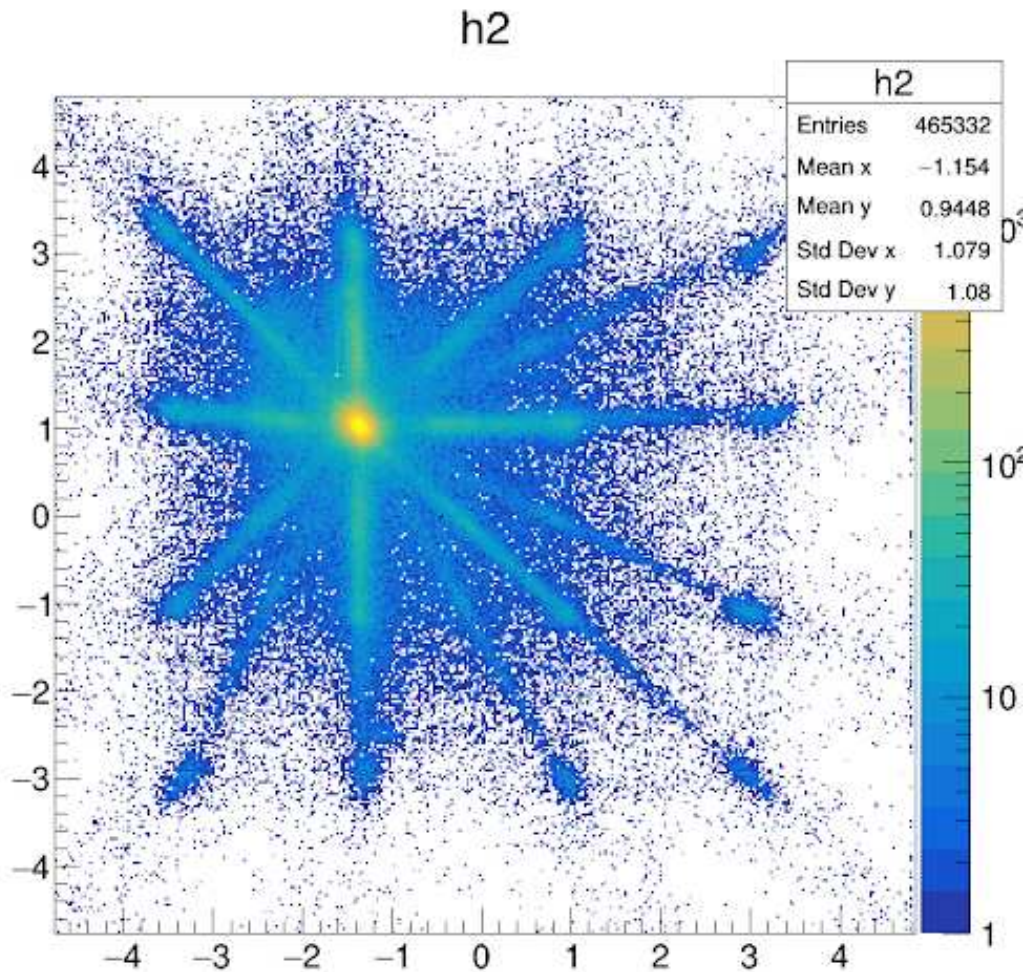
FIGURE 6.8: Flood map $((x, y)$ plane) of the events in an acquisition for validation. 4×4 module, crystal i=1, j=2

for the scattering event. The beam position, in fact, is only used at *truth* for the computation of the accuracy.

This selection procedure is enough for the 4×4 matrix; in the case of the 8×8 matrix, however, there are 4 crystals coupled to each SiPM channel. In this case, the additional information provided by the (u, v) coordinate of each event is used (see figure 6.9): after the selection of the SiPM candidate, the crystal to consider is chosen depending on the (u, v) coordinate of the event.

As with simulations, the measurement was carried out both on 4×4 and 8×8 matrices.
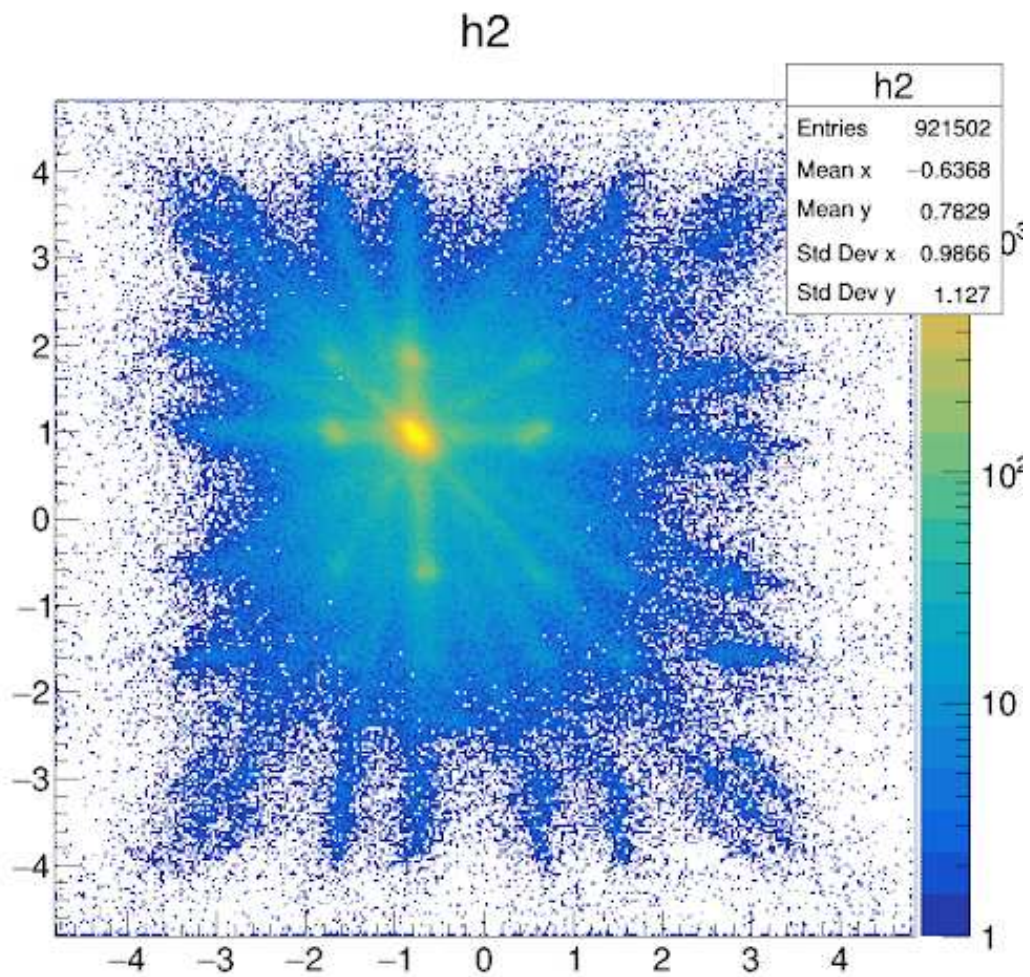
FIGURE 6.9: Flood map ((x, y) plane) of the events in an acquisition for validation. 8×8 module, crystal i=3, j=4

array type	simulations	measurements
4 ×4	(71 ±1)%	(65 ±0.5)%
8 ×8	(74 ±1)%	(68.5 ±0.5)%

TABLE 6.1: Overview of the accuracy obtained with simulations and measurement (average on all channels)

6.5 Results and discussion

The accuracies obtained, as an average across all the channels, are summarised in table 6.1 for both matrices. As a reference, the average from the simulations is reported as well; because with measurements data it is not possible to sort events depending on their Δz (this quantity in fact is unknown experimentally), the accuracy from simulations is reported as an average of all events.

As we can see, the performance of the algorithm on the measurement data is lower compared to simulations. This could be explained with two reasons. First of all, calibration data from measurements show a lower uniformity compared to those from the simulation: in the case of the measurements, small imperfections in the coupling between crystal and light guide could result in inhomogeneity in the light sharing. Moreover the choice of the two crystals to consider for the algorithm is based on the amount of light seen in each photodetector channel. This method works well with simulation data, but could be affected by experimental errors in the case of measurement data.

The events were also discriminated according to two different classes of categories. With reference to figure 6.10, events were sorted in 3 categories, depending on the relative position of the crystals involved:

- *lateral*: for events where the two energy depositions happen in crystals having one face in contact;

- *diagonal*: for events where the two energy depositions happen in crystals having one edge in contact;

- *distant*: for events in crystals that do not share a face, but coupled to SiPM channels with either index i or j not more different than $\pm$ 2.

Events were also classified according to the position of the crystals involved relative to the matrix:
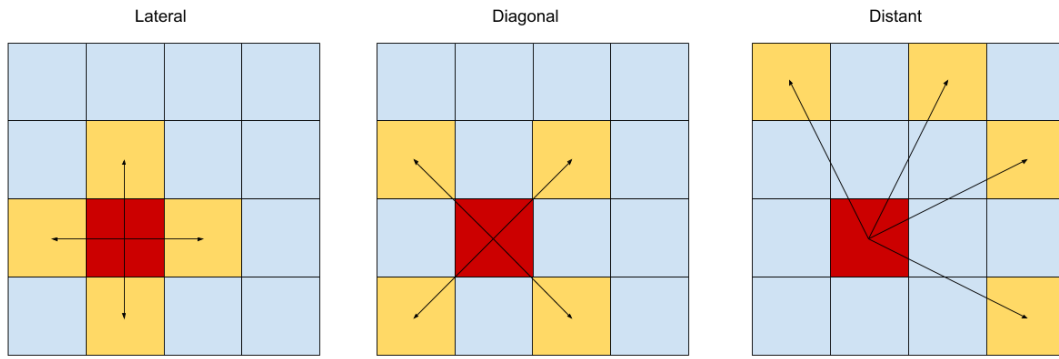
FIGURE 6.10: Different types of couples of crystals according to
their relative position in the matrix
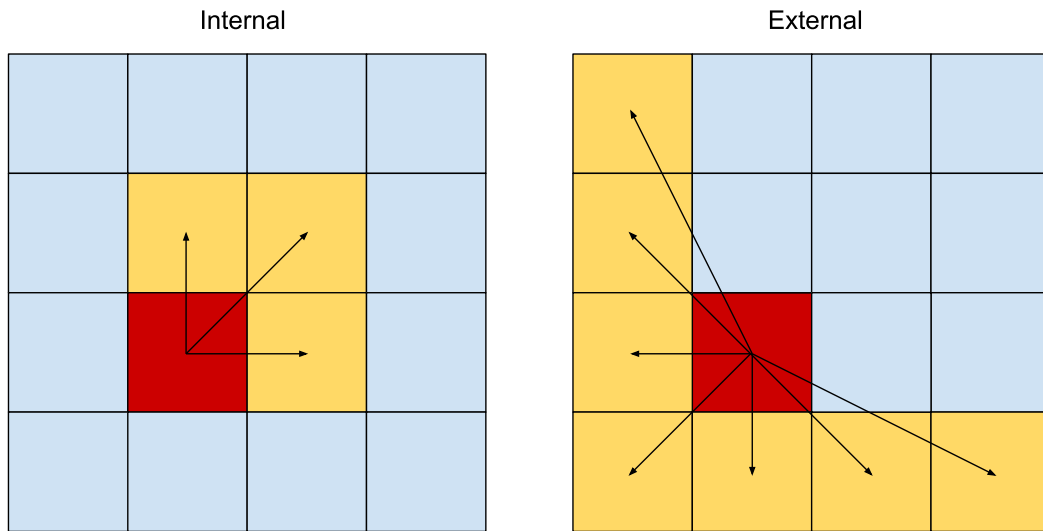
FIGURE 6.11: Different types of couples of crystals according to
their position inside the matrix

- *internal*: for events where both crystals involved are surrounded by
  other crystals;

- *external*: for events where only one of the two crystals involved is com-
  pletely surrounded by other crystals

The average of the events according to these two classifications are reported
in table 6.2 and table 6.3.

Looking at the dependence of the accuracy on the relative positions of the
two crystals involved in the scattering event (table 6.2), we notice higher val-
ues in the case of crystals coupled to adjacent SiPM channels, both for 1:1
and 4:1 couplings. This could be explained by the fact that light sharing in

array type	lateral	diagonal	distant
4 ×4	$(66.7 \pm 0.7)\%$	$(62 \pm 0.7)\%$	$(61 \pm 1)\%$
8 ×8	$(71.3 \pm 0.6)\%$	$(63 \pm 1)\%$	$(65 \pm 1)\%$

TABLE 6.2: Overview of the accuracy of the algorithm for *lateral*, *diagonal* and *distant* couples of crystals for both array types.

array type	internal	external
4 ×4	$(71.8\pm0.7)\%$	$(58.1\pm0.5)\%$
8 ×8	$(73.1\pm0.8)\%$	$(65.6\pm0.7)\%$

TABLE 6.3: Overview of the accuracy obtained for *internal* and *external* crystals with both array types

the back of the matrix is easier for crystals having one face in contact.

Considering instead the accuracy obtained for internal and external couples of crystal, the latter show lower values. This trend is found both in 4×4 and 8×8 matrices. A possible explanation for this loss in accuracy could be given by the fact that calibration maps for external crystals are less accurate compared to central crystals due to edge effect and light losses. However, for possible future application, considering the geometry of a full ring of detectors, most of the crystals would be surrounded by other crystals, being in fact in a configuration similar to the central crystals of our module. For this reason, the loss in accuracy caused by the edge effect in external crystals should not be a problem in an assembled scanner.

6.6 An improved event discrimination technique

In order to improve the accuracy of the algorithm, given the fact that with experimental data is not possible to operate a selection based on Δz between the two energy deposition, another selection method was found. The events in this case were sorted as a function of the difference between the probabilities P_0 and P_1 of the two hypotheses, K_0 and K_1. The assumption was that in case of similar coordinates of energy deposition in the two crystals, the light output is similar and therefore the two hypotheses are comparable. Once the events were sorted in increasing order of ΔP the accuracy of the algorithm
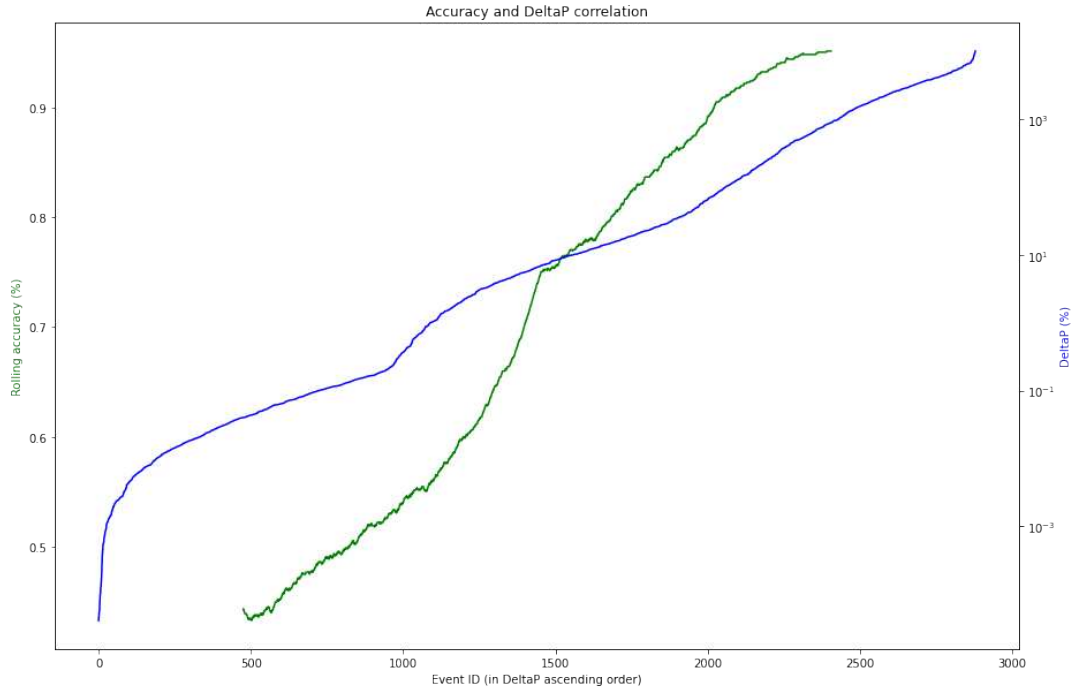
FIGURE 6.12: Rolling accuracy (green) computed over events
sorted for ΔP (blue)

array type	simulations	measurements	measurement (50% cut)
4 ×4	$(71 \pm 1)\%$	$(65.2 \pm 0.6)\%$	$(74 \pm 1)\%$
8 ×8	$(74 \pm 1)\%$	$(68.6 \pm 0.5)\%$	$(75 \pm 1)\%$

TABLE 6.4: Overview of the accuracy of the algorithm after the
selection of event using ΔP

was computed as a rolling value over different subset of events. In figure
6.12 is shown the rolling accuracy (in green) and the ΔP (in blue) for one
couple of crystals as examples.

As we can see, there is a correlation between the accuracy and the quantity
ΔP: the higher the difference in probabilities, the higher the average accuracy.
This led to a selection of half of the events with higher ΔP, that were used to
compute the accuracy reported in the third column of table 6.4. In the case
of this subset of events, the accuracy from measurement is comparable with
results from simulation, reaching values above 70%.

It is worth stressing that the variable ΔP, used as a discriminant for the event
sorting, is computed from values that can be obtained without any prior

knowledge of the crystal of the first interaction. This means that the selection can be operated in the case of a real detector scenario, where the first involved crystal is not known *a priori*.

6.7   Conclusions

The algorithm developed to sort ICS events has been preliminarily studied by means of Geant4 simulations in the previous chapter and with experimental measurements in this one. The results are promising, in particular considering the possibility explained in section 6.6 to operate a section *a posteriori* on the events based on the confidence of the algorithm in each estimation.

The majority of the literature found on the topic of ICS focuses on the recovery of events in the case of specific scanners or detectors with a great variety of sizes, materials, photodetectors and readout solutions. It is therefore difficult to compare the results of each project.

The most general paper found exploring this subject is probably the work of Shao et al., 1996. In this study, the performance of different algorithms is studied with Monte Carlo simulations on pixelated crystals of different materials and sizes. The accuracy reported for LYSO detectors with dimensions comparable to those studied in these two chapters, are in the range of 70% to 80%; however, important factors were neglected such as energy resolution and detector signal-to-noise ratio.

In future studies, the performance of the algorithm on detectors of different sizes and materials could be studied. The impact of the choices made in terms of calibration technique and minimization code could also be further investigated. Moreover the time information, which was discussed regarding these particular detectors in chapter 4, has not been yet included in the algorithm. Finally, the discrimination technique presented in section 6.6 could be further improved and refined.

Multiple studies have suggested the benefit of including ICS events in the reconstruction process in a wide range of system characteristics; some of them with standard pixelated geometries (Park, Rogers, and Clinthorne, 2003, Chinn, Foudray, and Levin, 2006, Chinn and Levin, 2011, Ghazanfari et al., 2011, Clerk-Lamalice et al., 2012, Wagadarikar et al., 2013, "Development of a new position decoder circuit for PET consisting of GAPD arrays to recover intercrystal scattered events", Ota et al., 2016 Hemmati et al., 2017, Yang et al.,

2018, Yoon and Lee, 2018, Kim and Jin, 2018 and Lee, Kang, and Lee, 2018), some with dedicated layered detectors (Rafecas et al., 2003, Hueso González, 2012, Peng et al., 2018, Ilisie et al., 2018, Teimoorisichani and Goertzen, 2019 and Lee et al., 2020) and some with plastic scintillators (Kuramoto et al., 2017). In our specific case, given the possibility shown in chapter 3 to simulate, with auxiliary mechanics, a full ring of detectors, the impact of the algorithm presented on reconstructed images with the detector studied in this thesis could be investigated in the future.

References

Chinn, Garry, Angela MK Foudray, and Craig S Levin (2006). "A method to include single photon events in image reconstruction for a 1 mm resolution PET system built with advanced 3-D positioning detectors". In: *2006 IEEE Nuclear Science Symposium Conference Record*. Vol. 3. IEEE, pp. 1740–1745.

Chinn, Garry and Craig S Levin (2011). "A maximum NEC criterion for Compton collimation to accurately identify true coincidences in PET". In: *IEEE transactions on medical imaging* 30.7, pp. 1341–1352.

Choe, Hyeok-jun et al. "Development of a new position decoder circuit for PET consisting of GAPD arrays to recover inter-crystal scattered events". In: (), pp. 1–3.

Clerk-Lamalice, Julien et al. (2012). "Evaluation of easily implementable inter-crystal scatter recovery schemes in high-resolution PET imaging". In: *2012 IEEE Nuclear Science Symposium and Medical Imaging Conference Record (NSS/MIC)*. IEEE, pp. 2196 –2199.

Comanor, KA, PRG Virador, and WW Moses (1996). "Algorithms to identify detector Compton scatter in PET modules". In: *IEEE transactions on nuclear science* 43.4, pp. 2213–2218.

Ghazanfari, N et al. (2011). "Quantitative assessment of the influence of crystal material and size on the inter crystal scattering and penetration effect in pixilated dual head small animal PET Scanner". In: *5th Kuala Lumpur International Conference on Biomedical Engineering 2011*. Springer, pp. 712–715.

Hemmati, Hamidreza et al. (2017). "Compton scatter tomography in TOF-PET". In: *Physics in Medicine & Biology* 62.19, p. 7641.

Hueso González, Fernando (2012). "Inter-crystal scatter in positron emission tomography: Identification techniques and effects on reconstructed images for AX-PET demonstrator". In:

Ilisie, V et al. (2018). "Building blocks of a multi-layer PET with time sequence photon interaction discrimination and double Compton camera". In: *Nuclear Instruments and Methods in Physics Research Section A: Accelerators, Spectrometers, Detectors and Associated Equipment* 895, pp. 74–83.

Kim, Changlyong and Xiao Jin (2018). "Improved Line-of-Response Allocation for Inter-Crystal Compton Events in PET". In: *2018 IEEE Nuclear Science Symposium and Medical Imaging Conference Proceedings (NSS/MIC)*. IEEE, pp. 1–3.

Kuramoto, M et al. (2017). "Development of TOF-PET using Compton scattering by plastic scintillators". In: *Nuclear Instruments and Methods in Physics Research Section A: Accelerators, Spectrometers, Detectors and Associated Equipment* 845, pp. 668–672.

Lee, Min Sun, Seung Kwan Kang, and Jae Sung Lee (2018). "Novel inter-crystal scattering event identification method for PET detectors". In: *Physics in Medicine & Biology* 63.11, p. 115015.

Lee, Seungeun et al. (2020). "Recovery of inter-detector and inter-crystal scattering in brain PET based on LSO and GAGG crystals". In: *Physics in Medicine & Biology* 65.19, p. 195005.

Ota, R et al. (2016). "Evaluation of a sub-millimeter resolution PET detector with a 1.2 mm pitch TSV-MPPC array one-to-one coupled to LFS scintillator crystals and inter-crystal scatter studies with individual signal readout". In: *IEEE Transactions on Radiation and Plasma Medical Sciences* 1.1, pp. 15–22.

Park, S-J, WL Rogers, and Neal H Clinthorne (2003). "Effect of intercrystal Compton scatter on efficiency and image noise in small animal PET module". In: *2003 IEEE Nuclear Science Symposium. Conference Record (IEEE Cat. No. 03CH37515)*. Vol. 4. IEEE, pp. 2272–2277.

Peng, Peng et al. (2018). "Compton PET: A simulation study for a PET module with novel geometry and machine learning for position decoding". In: *Biomedical Physics & Engineering Express* 5.1, p. 015018.

Rafecas, M et al. (2003). "Inter-crystal scatter in a dual layer, high resolution LSO-APD positron emission tomograph". In: *Physics in Medicine & Biology* 48.7, p. 821.

Shao, Yiping et al. (1996). "A study of inter-crystal scatter in small scintillator arrays designed for high resolution PET imaging". In: *IEEE Transactions on Nuclear Science* 43.3, pp. 1938–1944.

Teimoorisichani, Mohammadreza and Andrew L Goertzen (2019). "A study of inter-crystal scatter in dual-layer offset scintillator arrays for brain-dedicated PET scanners". In: *Physics in Medicine & Biology* 64.11, p. 115007.

Wagadarikar, Ashwin A et al. (2013). "Sensitivity improvement of time-of-flight (ToF) PET detector through recovery of compton scattered annihilation photons". In: *IEEE Transactions on Nuclear Science* 61.1, pp. 121–125.

Yang, J et al. (2018). "Experimental studies of the performance of different methods in the inter-crystal Compton scatter correction on one-to-one coupled PET detectors". In: *2018 IEEE Nuclear Science Symposium and Medical Imaging Conference Proceedings (NSS/MIC)*. IEEE, pp. 1–3.

Yoon, Changyeon and Wonho Lee (2018). "Performance Evaluation of Compton Micro-PET for Detector Modalities: A Monte Carlo Study". In: *Nuclear Technology* 204.3, pp. 386–395.

Chapter 7

Discussion and Perspectives

The first step of the work presented in this thesis was to prepare the experimental setup for the planned studies. This setup consists of a multi-channel DAQ system with parallel time and energy chains. The detectors and electronics used for this project were characterized, the mechanics assembled and the acquisition software developed. The performance of the setup was evaluated and measures were taken in order to be able to monitor and control the system remotely and to easily scale up the data acquisition campaigns. This system opens many possibilities in terms of future studies on multi-channel detectors and image reconstruction.

The first main application of this new setup was to improve the Coincidence Time Resolution of a PET module using Depth Of Interaction information. The DOI is obtained with a technique previously developed at CERN, and the ability to simultaneously measure energy and time allowed to go a step further and to use the DOI knowledge to correct for the time necessary for the optical photons to spread around the photodetector. A high CTR (as low as 157 ps), the single side readout and the simplicity of the light sharing design make this module and this DOI correction technique for CTR very promising for PET scanners with strict requirements.

The other important topic of the study was the Inter-Crystal Scatter events (ICS). In this case, a new algorithm was developed in order to correctly identify the crystal of first interaction. This method was tested and evaluated both on simulation and experimental data. Simulations and measurements agree on the accuracy of the algorithm higher than 70% for at least 50% of the events considered. The events where the algorithm was proven to be more accurate are selected according to a discrimination technique developed on purpose. There are many challenging aspects to investigate in future studies; the most interesting is the possibility to include the time information in the

algorithm, which can be obtained thanks to the experimental setup developed.

The algorithm developed for ICS events could have two major fields of application. On one hand, more immediately, on PET scanners: in this case, the ability to include ICS events in cases where they are discarded could increase the sensitivity (compared to the rejection approach) or could improve the quality of the reconstructed image (compared to the situation when they are included but with a lower accuracy).

Furthermore, without the limitations of use given by the coincidence scenario, the method could be applied to single events allowing to use the same detector described in this thesis as a Compton-camera: this would greatly increase the sensitivity in PET (where single events, much more likely than coincidences, are always discarded) and in SPECT scanners (where collimators strongly limit the sensitivity). Moreover, the fact of not requiring two events in coincidence would open the possibility to use sources different than positron emitters or even to employ multiple gamma sources with different energies simultaneously.